The Dissertation Committee for Irina Vladimirovna Churina Certifies that this is the approved version of the following dissertation:

Experimental Study of Electron Thermal Transport in Dense Aluminum Plasmas

Committee:

Todd Ditmire, Supervisor

Roger Bengtson

Michael Downer

Greg Sitz

Eric Taleff

Experimental Study of Electron Thermal Transport in Dense Aluminum Plasmas

by

Irina Vladimirovna Churina, M.S.

Dissertation

Presented to the Faculty of the Graduate School of

The University of Texas at Austin

in Partial Fulfillment

of the Requirements

for the Degree of

Doctor of Philosophy

The University of Texas at Austin

December, 2008

Dedication

To my family.

Acknowledgements

This work would not have been possible without the help and support of many great people. First of all, I want to thank my lab mates for their willingness to give me a hand in the lab from time to time. I am thankful to former physics graduate students: Will Nichols, Bonggu Shim, Nick Matlis, Greg Hays, Aaron Edens, Will Grigsby, and Gilliss Dyer. Their expertise and advice I always found very helpful.

Let me also express my gratitude to the post-docs with whom I worked through the years, especially Dan Symes for working with me for long hours in the lab, as well as to Aaron Bernstein for his thorough advice and help.

The hard work and help that Byoung-Ick Cho provided in producing the target for my experiments was invaluable. Allen Dalton was also very patient with me as I gave him a seemingly endless stream of HYADES codes to run on Livermore computer. It took a while, but we finally got it right.

To my supervisor, Professor Todd Ditmire, I am grateful for providing me the opportunity to work in his lab and for providing resources and the support necessary for the experiments. His support and guidance in my work were critical to its progress.

To my committee members, thank you for your help and advice with my work and spending the time to review this dissertation.

At last, I want to thank my family for their support over the years. The success of my work would not be possible without my husband, David. His enormous support and motivation helped me to earn this degree.

Experimental Study of Electron Thermal Transport in Dense Aluminum Plasmas

Publication No._____________

Irina Vladimirovna Churina, Ph.D.
The University of Texas at Austin, 2008

Supervisor: Todd Ditmire

A novel approach to study electron thermal transport in dense plasmas was successfully implemented to measure the temperature-dependent conductivity and test the currently available dense plasma model by Lee and More. Intense, femtosecond laser pulses with energy up to 7 mJ per pulse were used to heat free-standing 170-370 nm aluminum foils. We carried-out a new approach to study the plasma transport properties of electron and thermal conduction. In this new approach, rather than probing the front (laser-heated) surface, probing was done on the back surface of a thicker metallic foil heated by a thermal conduction wave generated from a laser-heated front surface. Frequency-domain interferometry with chirped probe pulses allowed us to simultaneously measure the time-dependence of the optical reflectivity and phase-shift in a single shot with subpicosecond resolution. In addition, solid heating was observed to be dominated by the thermal conduction wave prior to the shock-wave breakout at the back surface when laser energy was directly deposited in a thin metallic foil. As a result we were able to estimate the optical conductivity of a dense aluminum plasma in the

range of 0.1 – 1.5 eV. The optical parameters were calculated using the output of a hydrodynamic simulation along with the published models of bound electron contributions to the conductivity and were found to be in reasonable agreement with the measurement. We found that the Lee and More model of a dense plasma's conductivity predicts the real and imaginary part of the measured optical conductivity to within 20%. The simulation results were then used to examine the temperature dependence of the conductivity for 170 and 230 nm aluminum foils heated with the 2-5 mJ pulses. In all cases the same conductivity was obtained, though the arrival of the heat wave and subsequent shock waves varied with the choice of intensity and target thickness. This consistency in the data gave us good confidence in the validity of this technique for deriving conductivity as a function of temperature.

Table of Contents

List of Tables

List of Figures

1 Introduction

The dynamics of dense matter at finite temperature has been an intense area of study for researchers interested in extreme states of matter. This includes research in high-pressure physics[1], applied material studies[2], planetary interiors and brown dwarf stars [3], inertial fusion[4], optimization of yield and duration of x-ray pulses[5-7], the physics of phase transitions[8], and all forms of plasma production in which energy is rapidly deposited into a solid.

Warm dense matter is a specific type of dense matter that is too dense to be described by the classical plasma theory and too hot to be explained by solid-state physics. The temperature-density diagram for aluminum in Figure 1.1 shows the region of interest of the so-called warm dense matter, which is found at near solid density and temperature of $\leq 10eV$. In this region the ion-ion interactions are strongly correlated and the electrons are degenerate. This complexity makes it difficult to determine the equation of state for warm dense matter. Because of the extreme pressures that exist in this phase of matter, it is a challenge in itself for an experimentalist just to create it in a laboratory, let alone to characterize it precisely and accurately.

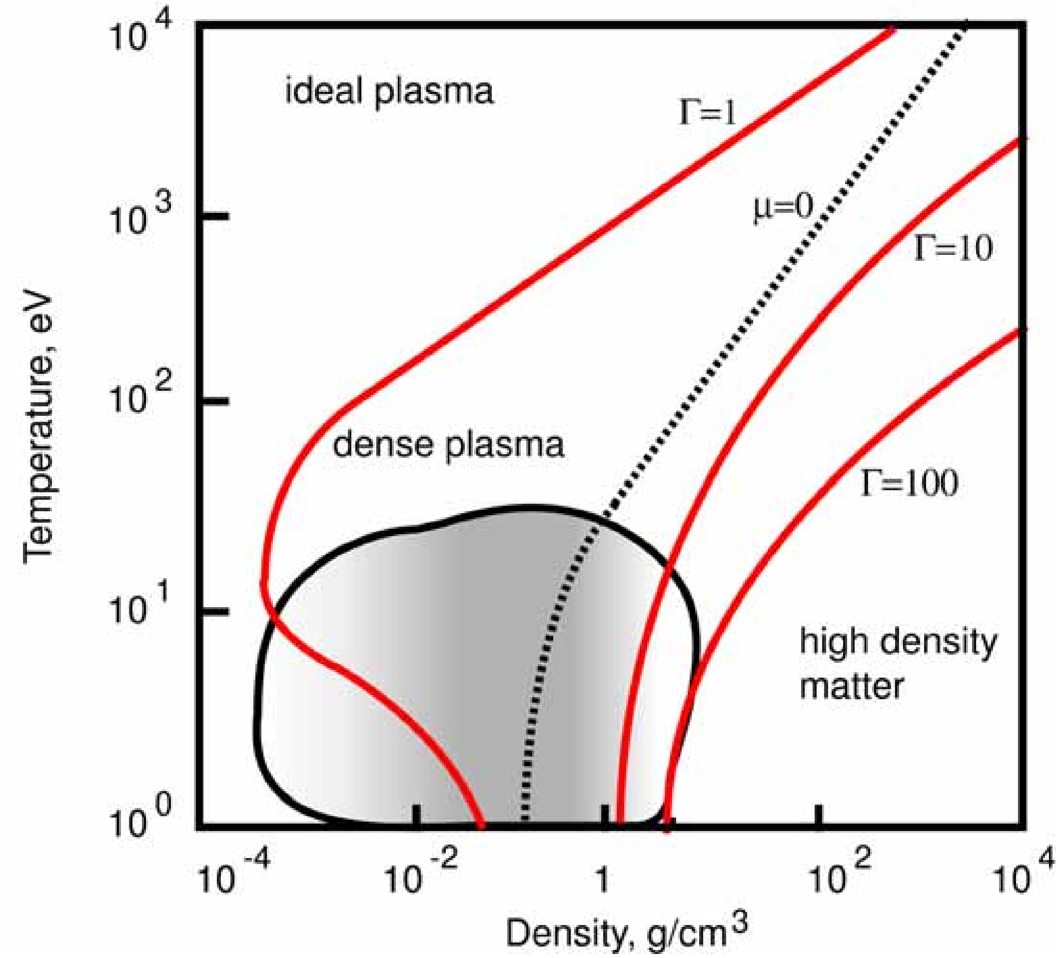

Figure 1.1 The temperature-density space diagram for aluminum. The gray outlined region corresponds to the warm dense matter region, where plasma is strongly coupled (the coupling parameter is $\Gamma > 1$) and strongly degenerate (it is the region to the right of the line where the chemical potential $\mu = 0$).

In the laboratory a dense plasma can be obtained by using various techniques. One way to heat matter to such high temperature and pressure is by driving a shock (traveling discontinuity in pressure, temperature and density)[9, 10] or shock-less compression wave [11] through a sample to be studied. For example, at Sandia National Laboratories, the magnetic pressure produced by the Z accelerator is used to launch metal flyer plates with velocities exceeding 22 km/s. This accelerated flyer plate technique, used in shock experiments, can produce matter at very high pressure (>1 Mb) [9]. Using the Z-pinch approach at Los Alamos National Laboratory, it has been possible to create hot, near solid-density aluminum plasmas, by passing a 200 kA current through aluminum wire imbedded in a glass. The pressure in the heated wire rises dramatically up to 1 Mb and produces a shock in the glass. As the glass compressed, the hot aluminum expanded. Using this technique, the electrical transport properties were measured for hot dense aluminum [10]. Recent development of laser technology has made it possible to create warm, dense matter by using fast, high-energy proton beams. It has been shown that by using proton beams it is possible to heat a solid isochorically up to 20 eV [12, 13].

The other way to obtain dense plasma in the laboratory is to use laser-solid matter interaction methods, where an intense laser pulse deposits energy into material rapidly, before it starts expanding. This experimental approach to create dense plasma was used in my studies. Intense, femtosecond lasers offer a unique way to create and probe dense plasmas. In addition, femtosecond laser probes can be used to examine the fundamental properties of strongly coupled, strongly degenerate plasmas, such as electron thermal and electrical conductivity, particle transport, energy deposition, and the equation of state. It is done with the so-called pump and probe technique, when the first (pump) femtosecond pulse is used for rapid heating of the solid and the second one (probe) acts as a diagnostic of changes that happen on an ultrafast time scale. The probe, then, will typically measure one of the optical properties (reflectivity, phase shift, transmissivity) in order to gain information about fundamental properties of warm dense plasma.

Many experiments were conducted using the pump-probe technique, such as femtosecond laser absorption measurements [14-17], as well as studies of hot expanded states of the front surface of the laser heated target [18, 19]. There have been a number of studies on electron thermal transport and electrical conductivity of such ultrafast created plasmas with much of the information derived through optical reflectivity measurements [20-23]. The authors of those experiments noted the difficulty of extracting the conductivity from reflectivity measurements off the target front surface when plasma density gradients existed [20, 21]. Widmann [22] and Ping [23] have presented successful measurements of conductivity in femtosecond laser-heated metals in which a thin gold foil with thickness of only a few skin depths was nearly uniformly heated by a femtosecond pulse. The optical conductivity was measured in these experiments by simultaneously probing the foil's reflectivity and transmission on a time scale faster than hydrodynamic expansion, with these two quantities yielding the real and imaginary parts of the dielectric function. One drawback to this technique is that there are non-uniformities in the density of the thin (~20 - 30 nm) foils during the transmission measurement because of the expanding front surface of the material.

In this dissertation I have carried-out a new approach to study electron-ion equilibration rates and other electron thermal transport properties, such as electrical and thermal conductivity, in a dense plasma. In this new approach, rather than probing the front (laser-heated) surface, I probed the back surface of a thicker metallic foil heated by a thermal conduction wave from the laser-heated front surface [24]. When the laser energy is deposited directly into the thin (200-500nm) metallic foil, it is possible to observe solid heating that is dominated by the electron thermal conduction in a dense matter before the shock wave breakout at the back surface. That is contrary to the laser shock experiments [25-27], when the solid is heated by the laser driven shock wave.

The goal of this work is to study electron thermal transport properties of dense plasma using this alternative approach, where one can probe the back surface of a thicker metallic foil heated by a thermal conduction wave from the laser-heated front surface.

Such an approach requires measurement of both reflectivity and reflected probe phase shift to derive information on real and imaginary parts of the dielectric function. The frequency domain interferometry (FDI) technique [28] was applied to measure both the reflectivity and reflected probe phase shift. However, to be able to capture the dynamics of the heated foil required continuous measurement of the optical parameters over tens of picoseconds (depending on target thickness and the irradiated laser intensity). By applying chirped pulses to the FDI technique to do the probing of the heated matter it was possible to capture the continuous dynamics of the heated solid in a single shot with sub-picosecond resolution. Having measurements of the temperature-dependent conductivity provides one with the ability to test a currently available dense plasma model as well as to gain information about the dielectric constant of the dense plasma.

In this dissertation, I have performed experimental studies of electron thermal transport in femtosecond-laser heated aluminum. Chapter 2 explains how a dense plasma was created in the laboratory using a table-top, ultra high-intensity laser system. The relevant physics of dense plasmas and current available models are described in Chapter 3. The experimental setup is presented in Chapter 4. The single-shot, interferometric diagnostic used for probing the plasma is described in Chapter 5. Experimental data are presented in Chapter 6 and compared to the simulation results. Chapter 7 summarizes the thesis, provides conclusions and outlines possible future work. Since it is important that a dissertation mark new and original work in a field, it is important to point out the new contributions that this work makes. In that respect, Chapters 4, 5, and 6 detail new and original experimental methods and results that pertain to high energy density science.

2 Making Dense Plasma in the Laboratory

2.1 NEED FOR ULTRASHORT PULSE LASER TECHNOLOGY

To access the dense plasma state of matter we start with the solid density, room temperature target. When an intense, short-pulse laser irradiates the target the heat is deposited at a rate faster then the thermal expansion rate, making it possible to create extreme states of matter at temperature well above the normal melting point and at high density. The high pressure inside the heated region of the target causes the material to expand. Under such a condition, the electronic properties of the target volume can be modified on the ultra-fast time scale. It is necessary to implement an ultra-fast diagnostic to probe the dynamics of this extreme state of matter.

The energy and time requirements for the laser used to generate plasma are met by amplification of a femtosecond laser oscillator. In order to avoid damage of the optical system by amplifying short pulses, the chirp pulse amplification (CPA) technique [29, 30] minimizes the chance of optic damage by amplifying a stretched pulse first and then compressing the amplified pulse into a high-intensity short pulse. The final pulse is expanded to a large beam diameter in order to not damage any of the final optics.

The three stages of the CPA technique are shown in Figure 2.1. In the first stage the short femtosecond pulse is broadened and chirped. The broadening in time of the short pulse is done with a stretcher, which is built out of two diffraction gratings and an imaging telescope between them. The broadened pulse is then safe to be amplified in the optical system. The broadened pulse gains energy going through the second stage, the amplification. To produce the short, high-intensity pulse the amplified broadened pulse is compressed in time in the compressor with the help of diffracting gratings[31]. The result of the final stage is a short, high power pulse.

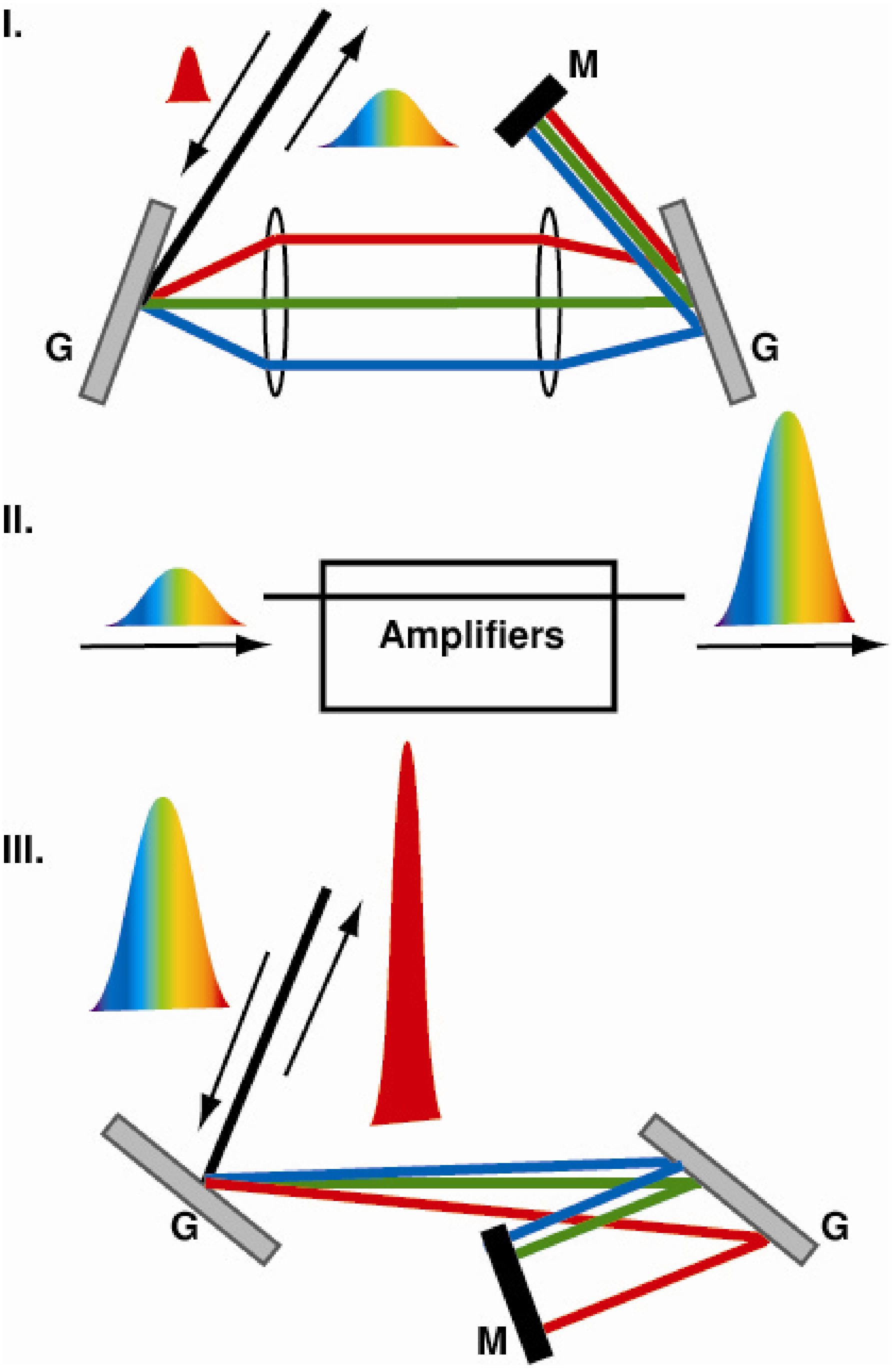

Figure 2.1 Schematics of CPA technique. I. Pulse broadening and chirping II. Pulse amplification. III. Pulse compression. G is a grating, M is a mirror.

2.2 THOR

The Texas High-Intensity Optical Research (THOR) laser is the first high-power laser built by the Ditmire group in the University of Texas at Austin. The experimental work presented in this dissertation was done on that laser. The laser outputs 35 fs pulses with pulse energies up to 700 mJ at a repetition rate of 10 Hz. To generate that type of laser pulse, the chirped pulse amplification (CPA) technique was implemented. The presence of two compressors after amplification made it possible to specify different pulse lengths for each of the pump and probe pulses, each taken to be 35 fs and 28 ps respectively. The laser is been well documented by the previous students in the group as well as the students who actually designed and built this system [32-34]. Below is a description of the laser elements as well as the techniques implemented in the design.

2.2.1 THOR layout

The short pulse, a seed, was generated from a Ti-sapphire oscillator that was amplified following the CPA technique. The layout of the THOR laser is shown in Figure 6.5. The Femtosource Kerr-lens modelocked Ti-sapphire oscillator was pumped by a Spectra Physics Millenia Vs DPSS laser that output 4.5 W at 532 nm. The mode-locked oscillator produced 20 fs, 8 nJ laser pulses centered around 800 nm at a repetition rate of 75 MHz. The 75 MHz signal was passed through a Faraday rotator surrounded by two calcite polarizers to prevent back reflection and feedback. The isolated 75 MHz seed pulse was divided to 10 Hz using a Pockel's cell. The 10 Hz pulse was stretched to 600 ps and passed through a fiber to pick up necessary dispersion for future recompression of the pulse.

The pulse stretcher was designed to have only reflecting optics to eliminate chromatic aberration due to the presence of transmitting optics. Based on the design by Banks *et al.* [35], it has one diffraction grating with a mirrored stripe across the center, one spherical mirror and one flat mirror. The combination of the stripe, the spherical and flat mirrors replaces the telescope that is present in other designs (see Figure 2.1(I))[29].

Following stretching, the pulse was sent to the second stage of the CPA system, the amplification. THOR consists of three amplifiers. The first one is the regenerative amplifier. The Ti-sapphire crystal was pumped by 45 mJ, 532nm pulses that were split from the Quantel Big Sky laser 10 Hz output. After making 24 round trips in the amplifier cavity the amplified pulse was switched out by a Medox Pockel's cell. To minimize any leakage from the regenerative amplifier the ejected pulse was passed through two polarizers with a half waveplate between them, and another Pockel's cell. The final gain in the first amplifier is of the order of $\sim 10^6$, producing a ~1-2 mJ pulse.

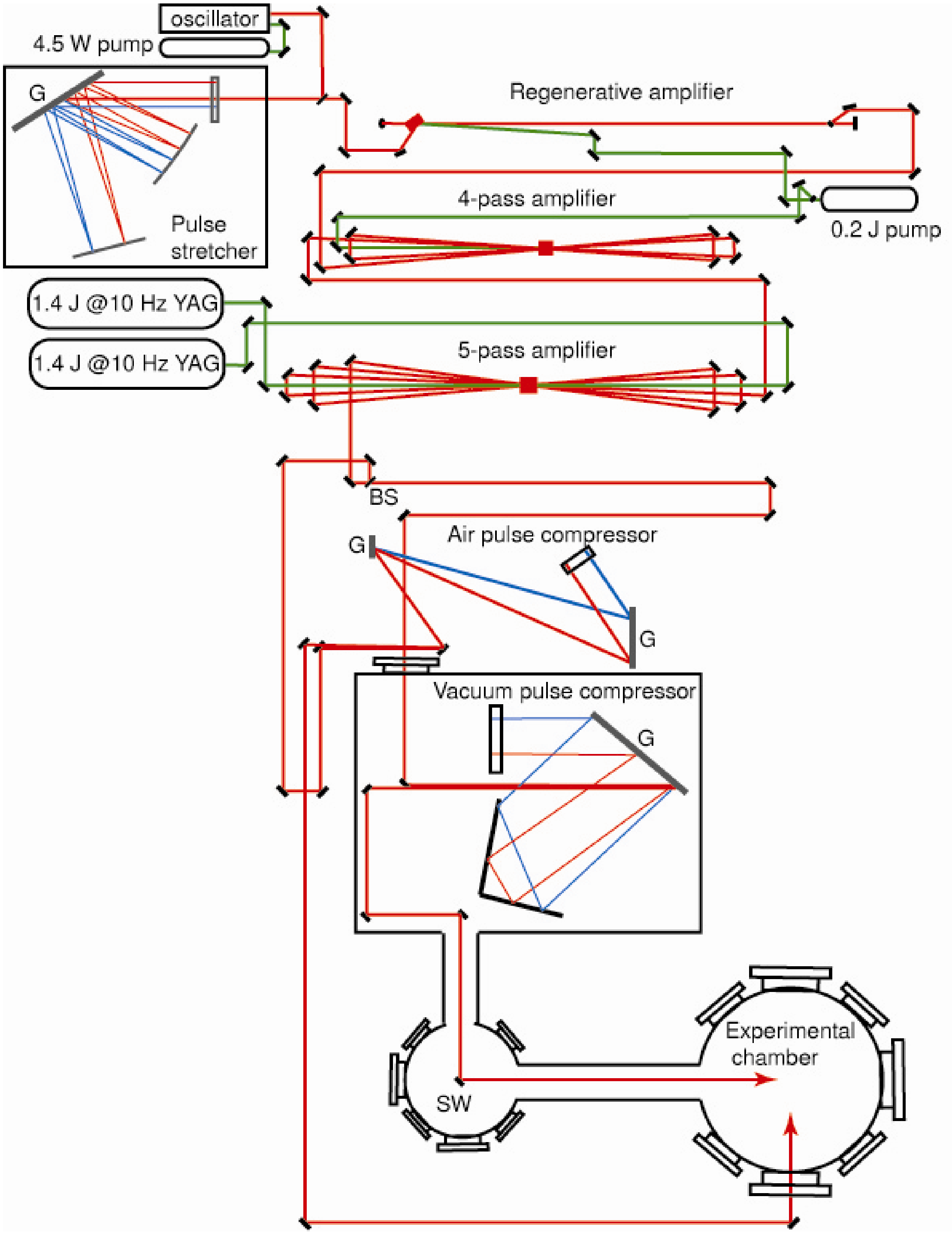

Figure 2.2 The layout of the THOR laser including the output beam transport to the experimental chamber. G is a grating, BS is a beamsplitter, SW is a switchyard .

The second amplifier is a 4-pass amplifier. The seed pulse was passed 4 times though the Ti-sapphire crystal pumped by 110mJ, 532 nm Big Sky pulses. The pulse was amplified to ~20 mJ and expanded in the spatial filter to 10 mm diameter pulse.

The final amplifier is a 5-pass amplifier. Like the 4-pass amplifier, the seed pulse traces a "bow-tie" shape. The 5-pass amplifier's Ti-sapphire crystal was pumped on each side with two Spectra Physics PRO 350 YAG lasers. Each laser delivers 1.4 J, 532 pulses at 10 Hz. After passing trough the crystal 5 times, the seed pulse was amplified to ~1J.

Before sending the amplified pulse to the final CPA stage, the pulse was spatially filtered and expanded to a 50 mm diameter beam. The expanded beam had a low enough fluence to avoid any grating damage in the vacuum compressor.

The THOR laser has two compressors: one in vacuum, and one in air. The presence of two compressors gives more flexibility in designing multiple beam experiments.

The air compressor is designed to compress up to 80mJ pulses. The beam splitter picks off 8% of the amplified pulse after the 5-pass amplifier. The reflected beam was spatially filtered and expanded to 20 mm in diameter. The air compressor has two parallel gratings and a vertical roof top mirror. By changing the distance between the gratings, the 550 ps pulse can be compressed up to 60 fs. The output of the air compressor directs the beam toward the experimental chamber in air and enters the chamber through a window.

The vacuum compressor is a single grating compressor. In order to be able to use only one grating, a horizontal retro-reflector was installed to fold the compressor in half and use the same grating twice. A vertical roof-top mirror is used to double-pass the beam and offset the input from output beams. The pulse was compressed to ~35 fs and directed to the switchyard, where it was redirected to the experimental chamber in vacuum.

2.2.2 Diagnostics: Third order autocorrelation

It is important to characterize the laser pulse before carrying out the experiment. It was crucial for the solid target experiments not only to know the pulse duration and pulse peack intensity, but also to define the position and amplitude of any pre-pulses and post-pulses. While the second order autocorrelation was used to measure the pulse duration, it did not allow us to distinguish between the pre- and post-pulses because of the output signal being symmetric around the zero time. Using a third-order autocorrelation solved this problem.

In the third-order autocorrelator, the 1ω pulse was sent to a doubling crystal and then separated from the 2ω pulse with a dichroic beamsplitter (Figure 2.3). After adjusting the delay between 1ω and 2ω pulses, the pulses were recombined in a second nonlinear crystal producing 3ω pulse, which was the correlation between 1ω and 2ω pulses. By changing the delay between 1ω and 2ω pulses, the 2ω pulse was swept through the fundamental 1ω pulse allowing us to distinguish between the pre- and post-pulses.

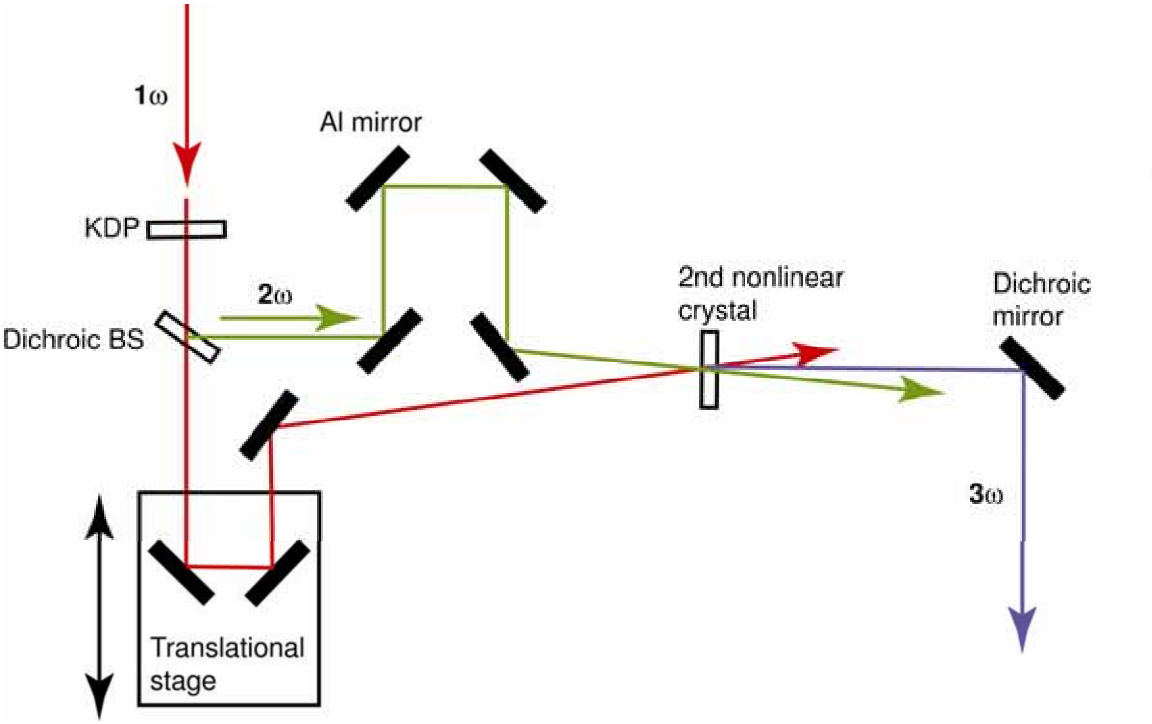

Figure 2.3 Schematics of the third-order autocorrelator. BS is a beamsplitter.

The third-order autocorrelation scan taken in the target room in February 2006 is shown in Figure 2.4. The input energy to the autocorrelator was kept below 7 mJ in order to avoid any parasitic signal generation on the aluminum mirrors used in the autocorrelator. By placing the set up in the target room, we were able to isolate the PMT detector from the noise generated in the laser room. It was also important to isolate the signal of the 3ω pulse from the 1ω and 2ω pulses. Two dichroic mirrors were used after the second nonlinear crystal, as well as several interference filters before the PMT detector. To measure wide dynamic range between the main pulse, pre-/post-pulses, and ASE glass slides were used as the attenuators for 3ω pulse.

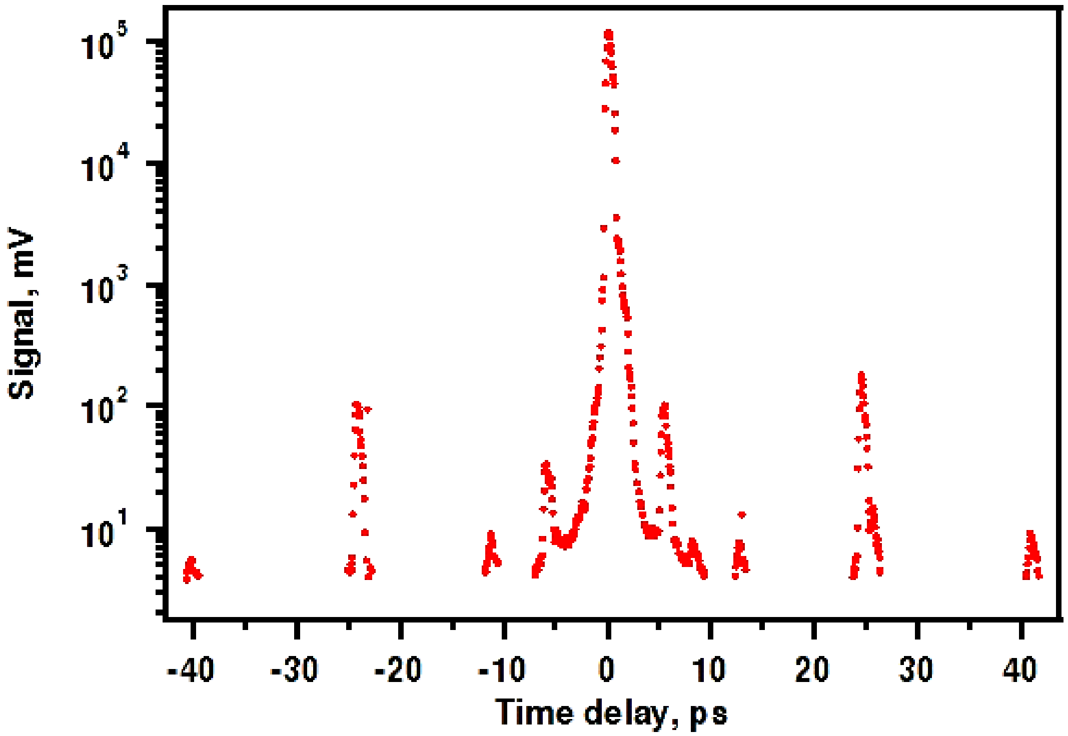

Figure 2.4 Third-order autocorrelation of 800 nm THOR output and frequency doubled signal as a function of the time delay between them.

As seen from the graph (Figure 2.4) the dynamic range of the measurement was of the order of 10^6. Within this dynamic, range pre/post pulses at -40, -24, -11, -5.5, 8, 13, 24.5, and 21 ps were observed. The pre-pulse at 24 ps with the pulse-to-pre-pulse contrast ration of 10^3 indicated that with the irradiated intensity of 800 nm a pulse bigger than 10^{13} W/cm^2 was interacting with the solid target, which was enough to modify considerably the target before the main pulse arrival. It is important to take this into consideration for the solid target experiments. It was also observed that the main pulse was asymmetric. By zooming in (Figure 2.5) around the main pulse we concluded that the presence of the post-pulse within a few ps after the main pulse was the reason for the modification of the main pulse. The presence of this post pulse was confirmed with a spectrometer measurement of the pulse after the five pass. The measured pulse envelope contained slight modulations. Using an analysis based on the Fourier transform relation between time and frequency, the presence of a 550 fs post pulse was verified. This post-pulse was also observed with the second order autocorrelation, and it was attributed to the five pass's crystal orientation. Since the Ti-sapphire crystal has different indexes of refraction along different axes, it takes different amounts of time for the seed pulse to pass thru the different axes, resulting in the post-pulse. To improve the pulse envelope, the five pass's crystal was mounted on a galvanometer stage and rotated to minimize the modulations.

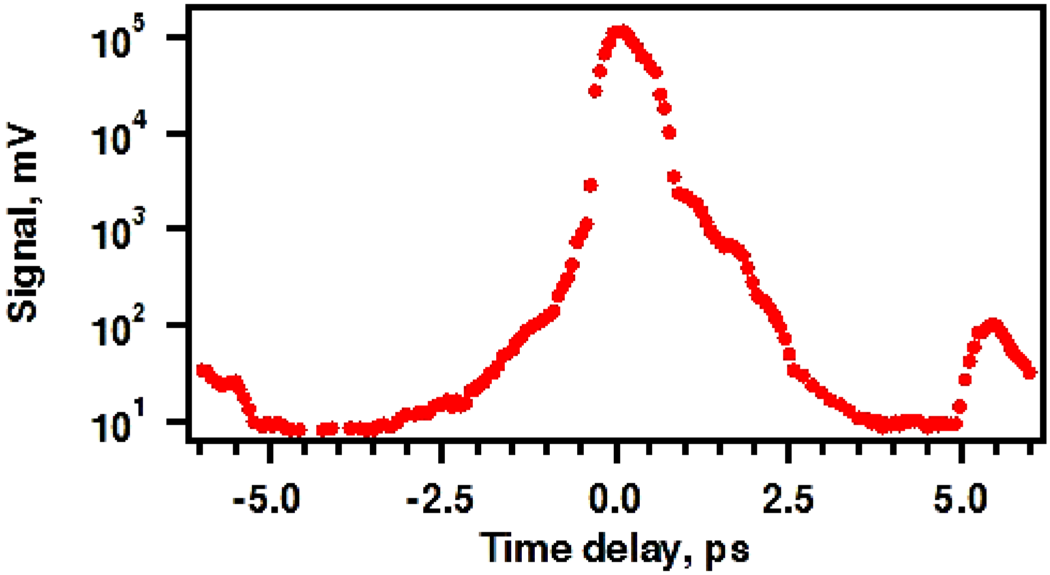

Figure 2.5 Third-order autocorrelation trace shows the main pulse asymmetry

3 Theory of Dense Plasma Dynamics

3.1 SHORT PULSE ABSORPTION MECHANISM

When a short-pulse laser irradiates a target, heat is deposited at a rate faster than the thermal expansion rate. It makes it possible to heat solid-state matter isochorically (at constant volume, density) to temperatures above 10 eV at electron densities close to 10^{24} cm^{-3} [14, 15, 36]. Those high electron densities are equivalent to that of solid-state matter.

When short laser pulses irradiate a solid, most of the energy is absorbed by electrons, causing a higher electron temperature compared to the ion temperature. To reach thermodynamic equilibrium requires a longer time scale than the duration of the laser pulse due to the slow electron-ion relaxation. For moderate intensities of the order of 10^{14} W/cm^2, the electron-ion relaxation time is of the order of several picoseconds.

The interaction of the ultrashort laser pulse with matter is illustrated in Figure 3.1. When a short laser pulse at wavelength λ irradiates a metal target with index of refraction n, the thin front layer is heated to a thickness given by the skin depth $d_{skin} = \frac{\lambda}{4\pi \operatorname{Im}(\hat{n})}$.

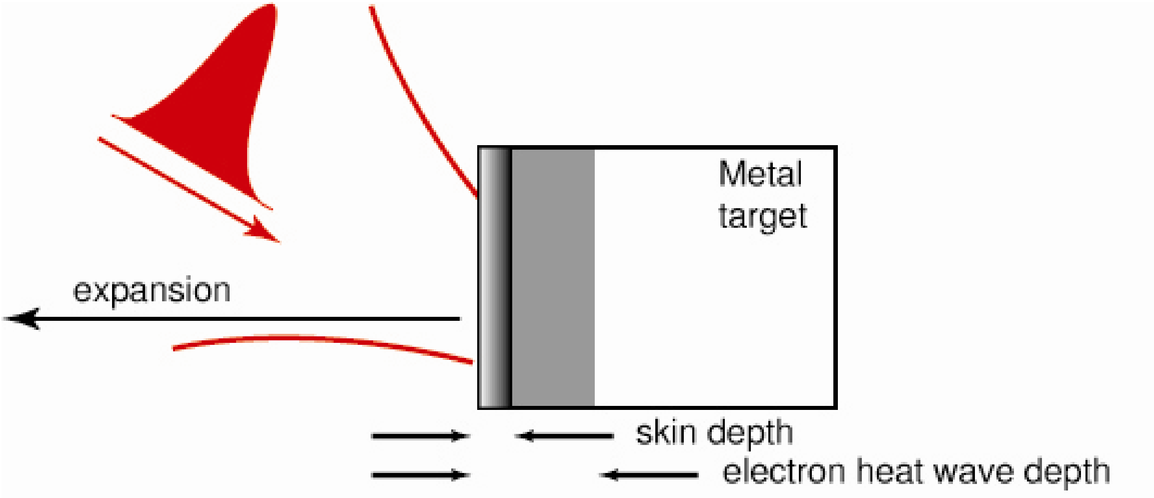

Figure 3.1 Diagram of the high intensity femtosecond pulse interaction with solid metal target.

For cold aluminum, d_{skin} is 7 nm at 800 nm wavelength. The typical expansion time for aluminum heated to 10 eV by a laser intensity exceeding 10^{14} W/cm^2 is d_{skin}/c_s, where the ion-sound velocity c_s in plasma with Z electrons per ion, T_e and T_i electron and ion temperatures, and ion mass m_i is given by [37]

$$c_s = \sqrt{(ZT_e + 3T_i)k/m_i} \; . \tag{3.1}$$

For the chosen laser intensity the expansion time is ~150 fs. While the thermal expansion rate is slower than the 40 fs FWHM laser pulse achievable with our laser system, to be able to characterize the created state of the solid density plasma requires that the diagnostic should be done on a sub-picosecond time scale as well.

Once the laser is absorbed by the target, the electron thermal conductivity, κ, defines the spatial profile of T_e and can be characterized by the depth of the heat wave propagation, x_{hw} [38, 39]:

$$x_{hw} = \sqrt{\chi t}, \tag{3.2}$$

$$\chi = \frac{\kappa}{\rho c_p} \propto \lambda_e \upsilon_e \tag{3.3}$$

where the heat diffusivity, χ, can be defined by electron mean free path, λ_e, and electron thermal velocity, υ_e. The specific heat of electrons, c_p, is defined at constant pressure, and ρ is a mass density.

Figure 3.2 shows the depth of the heat wave in heated aluminum as a function of the pulse length for laser intensity of the order of 10^{14} W/cm^2. As seen from the graph for laser pulses longer than ~10 fs, the initial depth of the heat wave propagation exceeds the skin depth.

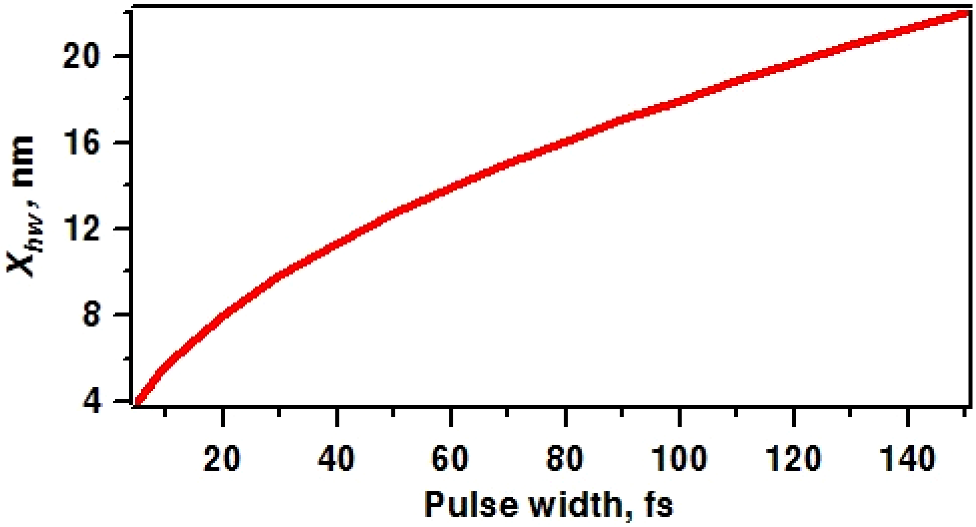

Figure 3.2 The initial depth of the heat wave propagation in a heated aluminum as the function of pulse width for laser intensities of the order of 10^{14} W/cm^2.

3.2 ENERGY TRANSPORT

When energy emitted by the material travels a small (smaller than the region of interest) distance before being reabsorbed by the material, the heat transport can be described as diffusive [39]. Diffusive theory gives the heat flow as:

$$Q = -\kappa(T)\nabla T \tag{3.4}$$

with the thermal conductivity $\kappa(T)$ as a function of temperature T.

The energy flow in a high-temperature plasma can take place by either collisional-electron or radiative transport [39, 40]. The energy transport in plasma is governed by Coulomb collisions of electrons for plasma temperatures smaller than 100eV[40]. The diffusive theory for the conduction of heat by electrons is given by substituting the thermal conductivity of an ideal gas into Equation (3.4):

$$Q = -\frac{1}{3}\lambda_e \upsilon_e n_e k_B \nabla T_e = -\kappa \nabla T_e \,. \tag{3.5}$$

The average, mean free path, λ_e, for deflection of electrons with multiple coulomb collisions with ions can be expressed as:

$$\begin{aligned} \lambda_e = \upsilon_e \tau_{ie} &= \sqrt{\frac{k_B T_e}{m_e}}\frac{1}{4}\frac{m_e^{1/2}(k_B T_e)^{3/2}}{n_i Z^2 e^4 \ln\Lambda} = \frac{1}{4}\frac{(k_B T_e)^2}{n_e Z e^4 \ln\Lambda} \\ &= 4.5\times 10^{13}\frac{T_e^2[eV]}{n_e[cm^{-3}]Z\ln\Lambda} cm \end{aligned} , \tag{3.6}$$

where electron-ion collision time, τ_{ie}, was found by calculating the cross-section of the impact, and defining the electron thermal velocity as $\upsilon_e = \sqrt{k_B T_e / m_e}$ [37, 39]. The Coulomb logarithm, $\ln\Lambda$, is defined by the ratio of maximum, q_{max}, and minimum, q_{min}, momentum transfer of on an electron scattered off an ion of charge Z:

$$\ln\Lambda = q_{\max} / q_{\min} \tag{3.7}$$

The thermal conductivity can be expressed as

$$\kappa = \frac{4k_B (k_B T_e)^{5/2}}{Z e^4 m_e^{1/2} \ln\Lambda} \tag{3.8}$$

where κ is independent of density and proportional to $T_e^{5/2}$. Taking into account electron-electron collisions for small to moderate values of Z, one obtains the Spitzer-Harm result approximation by multiplying Eq.(3.8) by $g(Z) \simeq (1+3.3/Z)^{-1}$ [37].

At high temperature the radiative transport starts to dominate over the collision-electron transport, when the energy contained in the plasma is emitted as radiation in ultraviolet and X-ray regions. The radiative thermal conductivity becomes [39]

$$\kappa_{rad} = \frac{16}{3} k_{SB} T_e^3 \lambda_{Rosseland} , \tag{3.9}$$

where $\lambda_{Rosseland}$ is a radiative mean free path and k_{SB} is the Stefan-Boltzmann constant.

$$\lambda_{Rosseland} = 9 \times 10^6 \frac{T_e^2}{Z^2 n_i} \exp(I / k_B T_e)[cm] \tag{3.10}$$

Based on Eq.(3.10) the κ_{rad} depends on density and is proportional to T_e^5, making the radiative diffusion highly non-linear.

The study in this work is focused on moderate temperature plasma (<100eV), where the collision-electron transport is dominant. However, hot plasma studies are of great interest to the community because of the ability of hot plasma to emit X-rays. The possibility of enhancing the X-ray yield and temperature from modified surfaces with the wavelength scale futures irradiated with intense laser pulses is being explored in our group. See Appendix A.

3.3 DEGENERATE, STRONG COUPLED PLASMA

Partial ionization causes strong, nonideal effects because the bound electrons have large binding energies and very large radiative cross section.

In an ideal plasma electrical interactions are weak. The binding energy of the screening cloud around one charge is less than the thermal energy of the plasma:

$$\frac{Q^2 e^2}{r_{Debye}} < kT .$$

The Debye radius, r_{Debye}, characterizes the dimension of the cloud, Q is ion charge, and e is electron charge. In this case many particles participate in the screening. The situation changes for low temperature and/or high-density plasma when the screening energy rises and exceeds kT. The resulting plasma is a strongly coupled plasma with the electrical interaction exceeding kinetic energy. The ion coupling parameter, Γ, becomes bigger than 1:

$$\Gamma = \frac{Q^2 e^2}{r_0 kT} \geq 1$$

where r_0, the ion sphere's radius, is equal to $(4\pi / 3n_{ion})^{1/3}$. The strongly coupled plasma can not be treated with the Debye screening [41] approach due to the strong ion-ion correlations. Figure 3.3 shows the changes in the ionic potential during the transition from ideal to dense plasma states. As the distance between the ions changes, the ion-ion correlations become important and should be taking into account.

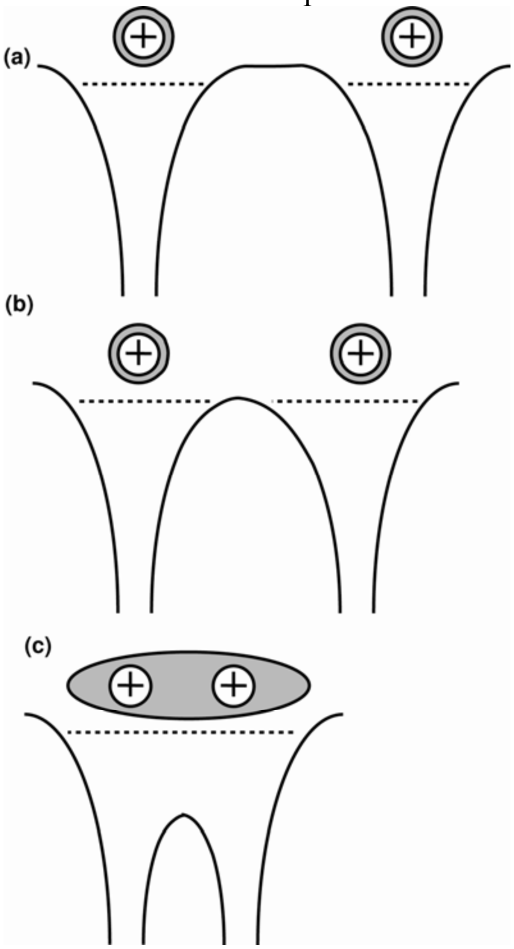

Figure 3.3 Models of ionic potential for (a) ideal plasma, (b) dense plasma, (c) high density plasma.

Another high-density non ideal effect is degeneracy of free electrons, which occurs at temperature below the Fermi temperature, T_F:

$$kT \le kT_F = \frac{\hbar}{2m}(3\pi^2 n_e)^{2/3}.$$

When the free electrons are degenerate the equilibrium Fermi-Dirac distribution

$$f(\varepsilon) = \frac{1}{1+\exp(\varepsilon-\mu)/kT} \tag{3.11}$$

takes into account quantum effects and replaces the usual classical Maxwellian distribution ($f(\varepsilon) \propto \exp(-\varepsilon/kT)$) [39, 42]. The chemical potential, μ, depends upon temperature and density of the electrons.

3.4 ELECTRICAL AND THERMAL CONDUCTIVITY

The optical properties of the material describe its electronic response to electromagnetic radiation. However, the electrical conductivity is needed to understand the transport properties of a plasma. For example, electrical conductivity is one of the fundamental parameters of laser-matter simulations. Furthermore, using the Weidemann-Franz relation[43], $\kappa/\sigma \sim T$, the electron thermal conductivity, κ, can be obtained from the known dc electrical conductivity, σ. For laser matter interactions, it is important to determine conductivity values for a large range of plasma parameters, such as temperature and density, because matter will be rapidly driven from cold to very hot temperatures under laser excitation.

3.4.3 Ideal plasma conductivity.

The electric current flow is a response of the plasma to the applied electric field E. As the electrons accelerate, the friction force F appears due to collisions with heavier ions and eventually compensates the electric force

$$eE + F = 0 \tag{3.12}$$

The friction force can be defined by the mean electron velocity *u* resulting from the balance between *E* and *F* and can be expressed as

$$F = mu\nu_{ei} \tag{3.13}$$

Where $\nu_{ei} = n_i \vartheta_{coulomb} \upsilon_{therm}$ is electron ion collision frequency, which is defined by the Coulomb cross section, $\theta_{Coulomb}$, ion density, n_i and electron thermal velocity, υ_{therm}.

The mean electron velocity can be expressed as:

$$u = \frac{eE}{m\nu_{ei}} \tag{3.14}$$

Using the Ohm's law the current density can be written as:

$$j = n_e eu = n_e e\frac{eE}{m\nu_{ei}} = \sigma E \tag{3.15}$$

From the Ohm's law the electrical conductivity is:

$$\sigma = \frac{n_e e^2}{m\nu_{ei}} \tag{3.16}$$

The electron-ion collision frequency is:

$$\nu_{ei} = n_i \frac{4\pi Z^2 e^4 \ln\Lambda}{m^2 \upsilon^4} \upsilon = \frac{4\pi n_i Z^2 e^4 \ln\Lambda}{m^{1/2}(k_B T)^{3/2}} \tag{3.17}$$

The electrical conductivity of fully ionized plasma has the following expression:

$$\sigma = \frac{n_e (k_B T_e)^{3/2}}{4\pi m^{1/2} n_i Z^2 e^2 \ln\Lambda} = \frac{(k_B T_e)^{3/2}}{4\pi m^{1/2} Z e^2 \ln\Lambda} \tag{3.18}$$

For an ideal plasma, conduction rises with the temperature because of a decrease in the electron-ion Coulomb cross section with increasing kinetic energy of electrons, $\vartheta_{coulomb} \approx 1/\upsilon^4 \approx 1/T^2$.

The thermal conductivity of fully ionized plasma was defined in Equation (3.8), and is proportional to $T_e^{5/2}$. The electrical conductivity of fully ionized plasma is proportional to $T_e^{3/2}$. The Spitzer results are identical to Equation (3.8) and Equation(3.18), except for the numerical cofactor.

$$\begin{aligned}\kappa_{Spitzer} &= 8\left(\frac{2}{\pi}\right)^{3/2}\frac{k_B(k_BT_e)^{5/2}}{Ze^4m_e^{1/2}\ln\Lambda}\\ \sigma_{Spitzer} &= 2\left(\frac{2}{\pi}\right)^{3/2}\frac{(k_BT_e)^{3/2}}{Ze^2m_e^{1/2}\ln\Lambda}\end{aligned}. \tag{3.19}$$

Eq.(3.19) was obtained for the ideal plasma having a Maxwellian distribution of free electrons [44]. These formulas are valid for fully ionized, non-degenerate plasmas, i.e for low density and high temperature states. For non ideal plasmas, the electron degeneracy at high mass density will reduce the number of conduction electrons to the electrons within a narrow range near the Fermi energy. In a degenerate plasma, the smaller number of states that participate in conduction has the effect of reducing the temperature dependence of conduction coefficients. Therefore when the Spitzer conductivity is used to calculate the plasma conductivity for a plasma at solid density and low temperature (<10 eV), it gives a result that is shown to be incorrect by a large factor. To overcome this inconsistency, semiclassical [42] and quantum mechanical [45, 46] conductivity models were developed. The (semiclassical) model developed by Lee and More [42] is widely used and obtain reasonably good agreement with existing theory and experiment [10, 19, 21, 47, 48].

3.4.4 Lee and More conductivity model for dense plasma

The Lee and More [42] conductivity model gives a consistent and complete set of transport coefficients, including electrical and thermal conductivities. The transport coefficients are obtained from the solution of the Boltzmann equation in the relaxation time approximation. The collision operator includes contributions from the scattering of electrons by ions and neutrals. The electron degeneracy effects are taken into account by using a Fermi-Dirac distribution for the electrons (Eq.(3.11)).

The electrical and thermal conductivities are given by:

$$\sigma = A\frac{n_e e^2 \tau}{m}$$
$$K = B\frac{n_e k^2 T \tau}{m} \tag{3.20}$$

Where τ is average collision time, and A and B are numerical factors expressed in terms of Fermi-Dirac integrals, F_n:

$$A = \frac{4}{3}\frac{F_2(\mu/kT)}{(1+e^{-\mu/kT})[F_{1/2}(-\mu/kT)]^2}$$
$$B = \frac{20}{9}\frac{F_4(-\mu/kT)}{(1+e^{-\mu/kT})[F_{1/2}(-\mu/kT)]^2}\left(1-\frac{16}{15}\frac{F_3^2}{F_2F_4}\right)$$
$$F_n(x) = \int_0^\infty \frac{y^n dy}{1+\exp(x+y)}$$

The average electron relaxation time is

$$\tau = \frac{3}{2\sqrt{2}\pi}\frac{m^{1/2}(kT)^{3/2}}{Z^2 n_i e^4 \ln\Lambda}[1+\exp(-\mu/kT)]F_{1/2} \tag{3.21}$$

Figure 3.8 shows a theoretical conductivity for aluminum at constant density (2.7 g/cm^3). At low temperature (<1eV) a curve of the form $\sigma = a/T$ can be fit to the Lee and More conductivity curve. In this region conductivity shows the Ohmic-like temperature dependent conductivity of metal and can be approximated by the usual condensed-matter theory. At higher temperature (>100eV) a curve of the form $\sigma = bT^{3/2}$ can be fit to the theoretical conductivity. This indicates that the ideal plasma approximation is valid. Between these low and high temperature regimes, the conductivity is almost constant that corresponds to the region of non-ideal plasma, where the degeneracy of electron states and ion-ion correlations are important. The minimum reached in conductivity temperature dependence is viewed as a transition from solid-mater to ideal plasma. To be able to describe this state of matter, knowledge of the conductivity is crucial.

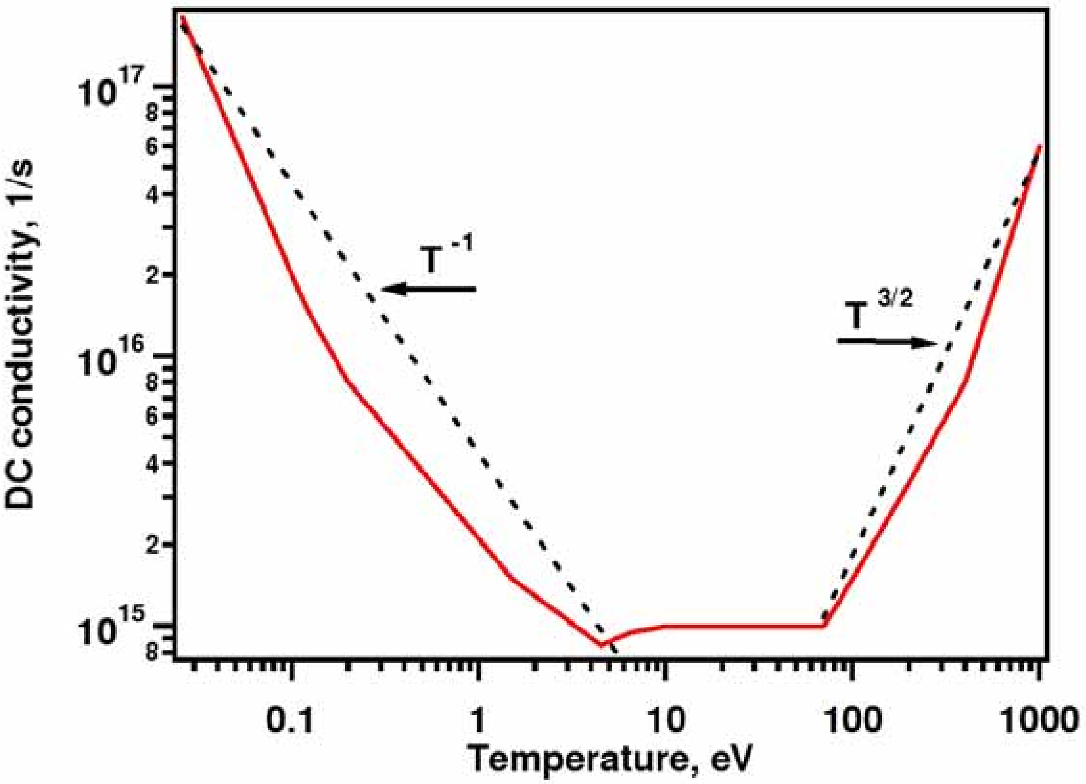

Figure 3.4 Lee and More electrical conductivity for solid density aluminum (line). The dash line is a fit.

3.5 OBTAINING OPTICAL CONDUCTIVITY

Experimental efforts to characterize laser heated matter usually have employed optical probing, whereby the optical constants (reflectivity, phase shift, transmissivity) of plasma are measured [14-17, 19, 20, 22, 23, 25, 36, 48-50]. The goal of this experiment is to use the optical parameters to determine conductivity (or vice-versa) and compare to the theory. Specifically, the hydrodynamic simulations using the Lee-More conductivity model and equation of state were used to predict the experimental observables.

Optical properties of the material are described by its complex dielectric function $\varepsilon_\omega = 1 + i4\pi\sigma_\omega / \omega$. From this formula the total optical conductivity is

$$\sigma_\omega = \frac{\omega}{i4\pi}(\varepsilon_\omega - 1)\,. \qquad (3.22)$$

Direct check of conductivity models can be done using the measured values of $\sigma_\omega(\Delta \mathrm{E}, \rho)$ for defined plasma state.

Assuming the free electron gas behavior, additional properties of warm dense plasma can be found. To define the dielectric constant as a function of frequency, we will consider the free electron contribution to (3.22). The momentum, p, of a free electron is related to the wavevector, k, by $p = m\upsilon = \hbar k$, based on the quantum theory description of electron (Fermi) gas [51]. The equation of motion for the displacement δk of a Fermi sphere of a particle in the presence of applied electric field E is:

$$\hbar\left(\frac{d}{dt} + \frac{1}{\tau}\right)\delta k = -eE = F\,, \qquad (3.23)$$

Where the first term on a left describes the free particle acceleration and the second one represents the effect of the collisions (friction) with the characteristic relaxation time τ. In terms of the gas velocity, the equation of motion is given as:

$$m\left(\frac{d}{dt} + \frac{1}{\tau}\right)\upsilon = F \qquad (3.24)$$

The force F acting on electron is an alternating electric field:

$$F(t) = -eE\exp(-i\omega t) \qquad (3.25)$$

Based on this, the solution to (3.24) is of the form:

$$\upsilon(t) = \upsilon\exp(-i\omega t) \qquad (3.26)$$

Applying this solution to the equation of motion we get:

$$\begin{gathered} m\left(-i\omega + \frac{1}{\tau}\right)\upsilon = -eE, or \\ \upsilon = -\frac{e\tau/m}{1 - i\omega\tau}E \end{gathered} \qquad (3.27)$$

Using the Ohm's law the current density can be written as:

$$j = ne\upsilon = \frac{ne^2\tau/m}{1 - i\omega\tau}E = \sigma(\omega)E\,, \qquad (3.28)$$

where n_e is an electron density.

From Eq.(3.28), the frequency dependent optical conductivity in the optical range and in the absence of the interband transition can be described by the Drude model:

$$\sigma_{free}(\omega) = \frac{\sigma_{DC}}{1 - i\omega\tau}, \qquad \sigma_{DC} = ne^2\tau / m \tag{3.29}$$

where σ_{DC} is the (dc) electrical conductivity.

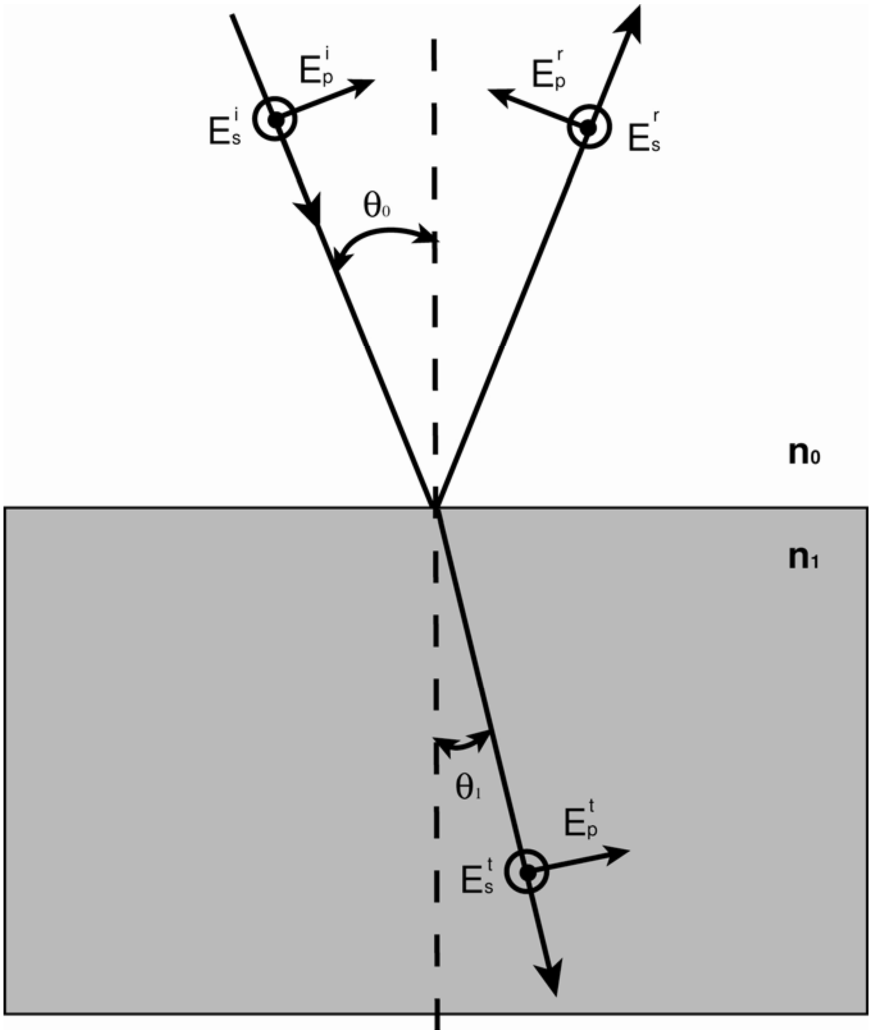

Figure 3.5 The plane wave reflection and refraction at the boundary between two media.

To determine the metal optical response the Fresnel equation can be used in the case of a very steep density gradient. In that case, the electron density gradient scale length, $n_e/(dn_e/dx)$, is very much shorter than the wavelength of the incident probe, λ. Figure 3.5 shows a plane wave incident on a medium with the index of refraction n_1. The electric field of the incident plane wave, traveling in the z direction, can be expressed as:

$$E^i = E_0 \exp(i\omega(\frac{\tilde{n}_0 z}{c} - t)) \tag{3.30}$$

The complex index of refraction is defined by the dielectric constant and can be written as:

$$\tilde{\varepsilon} = \tilde{n}^2 = (n + ik)^2, \tag{3.31}$$

where n is a index of refraction and k is a index of absorption.

The Fresnel amplitude reflection coefficients for s- and p-polarized light, obtained by setting up and solving the boundary-value problem, is:

$$\begin{aligned} \tilde{r}_s &= \frac{E_s^r}{E_s^i} = \frac{\tilde{n}_0 \cos(\theta_0) - \tilde{n}_1 \cos(\theta_1)}{\tilde{n}_0 \cos(\theta_0) + \tilde{n}_1 \cos(\theta_1)} \\ \tilde{r}_p &= \frac{E_p^r}{E_p^i} = \frac{\tilde{n}_1 \cos(\theta_0) - \tilde{n}_0 \cos(\theta_1)}{\tilde{n}_1 \cos(\theta_0) + \tilde{n}_0 \cos(\theta_1)} \end{aligned} \tag{3.32}$$

The amplitude transmission coefficient are:

$$\begin{aligned} \tilde{t}_s &= \frac{E_s^t}{E_s^i} = \frac{2\tilde{n}_0 \cos(\theta_0)}{\tilde{n}_0 \cos(\theta_0) + \tilde{n}_1 \cos(\theta_1)} \\ \tilde{t}_p &= \frac{E_p^t}{E_p^i} = \frac{2\tilde{n}_0 \cos(\theta_0)}{\tilde{n}_1 \cos(\theta_0) + \tilde{n}_0 \cos(\theta_1)} \end{aligned} \tag{3.33}$$

The resulting amplitude reflection coefficients can be written as:

$$\begin{aligned} \tilde{r}_s &= |\tilde{r}_s| \exp(i\varphi_s) \\ \tilde{r}_p &= |\tilde{r}_p| \exp(i\varphi_p) \end{aligned} \tag{3.34}$$

Where $|\tilde{r}_s|$ and $|\tilde{r}_p|$ are the amplitudes of the reflectance and φ_s and φ_p are the phase changes on reflection. The intensity reflection coefficients are

$$R_{s,p} = \tilde{r}_{s,p} \tilde{r}_{s,p}^* \tag{3.35}$$

At normal incidence the reflectivity of the reflected probe is:

$$R_s = R_p = \frac{(n_0 - n_1)^2 + k_1^2}{(n_0 + n_1)^2 + k_1^2} \tag{3.36}$$

The phase changes at normal incidence are:

$$\tan\varphi_s = -\tan\varphi_p = \frac{2n_0k_1}{k_1^2 + n_1^2 - n_0^2} \tag{3.37}$$

To determine the inhomogeneous metal film optical response, Maxwell's equation are solved by the matrix method [52]. Matrix methods for treating optical propagation in an inhomogeneous structure are used widely. An inhomogeneous plasma medium can be treated as a stack of thin homogeneous films extending from *0* to x_n (Figure 3.6),

$$0 \le x \le x_1, x_1 \le x \le x_2, \ldots., x_{n-1} \le x \le x_n$$

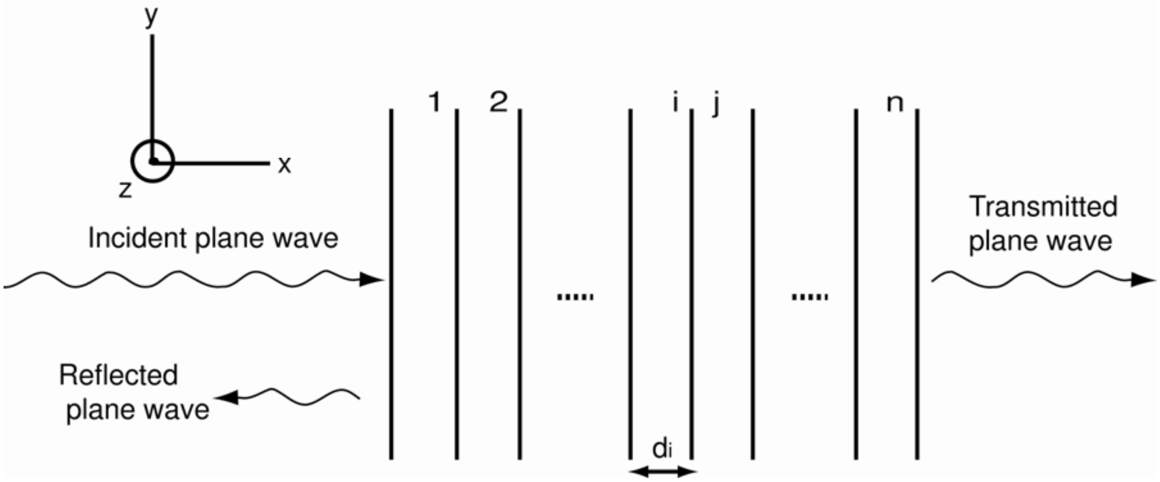

Figure 3.6 The schematics of an inhomogeneous medium that shows the approximation of a continuous dielectric constant change.

Consider a layered system (with layer thickness d_i and complex dielectric constant ε_i), with the *x* axis normal to the layer and with *x-y* as the plane of incidence. As a plane wave travels through the layered media, the component of the wave vector parallel to the interfaces, k_y, is the same in every layer. The forward and backward propagating electric fields in a layer *i* can be written as[53, 54]

$$E_i^{\pm}(r,t) = E_i^{\pm}\exp[(\pm iN_i k_0 x) + (ik_y y - i\omega t)],$$

where the vacuum wave vector magnitude $k_0 = 2\pi / \lambda_0$ and layer index $N_i = k_{ix} / k_0$. The k vector for a free wave propagating in layer i satisfies $k_y^2 + k_{ix}^2 = \varepsilon_i(\omega)k_0^2$, so that $N_i = [\varepsilon_i(\omega) - (k_y / k_0)^2]^{1/2}$.

By matching the tangential components of the electric fields and their associated magnetic field at the interfaces, the relationship between the amplitudes of the E fields to cross the *i-j* interface is derived

$$\begin{pmatrix} E_i^+ \\ E_i^- \end{pmatrix} = \Phi_{ij}\begin{pmatrix} E_j^+ \\ E_j^- \end{pmatrix} \tag{3.38}$$

And Φ_{ij} is the transfer matrix for the i-j interface. Φ_{ij} is a 2x2 matrix defined by

$$\Phi_{ij} = \frac{1}{t_{ij}}\begin{pmatrix} 1 & r_{ij} \\ r_{ij} & 1 \end{pmatrix}. \tag{3.39}$$

Here r_{ij} and t_{ij} are the reflection and transmission amplitudes for light incident upon the *i-j* interface from medium *i*. For S-polarized light the expressions are:

$$r_{ij} = \frac{N_i - N_j}{N_i + N_j}, t_{ij} = \frac{2N_i}{N_i + N_j}, \tag{3.40}$$

and for P-polarized light the corresponding expressions are

$$r_{ij} = \frac{\varepsilon_i N_i - \varepsilon_j N_j}{\varepsilon_i N_i + \varepsilon_j N_j}, t_{ij} = \frac{2n_i n_j N_i}{\varepsilon_i N_i + \varepsilon_j N_j}, \tag{3.41}$$

with $n_{i,j} = \sqrt{\varepsilon_{i,j}}$. The transfer matrix has the following properties: $\Phi_{ij}^{-1} = \Phi_{ji}, \Phi_{ij}\Phi_{jk} = \Phi_{ik}$.

While Φ_{ij} accounts for the propagation across an *i-j* interface, we still need a propagation matrix M_j, which accounts for the phase and amplitude changes in the fields from the left-hand side to the right-hand side of layer *i*. It is given by:

$$\begin{pmatrix} E_i^+(x_i + d_i) \\ E_i^-(x_i + d_i) \end{pmatrix} = M_i\begin{pmatrix} E_i^+(x_i) \\ E_i^-(x_i) \end{pmatrix}, \tag{3.42}$$

where

$$M_i = \begin{pmatrix} \exp(iN_i k_0 d_i) & 0 \\ 0 & \exp(-iN_i k_0 d_i) \end{pmatrix}. \tag{3.43}$$

The inverse propagation matrix, $\bar{M}_i = M_i^{-1}$, propagates the fields from right to left and can be obtained by changing d_i to $-d_i$.

Now, the overall transfer matrix of the fields from the left-hand side of the *1-2* interface to the left-hand side of the *(n-1)-n* interface throughout the layered medium can be written as,

$$T(\omega) = \Phi_{n(n-1)} M_{n-1} \Phi_{(n-1)(n-2)} M_{n-2} \ldots \Phi_{21}. \tag{3.44}$$

The overall reflection and transmission amplitudes for a beam incident from the left are given by:

$$r = -\frac{T_{21}}{T_{22}}, t = \frac{\det(T(\omega))}{T_{22}}, \tag{3.45}$$

where T_{12} and T_{22} are the matrix elements of the 2x2 matrix $T(\omega)$.

Thus the reflectivity, *R*, and transmission, *T*, in terms of *r* and *t* are,

$$R = |r|^2, T = |t|^2, \tag{3.46}$$

and the phase of the reflected wave, φ_r, and transmitted wave, φ_t, relative to the incident wave are,

$$\varphi_r = \tan^{-1}[\frac{\mathrm{Im}(r)}{\mathrm{Re}(r)}], \varphi_t = \tan^{-1}[\frac{\mathrm{Im}(t)}{\mathrm{Re}(t)}]. \tag{3.47}$$

3.5.5 Infrared optical conductivity for aluminum.

The total optical conductivity at 800 nm contains contribution from both bound and free electrons such that the total conductivity $\sigma(\omega) = \sigma_{free}(\omega) + \sigma_{bound}(\omega)$ is the sum of the bound and free electron conductivities. The free electron contribution was described by Drude in Eq.(3.29). Bound (covalent) electron contribution was important because of a strong interband absorption in aluminum at 1.5 eV, which is very close to the experimental interrogation laser wavelength.

Absorption peaks in polyvalent metals arise when the Fermi surface cuts the Brillouin Zone (BZ) faces (Figure 3.7). In general, an absorption edge is expected for each face that is cut and the position of the edge will occur at a photon energy equal to the energy gap appropriate to the particular zone plane [43]. At the BZ boundary in the nearly free electron band structure of fcc aluminum, the first and the second bands are split by the amount determined by the absolute value $U_k(G)$ of the relevant Fourier coefficient of the periodic lattice potential. A pair of bands is almost parallel in BZ planes perpendicular to the two directions $\Gamma - L$ and $\Gamma - X$. The fact that the Fermi surface cuts through these BZ faces, coupled with the parallelism of these bands, result in a kink in a density of states, so called van Hove singularities of the unbroadened joint density of states [43]. This irregularity in a density of states causes optical transitions at energy $2U_k(G)$ (Figure 3.7). Because of differences in the density of states, the $2U_k(111)$ transition at 0.4 eV is weaker than the $2U_k(200)$ transition at 1.5 eV.

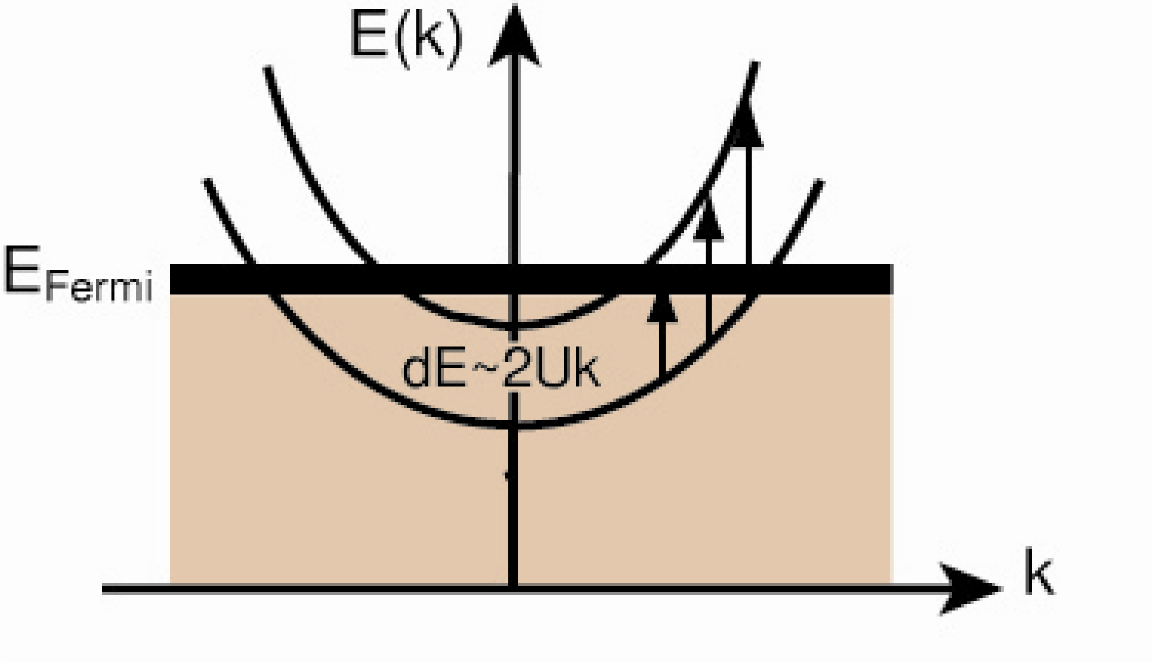

Figure 3.7 Splitting of the degenerate band induced by the periodic lattice potential in aluminum.

Much of the interband absorption effect can be accounted for in a calculation of both real and imaginary parts of the conductivity. Using the weak potential (or pseudopotential) representation of the bands, Ashcroft and Sturm [55] derived the frequency-dependent real and imaginary parts of the conductivity of aluminum. The $\mathrm{Re}[\sigma_{bound}(\omega)]$ and $\mathrm{Im}[\sigma_{bound}(\omega)]$ are functions of relaxation time, τ, and Fourier components of the potential, U_k. The $\mathrm{Re}[\sigma_{bound}(\omega)]$ has a simpler expression involving U_k:

$$\mathrm{Re}[\sigma_{bound}(\omega)] =$$

$$\sigma_a(a_0K)\left|\frac{2U_k}{\hbar\omega}\right|^2 \left\{\left[1-\left(\frac{2U_k}{\hbar\omega}\right)^2-\left(\frac{1}{\omega\tau}\right)^2\right]^2+\frac{4}{\left(\omega\tau\right)^2}\right\}^{-1/4} \frac{\left(\omega\tau\right)^2}{1+\left(\omega\tau\right)^2}J(\omega) \tag{3.48}$$

Where $\sigma_a = (e^2/a_0\hbar)(24\pi)^{-1}$ and K is the magnitude of the reciprocal-lattice vector. The function $J(\omega)$ is defined:

$$J(\omega) =$$

$$\frac{4zb\rho}{\pi(z^2+b^2)}\tan^{-1}t_0+\frac{1}{2\pi}\left(\frac{z^2-b^2}{z^2+b^2}\cos\phi+\frac{2zb}{z^2+b^2}\sin\phi\right)\ln\left(\frac{t_0^2+2t_0\rho\sin\phi+\rho^2}{t_0^2-2t_0\rho\sin\phi+\rho^2}\right), \tag{3.49}$$
$$+\frac{1}{\pi}\left(\frac{z^2-b^2}{z^2+b^2}\sin\phi-\frac{2zb}{z^2+b^2}\cos\phi\right)\left[\tan^{-1}\left(\frac{t_0+\rho\sin\phi}{\rho\cos\phi}\right)+\tan^{-1}\left(\frac{t_0-\rho\sin\phi}{\rho\cos\phi}\right)\right]$$

where

$$z = \hbar\omega/2\left|U_k\right|, b = \hbar/(2\tau\left|U_k\right|)$$
$$\phi = \frac{1}{2}\left[\frac{1}{2}\pi-\tan^{-1}\left(\frac{1+b^2-z^2}{2bz}\right)\right].$$
$$\rho^2 = [(1+b^2-z^2)^2+4z^2b^2]^{1/2}$$
$$z_0 = \hbar\omega_0/2\left|U_k\right|, t_0 = (z_0^2-1)^{1/2}$$

The $\mathrm{Im}[\sigma_{bound}(\omega)]$ is more complex than Eq.(3.48) and has the following expression :

$$
\begin{aligned}
&\mathrm{Im}[\sigma_{bound}(\omega)] = \sigma_a (a_0 K)\frac{1}{2b\pi\rho} \\
&(\frac{1}{2}\sin\phi_1 \ln\left(\frac{z_0^2-1+2(z_0^2-1)^{1/2}\rho\cos\phi_1+\rho^2}{z_0^2-1-2(z_0^2-1)^{1/2}\rho\cos\phi_1+\rho^2}\right)+ \\
&\cos\phi_1\left[\tan^{-1}\left(\frac{(z_0^2-1)^{1/2}+\rho\cos\phi_1}{\rho\sin\phi_1}\right)+\tan^{-1}\left(\frac{(z_0^2-1)^{1/2}-\rho\cos\phi_1}{\rho\sin\phi_1}\right)\right]+ \\
&\frac{b^2-z^2}{b^2+z^2}\{\frac{4bz\rho}{b^2+z^2}\tan^{-1}(z_0^2-1)^{1/2}+\frac{1}{2}\left(\frac{z^2-b^2}{z^2+b^2}\cos\phi_2+\frac{2zb}{z^2+b^2}\sin\phi_2\right) \\
&\ln\left(\frac{z_0^2-1+2(z_0^2-1)^{1/2}\rho\cos\phi_2+\rho^2}{z_0^2-1-2(z_0^2-1)^{1/2}\rho\cos\phi_2+\rho^2}\right)+\frac{z^2-b^2}{z^2+b^2}\left(\sin\phi_2-\frac{2zb}{z^2+b^2}\cos\phi_2\right) \\
&\left[\tan^{-1}\left(\frac{(z_0^2-1)^{1/2}+\rho\cos\phi_2}{\rho\sin\phi_2}\right)+\tan^{-1}\left(\frac{(z_0^2-1)^{1/2}-\rho\cos\phi_2}{\rho\sin\phi_2}\right)\right]\})
\end{aligned}
\tag{3.50}
$$

Where

$$
\phi_1=\frac{1}{2}\left[\frac{1}{2}\pi+\tan^{-1}\left(\frac{1+b^2-z^2}{2bz}\right)\right], \phi_2=\frac{1}{2}\left[\frac{1}{2}\pi-\tan^{-1}\left(\frac{1+b^2-z^2}{2bz}\right)\right]
$$

$$
\rho^2=[(1+b^2-z^2)^2+4z^2b^2]^{1/2}
$$

The $\mathrm{Re}[\sigma_{bound}(\omega)]$ and $\mathrm{Im}[\sigma_{bound}(\omega)]$ are sensitive to the relaxation time τ, that is depended on a temperature (3.21). Figure 3.8 shows the conductivity at 800 nm as a function of the collision frequency, $\nu=1/\tau$. As can be seen from the graph, the $\mathrm{Re}[\sigma_{bound}(\omega)]$ is more than a factor of two larger than $\mathrm{Re}[\sigma_{drude}(\omega)]$ at room temperature, where the value of the aluminum collision frequency is 8.5*10^{14} s^{-1} [38].

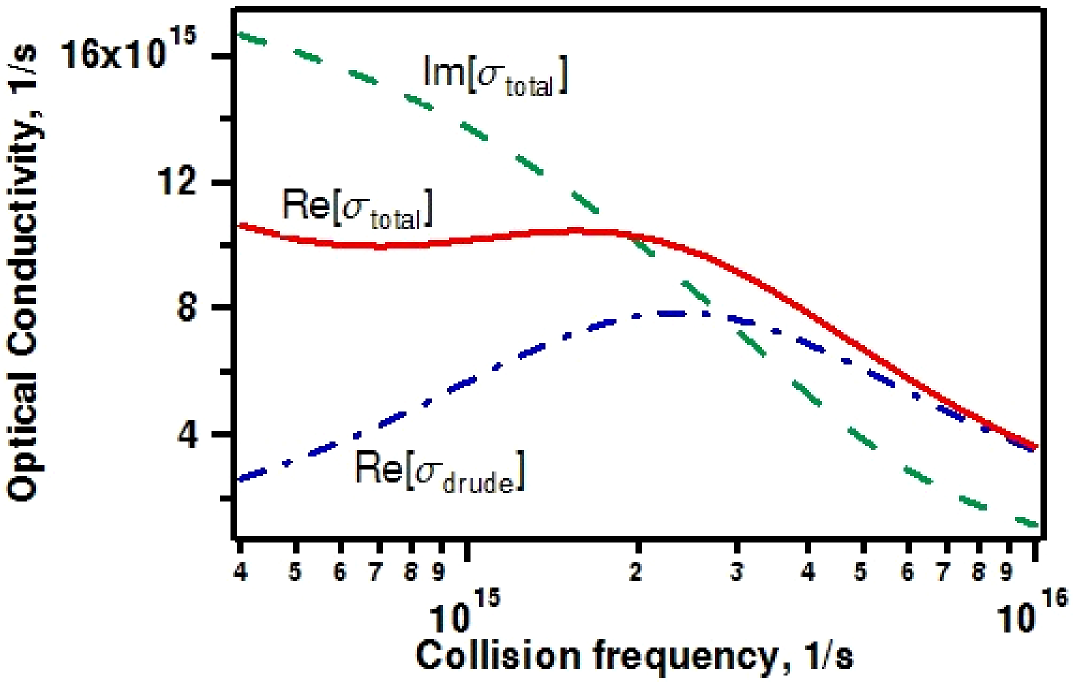

Figure 3.8 Optical conductivity at 800 nm of aluminum as a function of collision frequency.

Both the pressure and temperature dependences of the 1.5 eV interband transition have been studied. Tups and Syassen [56] measured the pressure-dependence of the transition and found that it shifts to a higher photon energy at an initial rate of $4.35 \pm 0.3 meV / kbar$, reflecting the increase in pseudopotential form factors (U_k) with compression. The temperature variation in the range of 0-552 K (0-0.05eV) was found to be consistent with expected influence of the Debye-Waller factor and volume changes [57]. This measurement was done at temperatures below the melting temperature, where the U_k changes were found to be less than 1% at temperatures above room temperature.

4 Experimental Setup

4.1 REFLECTIVITY OF LAYERED TARGETS

A pump-probe measurement was designed to study the electron thermal conduction mechanism in laser-heated thin films. The experiment was designed to measure the back surface reflectivity of a heated thin metal film. To be able to obtain reliable Equation of State (EOS) information from the heated target, it was necessary to create heated matter at a uniform density and temperature. It is hard to reach this single state when laser-heated matter is non-uniform; in that case it involves transits through multiple states. It has been proposed to use a very thin film of the order of 20-30 nm to create a single-state plasma, that will exist only within few hundreds of femtosecond after the heating laser pulse gets absorbed. The single-state measurement is crucial when heated matter is probed in extreme ultraviolet (5 nm-40 nm), resulting in one tenth of a nanometer probe beam absorption. We manufactured a thin film target using an aluminum vapor deposition process.

A 40 nm Al film was deposited on top of the commercially available 0.4x3mm copper slit coated with 39nm formvar/carbon support layer (Ted Pella SEM grids) (Figure 4.1) using the vapor deposition technique available in the Cryo Shop of the Physics department. The formvar layer of 35 nm stabilized with a 4 nm carbon layer provided strength to the support layer and was not destroyed during the metal deposition, unlike a formvar-only support layer. The thickness of the aluminum layer that was produced was measured with a Wyko optical profilometer and found to be 40 nm (Figure 4.2). The optical profilometer is designed to measure the surface roughness using coherence scanning interferometry for producing 3D images of the surface. Using the mask, the stripe of the aluminum film was deposited on a glass substrate in the same time as Al film was deposited on targets. The thickness of the deposited Al film was determined by measuring the surface profile of the prepared film on a glass substrate.

To confirm the solid density of the deposited film, X-ray-reflectrometry was used and produced a measurement of 2.8 g/cm^3 density for the film. Transmission electron microscope (TEM) measurement showed that this film was polycrystalline and made of 20-40 nm well-packed grains (Figure 4.3). To be able to produce free standing foil the formvar layer had to be dissolved in ethylene dichloride solution. Due to the small thickness of the aluminum film and its grain structure, the film was affected by the solution and destroyed during the etching. Taking into account that the formvar layer is transparent to visible light, the 400nm light will get absorbed in carbon/aluminum layer. Despite these difficulties, the layered target was used in the experiment.

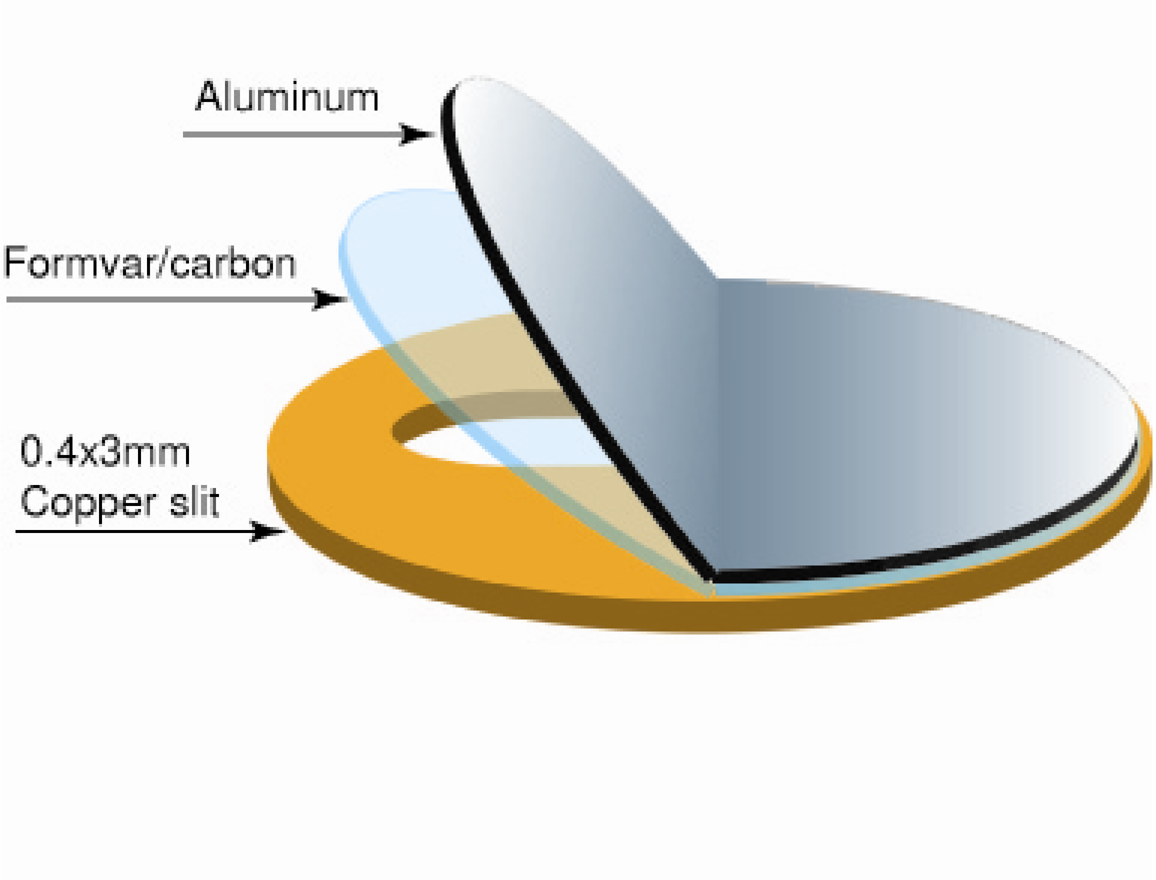

Figure 4.1 The view of the 40 nm aluminum foil that was created on top of copper slit coated with 39nm formvar/carbon layer.

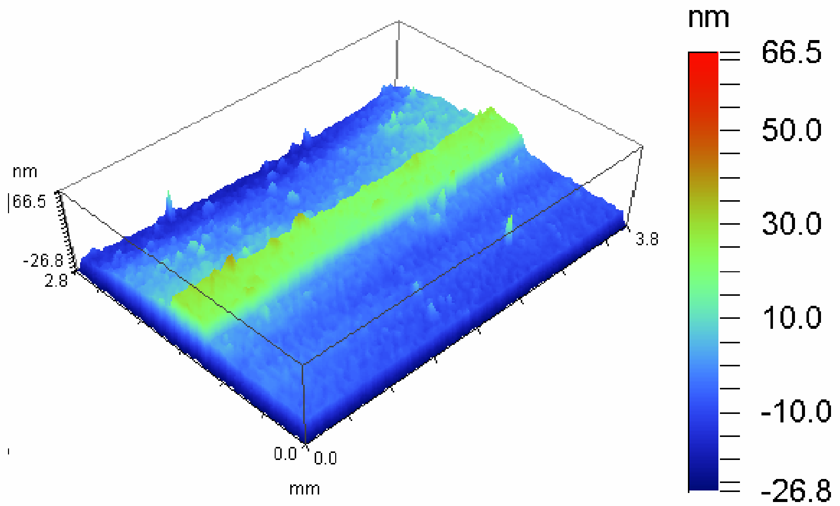

Figure 4.2 Optical profilometry image of aluminum film (green) deposited on a substrate (blue).

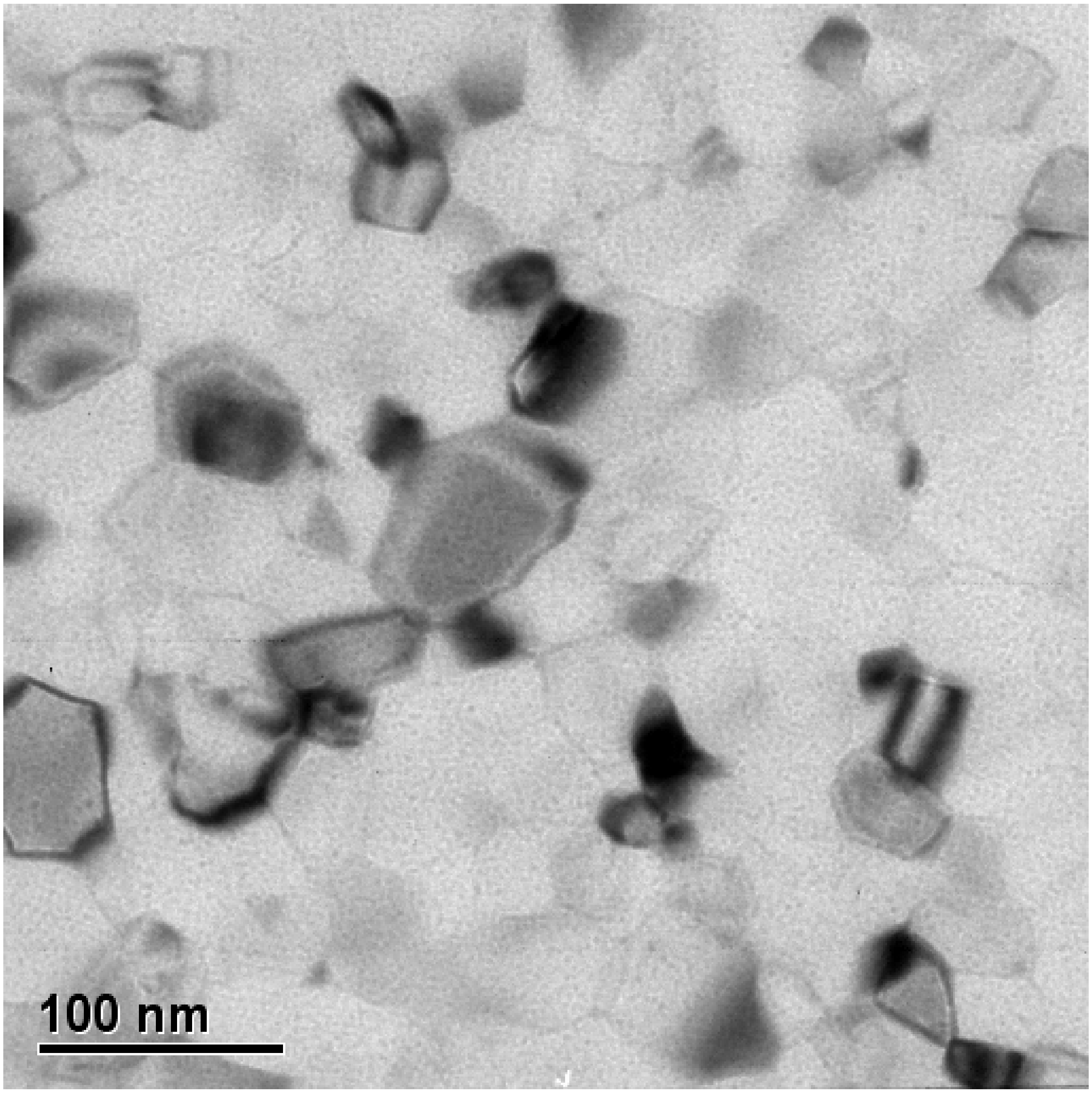

Figure 4.3 TEM image of the aluminum film shows polycrystalline structure with a grain size of 20-40 nm. Moire fringes are visible when differently oriented grains are stacked on top of each other.

The slits were arranged in an array of eight on GridStick supports (Ted Pella). Five grid sticks were arranged in a target holder, making total of 40 slits (grids) per target (Figure 4.4). Since the target was made of numerous grids (slits) arranged individually it was important to control the vertical and horizontal tilt of the target holder, correcting for the non-uniformity of the arrangement. The target holder was mounted in a modified mirror mount with motorized vertical and horizontal tilts and position on top of a three axis motorized translational stage.

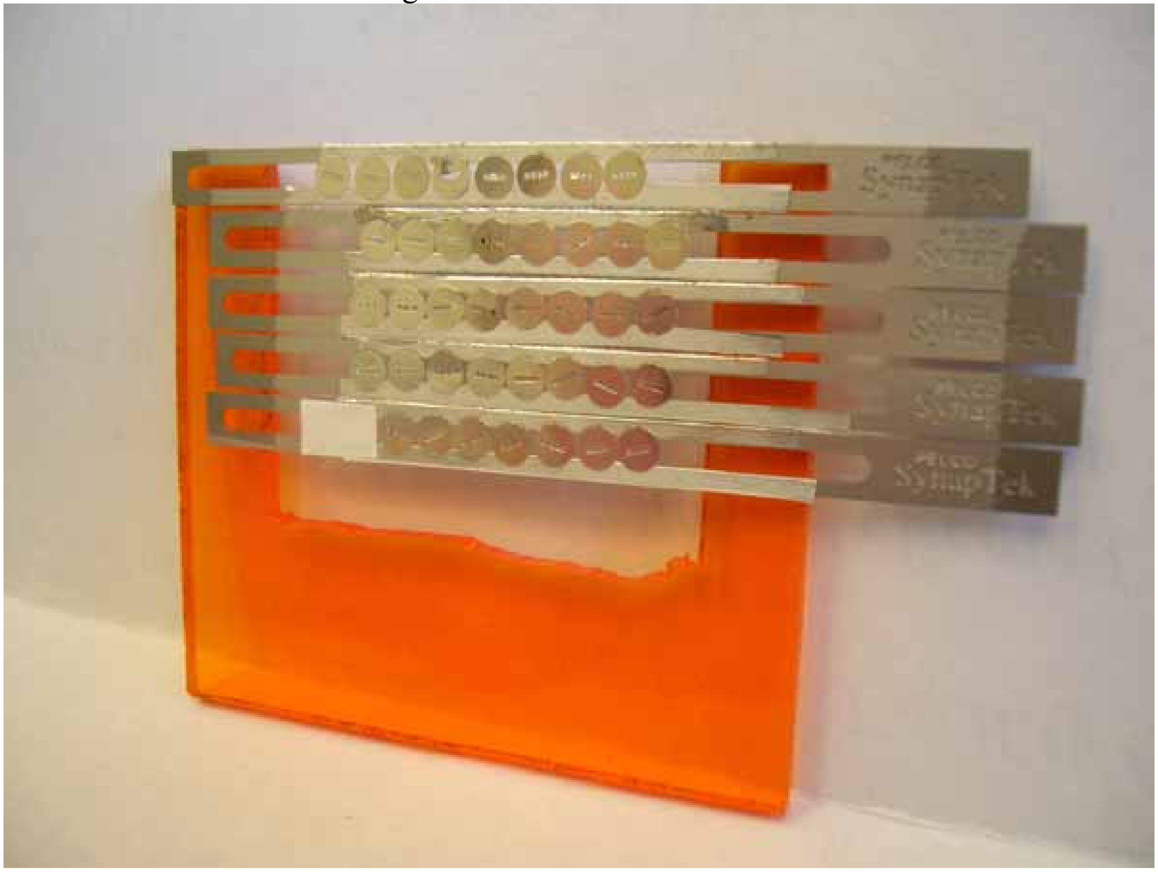

Figure 4.4 The arrangement of the slits in a target.

The experimental layout is shown in Figure 4.5. The 35 fs output of the THOR laser was delivered into the blue vacuum chamber. The beam was split into an energetic 0.5 mJ heating pulse and probe pulse, the latter of which was frequency-doubled and filtered to produce a 0.05 μJ pulse at 400 nm. A 1 mm thick KDP crystal was used to frequency-double the probe. The 800 nm light was filtered out with a dichroic mirror installed after the KDP crystal and blue glass filter. The final FWHM of the 400nm probe beam was estimated by accounting for the group velocity dispersion of a Gaussian beam propagating through the additional dispersive media (the KDP crystal and the glass filter). The Sellmeier equation was used to determine the wavelength dependent index of refraction for each element, leading to a calculated probe pulse width of 58 fs.

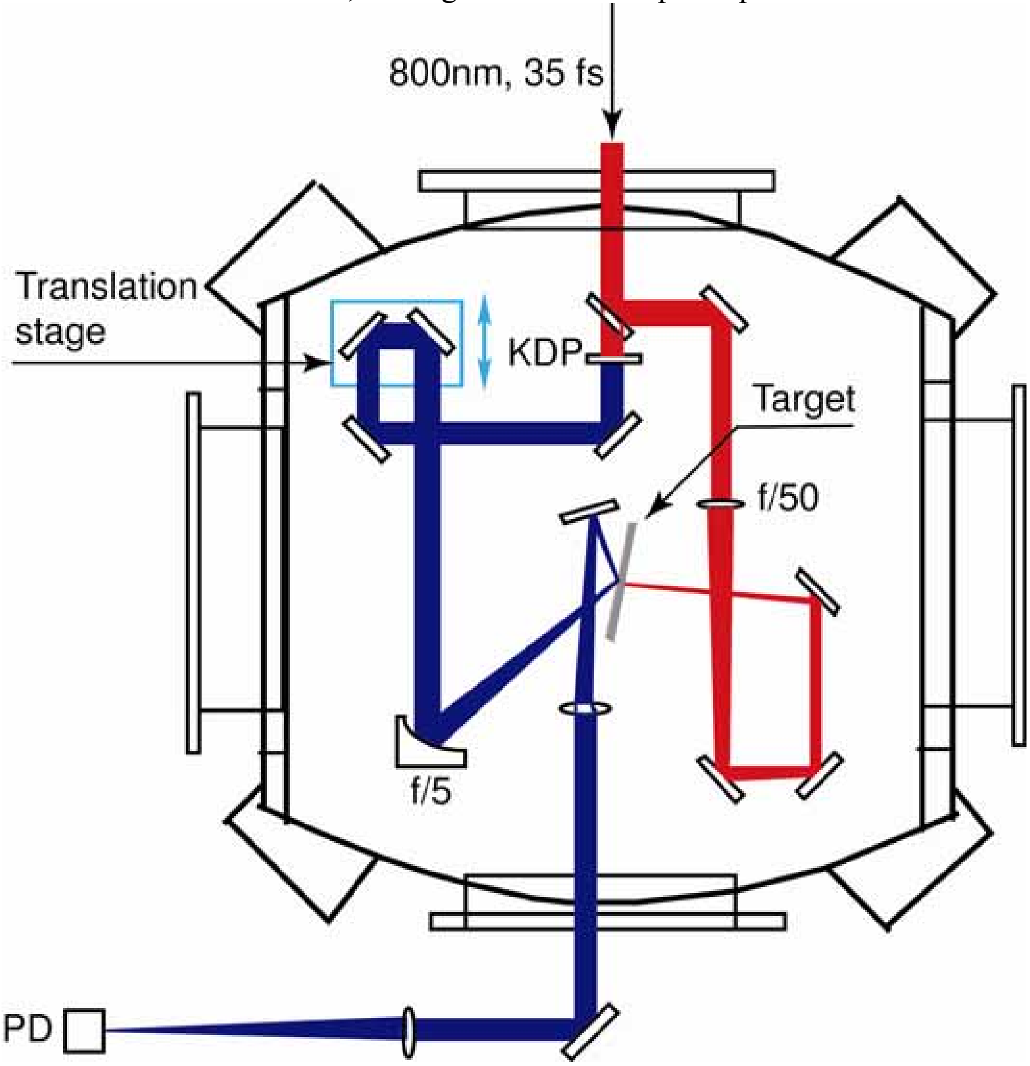

Figure 4.5 The layout of the optical set-up for measuring back surface reflectivity of the heated aluminum foil deposited on a support layer. PD is photodiode.

The front side of the target was heated with an 800 nm pulse at an intensity of $5*10^{13}$ W/cm^2. The intensity range below 10^{14} W/cm^2 at 800 nm was chosen to avoid any target modification by the pre-pulse before the main pulse arrival. As shown in

Chapter 2, the pulse to pre-pulse contrast ratio at 800 nm was approximately 10^4. The focal spot diameter was 120 μm. The p-polarized pump beam was incident at 5 degrees to the normal in order to eliminate the vacuum heating effect [17, 58].

The 400 nm probe was incident from the rear side of the aluminum foil at 55 degrees to normal, allowing the time resolution of the delay between the pump and the probe of 250 fs. The 58 fs, $3*10^9$ W/cm^2 intensity, s-polarized probe was focused to a smaller spot size of 60 μm diameter. The probe intensity was kept sufficiently below the damage threshold of the target. The use of the 400 nm probe wavelength allowed for improved discrimination from the 800 nm pump. The reflected probe beam from the back surface of the target was collimated and taken outside of the chamber and focused onto a photodiode. Several 400 nm interference filters were used to eliminate stray 800 nm light. Positioning the photodiode outside of the chamber allowed the signal to be optimized prior to every shot.

The delay line installed in the probe beam pass allowed me to change the delay between the heating beam and the probe in steps of 200 fs. Since the angle between the probe and the pump beams in the interaction region was 135 degrees, it was not straightforward to determine the zero time delay between the probe and the heating beams. Several steps were required in order to find the zero time overlap. First the KDP crystal was removed from the probe beam and the zero time delay between the same color probe and heating pulses was found by building en extra beam line that made a 90 degree overlap with the heating beam within the interaction region (Figure 4.6). The extra beam line was built by splitting a portion of the heating beam. Using the KDP crystal the zero time delay was first found between the heating and extra line beams, by adjusting the delay line built into the extra line beam pass. Then the zero time delay was found between the 800 nm probe beam and extra line beam by adjusting the delay line built into the probe pulse pass. Now when the heating and probe beams were roughly overlapped, the zero time overlap in the interaction region was found by imaging to the interaction region with a long focal length telescope on a ccd camera. The intensities of both pulses were kept slightly below the air ionization threshold just to be able to see them with the camera. By slowly changing the time delay between the heating and the probe beams it was possible to observe with the naked eye (not taking into account safety goggles) the intensity of the two overlapped beams drastically increase when the beams were temporally overlapped. The zero time delay between the pulses was determined within the pulse length of the beams. Before running the experiment, the KDP crystal was installed in the probe beam line, the introduced time delay was calculated, taking into account the thickness of the 1 mm thick crystal. The time delay associated with the filter blocking the 800 nm light was determined experimentally. Taking into account the angle of incidence of the probe beam and the error of the zero time determination, the final time resolution between the heating beam and the 400 nm probe was of the order of 300 fs.

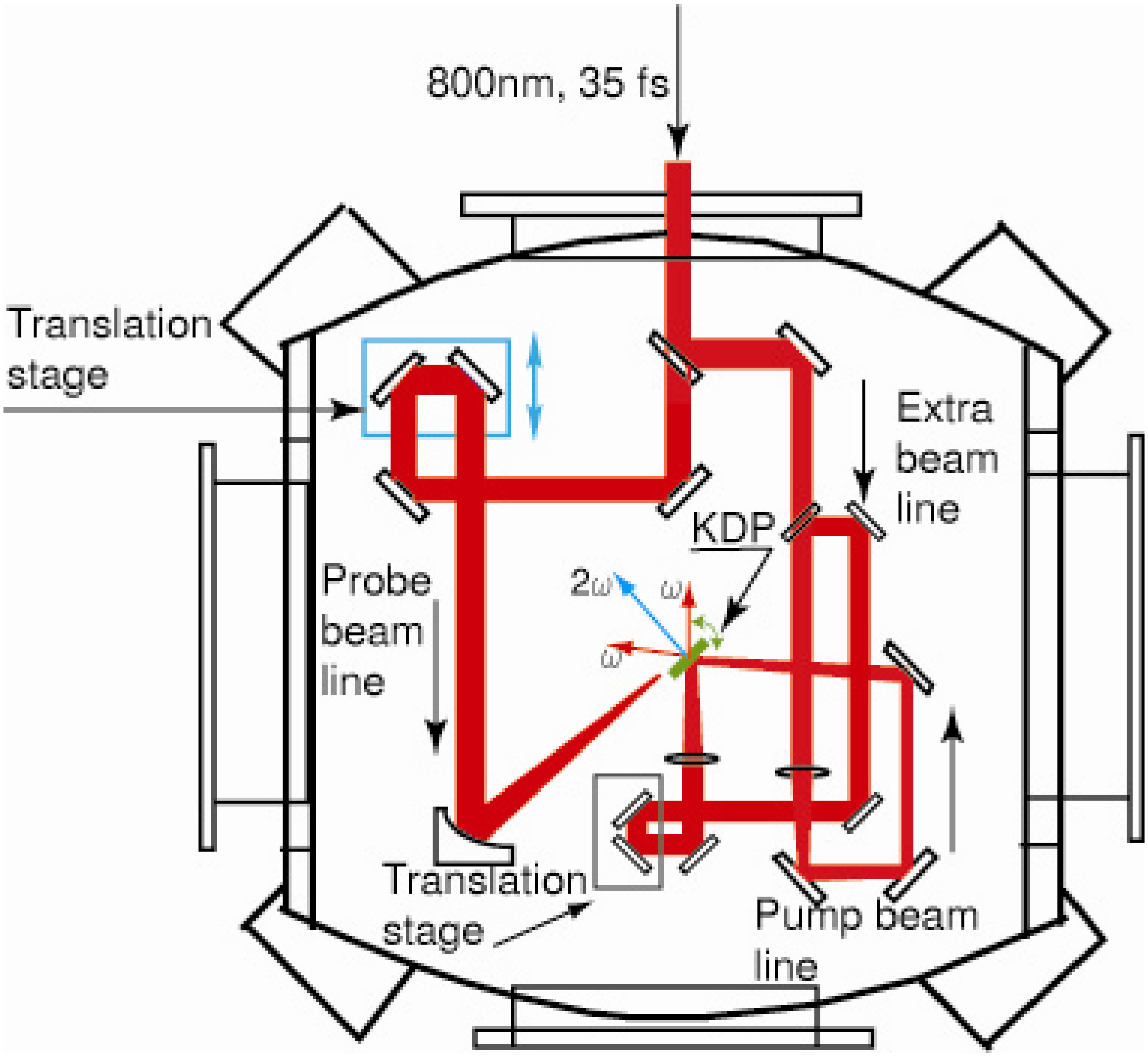

Figure 4.6 The layout of the set-up build to find a zero time delay between the probe and pump pulses.

4.2 SINGLE-SHOT EXPERIMENT ON A FREE STANDING FOIL

Most ultrafast heating experiments have been performed on thin films deposited on top of substrates where both the energy transport effects and shock-induced effects due to the substrate were a concern [25, 26, 49, 59]. The use of a free standing foil eliminated the induced effect due to the substrate and allowed us to study the electron thermal conduction mechanism in a two-temperature dense plasma.

4.2.6 Target

Free standing 200-400 nm aluminum foils were manufactured for use as the targets. The targets were made by depositing aluminum onto a silicon on insulator wafer (SOI) manufactured by Ultrasil corporation. We used SOI wafer (Figure 4.7) composed of a 2 μm silicon device layer, 2 μm silicon dioxide layer and 500 μm silicon handle layer with a <100> orientation. The SOI wafer was polished on both sides.

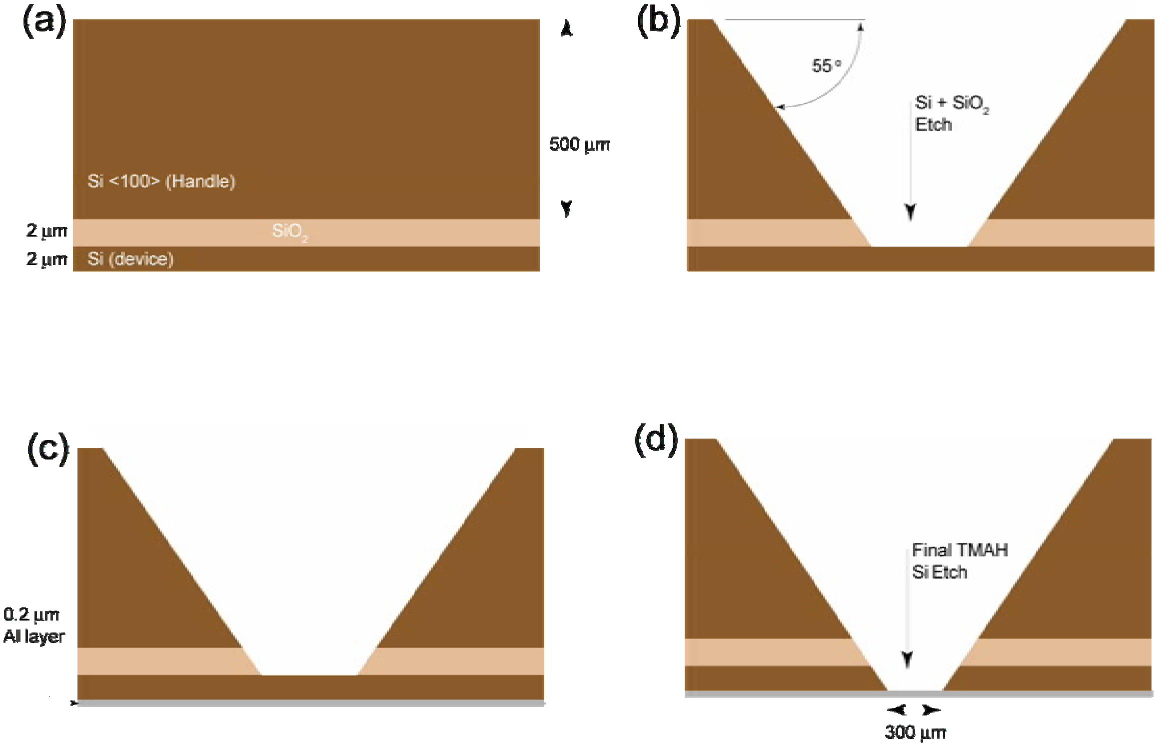

Figure 4.7 Target Creation Procedure – (a) Ultrasil Wafer, as purchased (b) Si and SiO$_2$ etching steps remove Si Handle and SiO2 layer. (c) aluminum layer was formed via vapor deposition (d) Final TMAH etch was used to remove Si device layer.

The grid pattern exposing the device layer was made on a SOI wafer before depositing the aluminum layer (Figure 4.7(b)). The grid-making technique was developed and used for our targets by Byuong-Ick Cho [60].

The aluminum vapor was deposited on top of the Si wafer in Cryo Shop on the 3rd floor of the physics building. The metal layer that was produced had a solid density of 2.7 g/cm^3. The free standing foils were made by etching away the 2 μm Si device layer. The etching technique is described in reference [61]. This technique allowed me to anisotropically etch the silicon in 5% tetra-methyl ammonium hydroxide (TMAH) solution, while the leaving deposited aluminum film unaffected. The TMAH solution was prepared following Pandy's recipe, where higher a concentration of dissolved Si in the solution was chosen to protect a deposited aluminum. For 1.5 l of 5% TMAH, solution more then 50 g of crushed Si were dissolved at 80 ^{0}C. The PH level of the etchant was monitored during Si dissolution. The PH level of the solution defined the etch level of Si and Al. The goal was to reach 11.6 PH which allowed me to minimize the Al etching rate to $\ll 1\mu m / hour$ and to reach $5-10\mu m / hour$ etching rate for Si. Using crushed Si, I was able to dissolve Si and to reach desirable PH level in the solution within 6 hours. During this time the temperature was monitored and maintained at 80 ^{0}C. After the solution was prepared, the target (Figure 4.7 (c)) was placed in the prepared solution for 20 min in order to dissolve $\sim 2\mu m$ of Si device layer and expose the aluminum film (Figure 4.7 (c)). The process would ideally produce an array of 96 free standing 300x300 μm aluminum films. In reality, the process produced around 85 useful targets, a yield of about 90 %(Figure 4.8). The Al film thickness was characterized by looking at the cross section of the target with the scanning-electron microscope (SEM). Targets with the 170, 230 and 375 nm aluminum foils were produced (Figure 4.9).

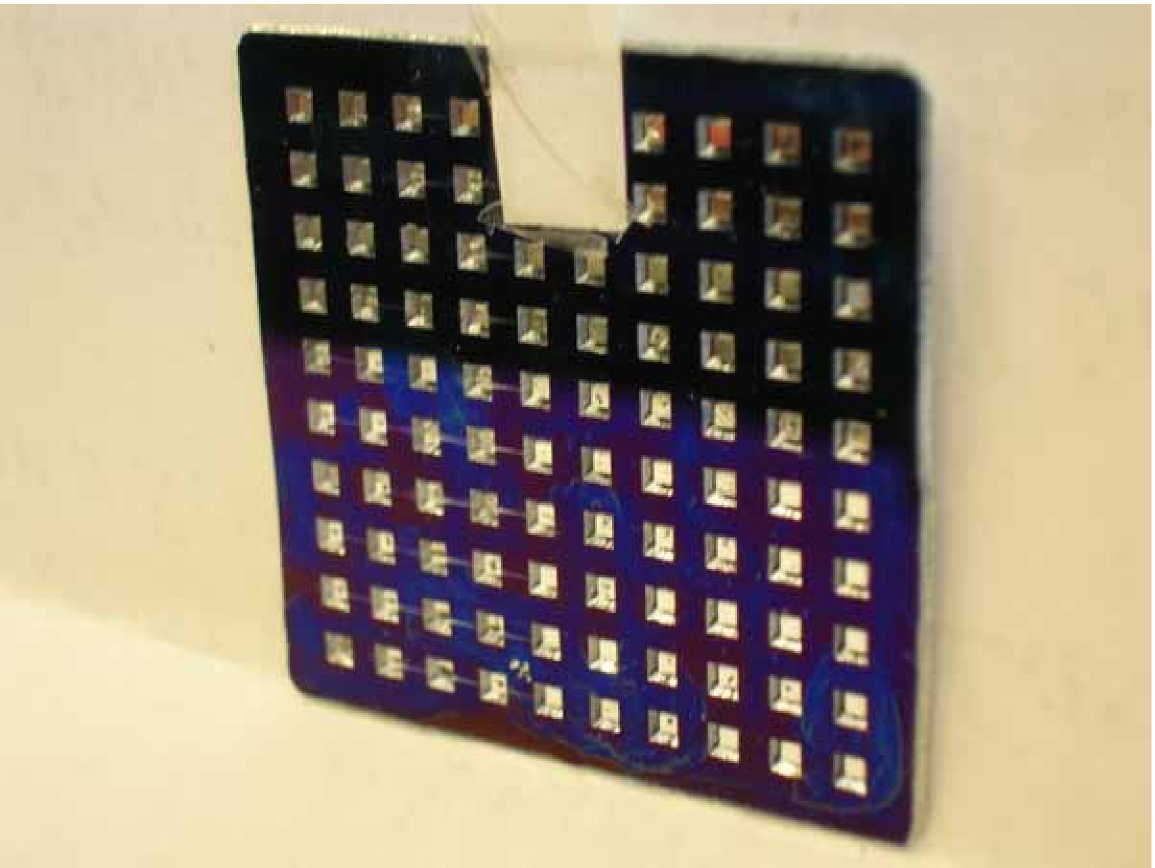

Figure 4.8 The silicon wafer grid pattern exposing the aluminum film.

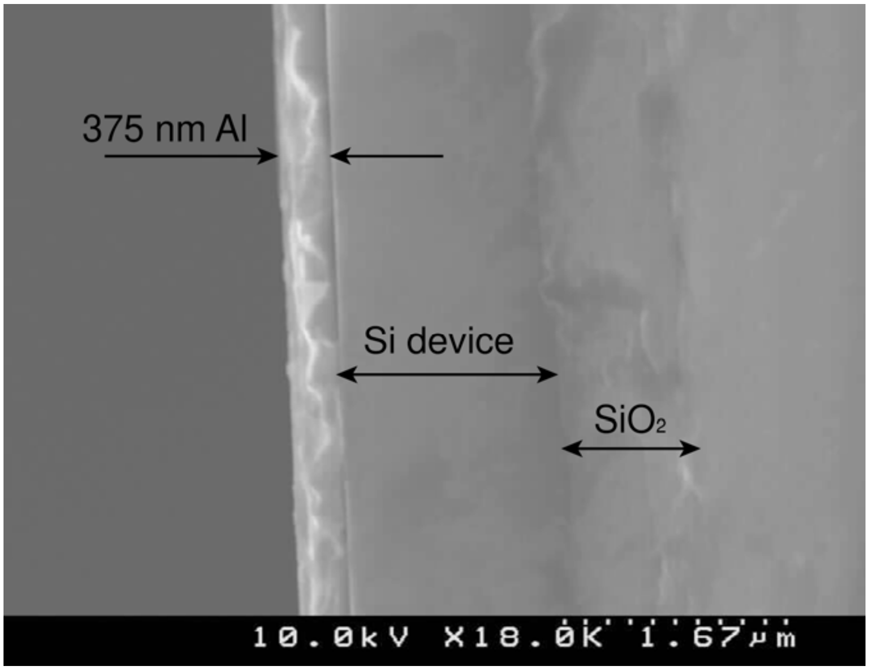

Figure 4.9 SEM image of aluminum foil on top of the SOI wafer.

4.2.7 Experimental setup

Most experimental efforts to understand transient effects in dense plasmas have employed a pump-probe technique, whereby the optical constants (reflectivity, phase shift, transmissivity) of metal are probed immediately after absorption by an intense ultrafast pump [14-19, 21-23, 26, 36, 48-50, 62-65]. Many experiments that have implemented this technique were done using femtosecond laser absorption measurements [14-17], and have studied the hot expanded states of the front surface of the laser heated target [18, 19, 65]. To study charge and thermal transport, electrical conductivity has been derived from optical reflectivity measurements of laser heated solids [20, 22, 23]. To study energy transport in a transparent target, the supersonically moving steep ionization front was measured [50, 62] . Transient thermal nonequilibrium between electrons and ions has also been studied in experiments on slab targets using shock waves driven by femtosecond duration laser pulses[25-27, 49]. Slab targets were used in this experiment to measure the average shock velocity and particle velocity at an Al/SiO2 interface. On the other hand, femtosecond laser pulses induced a limited rate of energy exchange between electrons and ions which gives rise to novel phenomena such as electron thermal conduction waves in a two-temperature, dense plasma. In order to observe the thermal conduction wave in two-temperature dense plasma, it has been proposed to probe the back surface of the femtosecond laser heated metal foil [24]. When the laser energy is deposited directly into the metal film, it is possible to observe solid heating that is dominated by the electron thermal conduction in dense matter. That is contrary to laser shock experiments in which the solid is heated by laser driven pressure pulses.

To be able to determine the dielectric function of the solid heated material generated by the thermal conduction from the heated front surface both reflectivity and phase shift changes of the reflected probed had to be measured. The experimental set up described earlier was designed to measure only reflectivity changes of the reflected probe. Another drawback of the previous experiment designed is that the time dependent changes of the measured reflectivity had to be reconstructed by changing the time delay between the pump and probe pulses. It is desirable to be able to obtain the time-dependent measurement in a single shot. It will allow us to eliminate measurement's errors due the changes in the target surface from shot to shot, as well as to avoid pulse to pulse averaging. To measure both reflectivity and phase shift changes of the reflected probe from heated solids in a single shot frequency domain interferometry technique was used to design the following experiment.

We designed a single-shot pump-probe experiment to study the dynamics of a solid density plasma. Probing the back surface of the heated target, the reflectivity and the phase shift changes of the reflected probe pulse were measured simultaneously. All experimental work was done using the THOR laser. The target was placed in a vacuum chamber at $5*10^{-5}$ Torr. The target was heated at the front, and the probe beam was incident at the back surface of the target immediately after the pump pulse. Figure 4.10 shows the target orientation during the shooting. Frequency-domain interferometry (FDI) was implemented with temporally chirped pulses to probe the evolving plasma, allowing dynamics to be captured in a single shot. The schematic of experimental set up is shown in Figure 4.11.

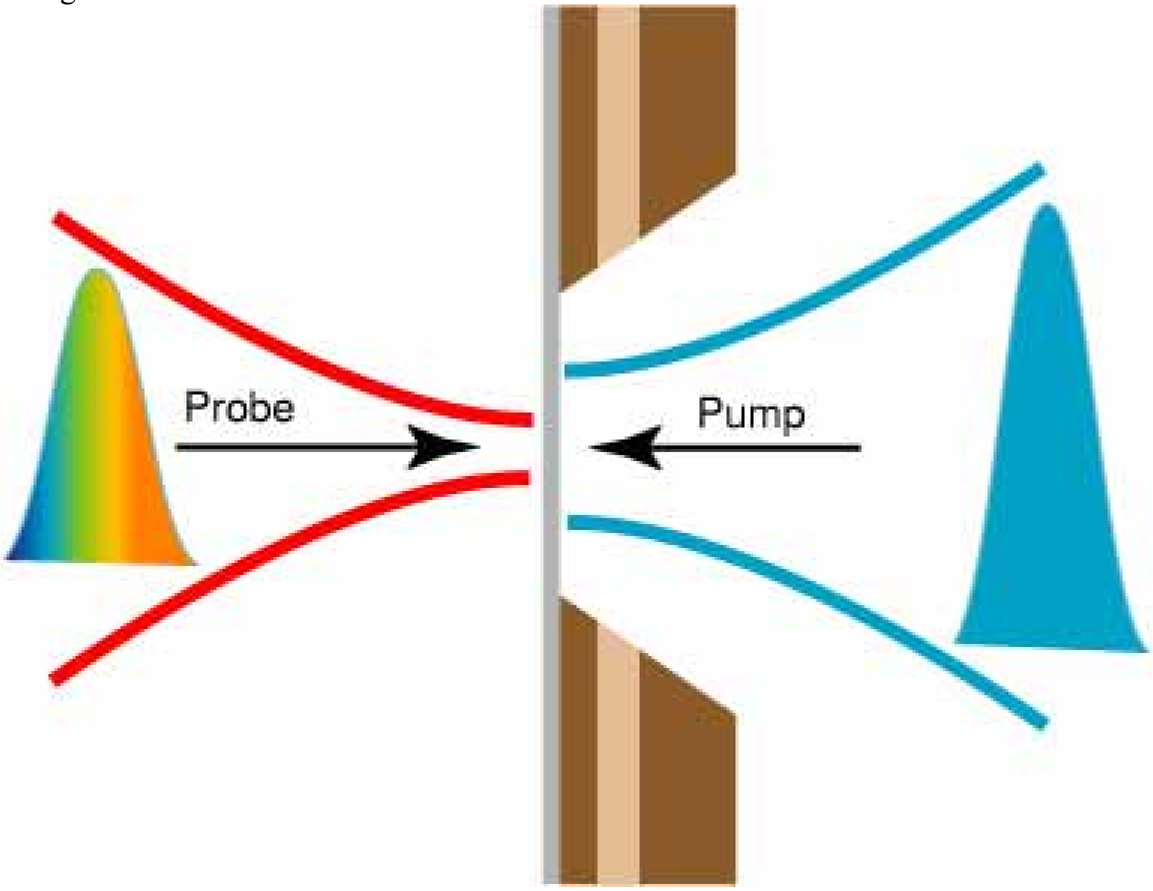

Figure 4.10 The close up shot of the target orientation relative to the laser beams.

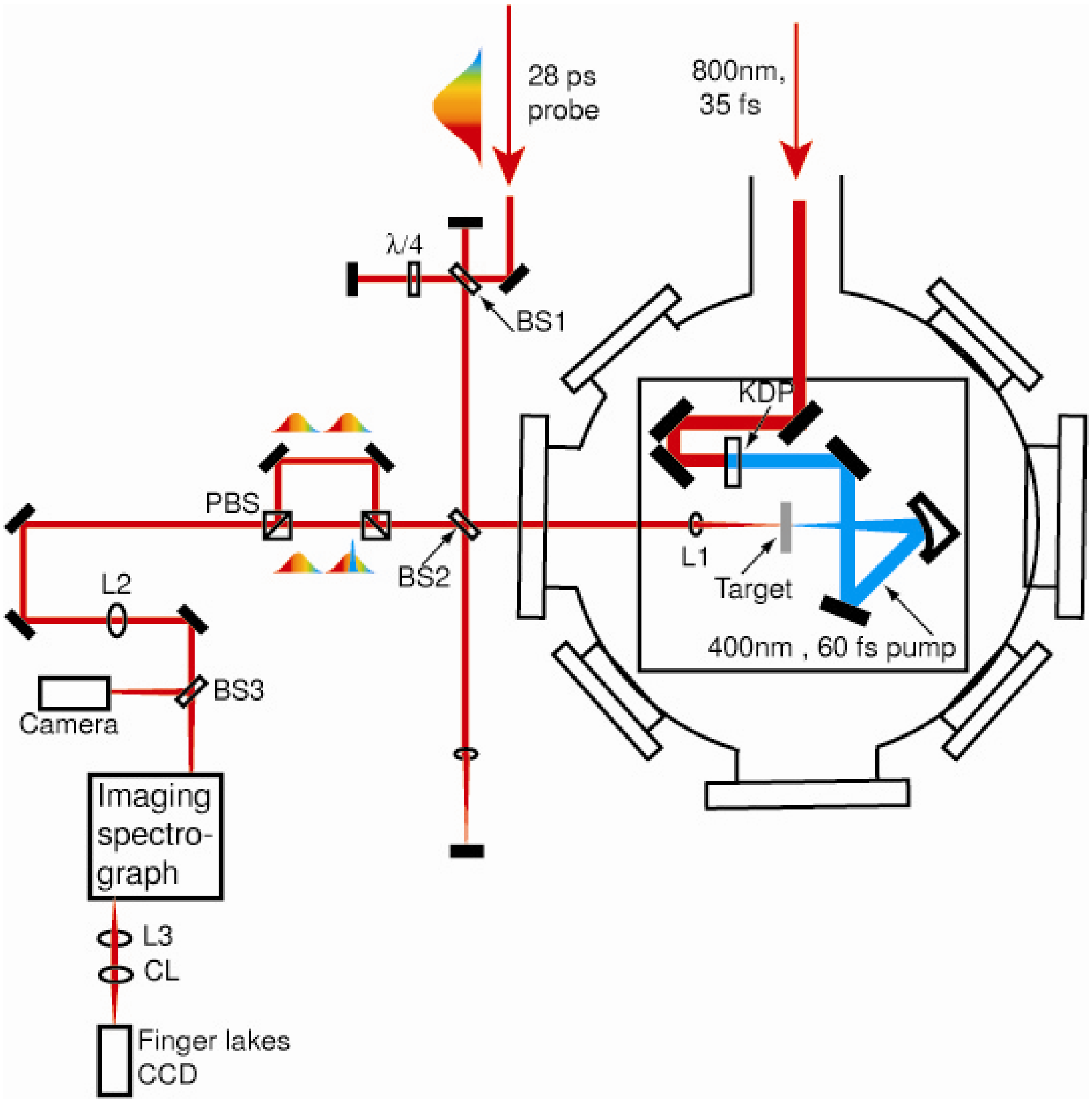

Figure 4.11 Schematics of the experimental set-up for optical probing of heated metal foil using single shot FDI technique. BS is a beamsplitter, PBS is a polarized beamsplitter, L is a lensm CL is a cylindrical lens.

The main laser beam was compressed to 35 fs. It was delivered to the blue chamber that was coupled to the vacuum compressor trough the switchyard (Figure 2.2). The 800 nm beam was frequency-doubled with 1 mm thick, 50 mm diameter KDP crystal to get a 0.5-1.5 mJ heating pulse at 400 nm. Using the second harmonic of the fundamental pulse allowed us to improve the main-to-prepulse contrast up to 10^8 and eliminate the concern of prepulses that are intense enough to modify the target. The fundamental frequency was eliminated by reflecting the 400nm beam from dichroic beam splitter that transmitted 800 nm and using the blue glass filter. The 50 mm diameter pump beam was focused with the f/4 parabola on the front surface of the target at normal incidence. The FWHM of the final pump beam was estimated using methods similar to those described in the previous section and found to be 70 fs.

The probe pulses were generated from the main pulse by inserting a beam-splitter after the 5 pass. The pulse width of the probe was adjusted by changing the grating separation in the air compressor. To get a 28 ps probe pulse, the distance between the gratings was reduced by 90 mm. The roof-top high reflector had to be adjusted by 95 mm to compensate for the beam shift. To characterize the sub-ps pulse's length the second order autocorrelation measurement is usually done. By increasing the overlap angle of the two beams on a KDP crystal it was possible to measure up to 5 ps pulses. To characterize 28 ps pulse the 35 fs compressed limited pulse was coupled to the 28 ps pulse and send to the spectrometer. Changing the time delay between those two pulses it was possible to estimate the pulse width of the chirp pulse as well as to measure the chirp of the probe pulse. The latter was used for the temporal phase and reflectivity determination (See Chapter 5).

The 28 ps probe pulse was attenuated by decreasing the beam size from 25 mm to 11 mm with the use of an apodizer before the spatial filter for the air compressor. The wedge installed in a transport line, as well as a set of absorptive glass ND filters, used to keep the energy of the probe pulse below the damage threshold of the aluminum target. The attenuated beam was sent to the interferometer (Figure 4.11) build outside of the chamber. The probe beams were coupled to the chamber through the side window and normally incident on the back surface of the target. The beams were focused with an f/18 lens to 40 um with the intensity below 10^{10} W/cm^2. The pump beam was defocused to 150 μm in order to ensure that the probe beam spot was smaller. Since the interferometer was mounted outside of the chamber on a separate table, the beam overlap was sensitive to the chamber vibration. To eliminate the effect of missed overlap the focusing lens for the probe (L1) was positioned inside the chamber.

4.2.8 Interferometer

We used frequency-domain interferometry (FDI) to probe the back surface of the heated foil [28, 66]. In FDI each wavelength of the mode-locked pulse has a specific time associated with it, so changes in the spectral signal are used to identify changes in time. The 28 ps chirped reference and probe pulses were long enough that the spectrally-resolved interference pattern could capture the full scale of the reflectivity and phase shift changes in a single shot. Our FDI setup is shown in detail in Figure 4.11.

The interferometer was designed to be able to measure simultaneously both the reflectivity and the phase shift of the probe. To achieve this, the beam was divided into two pairs of interfering pulses: a signal pair and a background pair. The background pair arrived 120 ps before the pump, and the signal pair was temporally overlapped with the pump.

Two unbalanced Michelson interferometers were used to separate the original pulse into two pairs of probe pulses. The first beam splitter (BS1) created the signal and background pulses. A quarter wave plate ($\lambda/4$) was placed into one of the arms of the first interferometer. After recombining in the first beamsplitter the two pulses were orthogonally polarized and separated by 120 ps – they could no longer interfere. The second beam splitter (BS2) separated each of the orthogonally polarized pulses into a reference and probe pulse pair. Both probe pulses were directed to the arm of the interferometer containing the target. Once interacting with the sample, the probe was reflected back to the beam splitter to recombine with the reference pulses, which were reflected from an aluminum mirror positioned outside of the chamber. The first pair of probe pulses produce a interference pattern that was used to normalize the interference pattern produced by the second pair of the probe pulses that were temporally overlapped with the heating beam.

The two sets of probe and reference pulses, the signal and background, propagated through a pair of two slightly vertically misaligned polarized beam splitters (PBS) and were focused onto a spectrometer's (JY - Micro HR) input slit, resulting in two distinct interference images at the output of the spectrometer (Figure 4.12). The images were recorded with a scientific grade CCD (Finger Lakes CCD) cooled to 10 ^{o}C. Using two sets of probe and reference pulses allowed us to probe the frequency-dependent reflectivity before and with the pump beam heating the target. By comparing those two signals, the time-dependent reflectivity and phase shift of the probe could be extracted simultaneously.

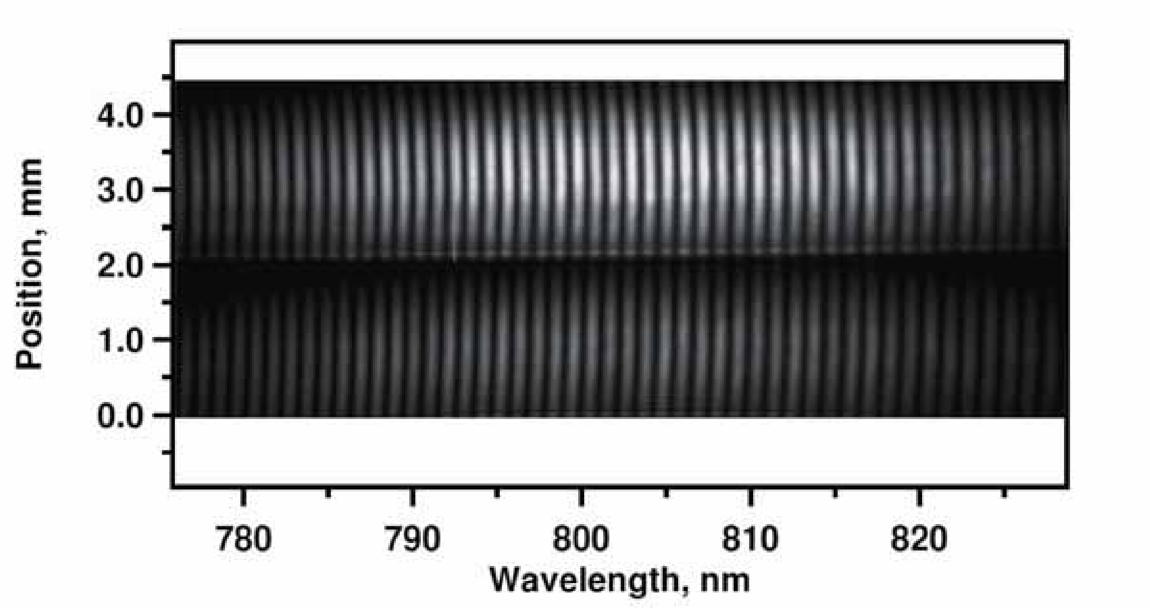

Figure 4.12 Example of the interference image recorder by the camera. Top stripe: The pump and the probe temporally overlap. Bottom stripe: The probe pulse is 120 ps before the pump.

To check the imaging of the back surface of the target, the beam splitter (BS3) was positioned before the spectrometer. Part of the probe beam was pointed to the camera and positioned at the same distance from the beam splitter as the spectrometer entrance slit. This allowed me to check for proper imaging of the target back surface.

For the experiments, a compact spectrometer was fitted with a 1200 groves/mm grating centered at 750 nm. The compact design of the spectrometer utilized a short focal length of only 140 nm. To be able to get the best magnification of the interaction region and at the same time try to fill the grating (f/3.88), the 11 mm diameter collimated probe reflected from the target was imaged with a 500 mm lens (L2) onto the entrance slit of the spectrometer. Since the probes were focused with a 200 mm lens onto the target, this produced only a x2.5 magnification of the interaction region. The 500 mm focusing lens also allowed the vertically misaligned signal and background pulses to pass through the entrance slit and for them to be collected by the camera without being clipped by the spectrometer and optics afterwards. Since the spectrometer input to output ratio was 1:1, we needed to improve the overall magnification of the system by installing a lens (L3) after the spectrometer exit (Figure 4.13). This produced a collimated ~2 mm beam, giving a final magnification of ~45. To see the interference fringes a cylindrical lens (CL) with the same focal lens as L3 was installed before the camera. The cylindrical lens was oriented horizontally to refocus interference fringes in the plane of the CCD camera.

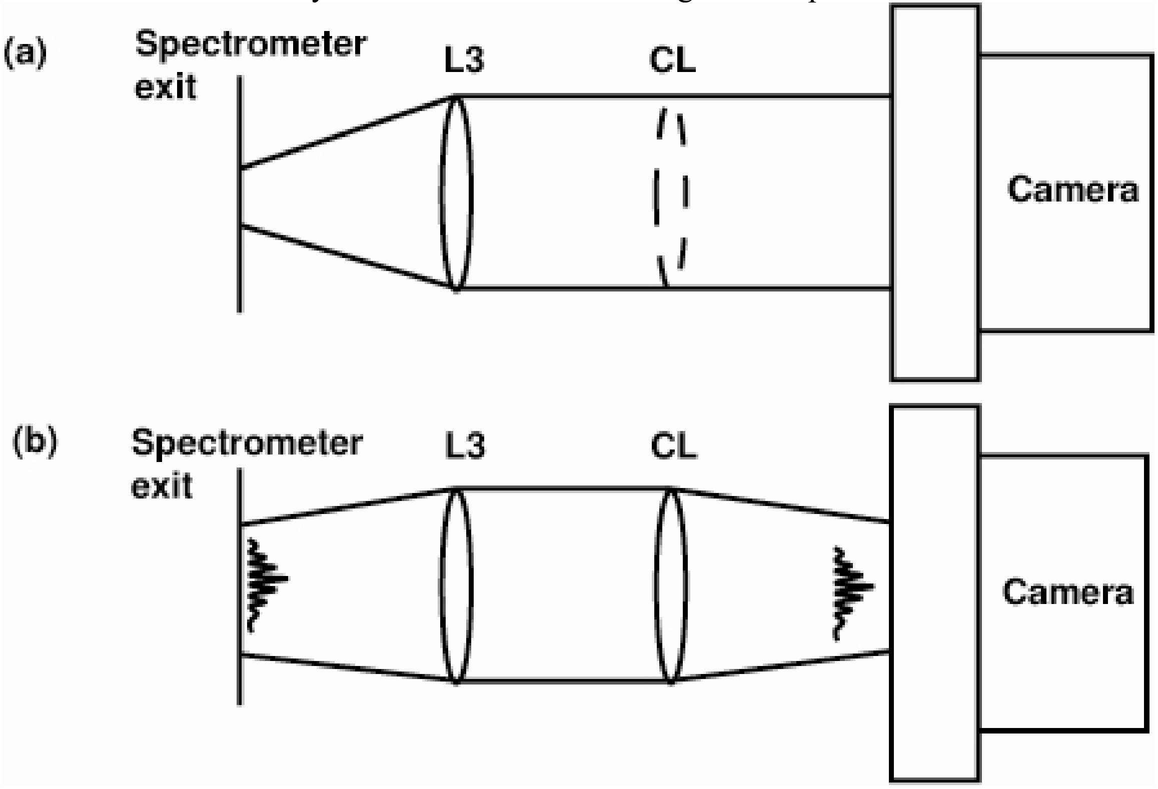

Figure 4.13 Schematics of the magnification system between the spectrometer exit and the camera.(a) Vertical view: the image at the output of the spectrometer is collimated by L3 to obtain the final magnification of 45 (b)Horizontal view: Cylindrical lens(CL) refocuses the fringes on the camera.

5 Single shot diagnostic

5.1 FDI PRINCIPLES

The goal of this experiment was to probe the plasma dynamics over tens of picoseconds with sub-picosecond resolution. In earlier works the time dependence was reconstructed by varying the time delay between the short probe pulse and the pump[18, 19]. Those approaches were sensitive to shot-to-shot variations in the laser pulse properties, and in the target response, as the probe was stepped through the delay range. In order to avoid those experimental uncertainties, we used frequency-domain interferometry (FDI) with the chirped pulses to measure ultrafast changes in optical properties over ~25 picosecond time-scales [67-71].

The FDI technique utilizes interference fringes in the frequency domain[28, 63, 72]. To get the fringes the two identical pulses are used. The electric field of the Gaussian reference pulse and the Δt delay probe pulse are :

$$\begin{aligned} E_{ref}(t) &= \exp(-at^2)\exp i(\omega_0 t + bt^2) \\ E_{probe}(t) &= E_{ref}(t+\Delta t) \end{aligned} \quad . \tag{5.1}$$

Computing the Fourier transform $E(\omega) = F[E_{ref}(t) + E_{probe}(t+\Delta t)]$ of the two pulses shows the interference spectrum:

$$\left|E(\omega)\right|^2 = E(\omega)E^*(\omega) = \left|\tilde{E}_{ref}(\omega) + \tilde{E}_{probe}(\omega)\right|^2 . \tag{5.2}$$

The interference spectrum exhibits modulations with a period of $\delta\omega = 2\pi/\Delta t$ (Figure 5.1).

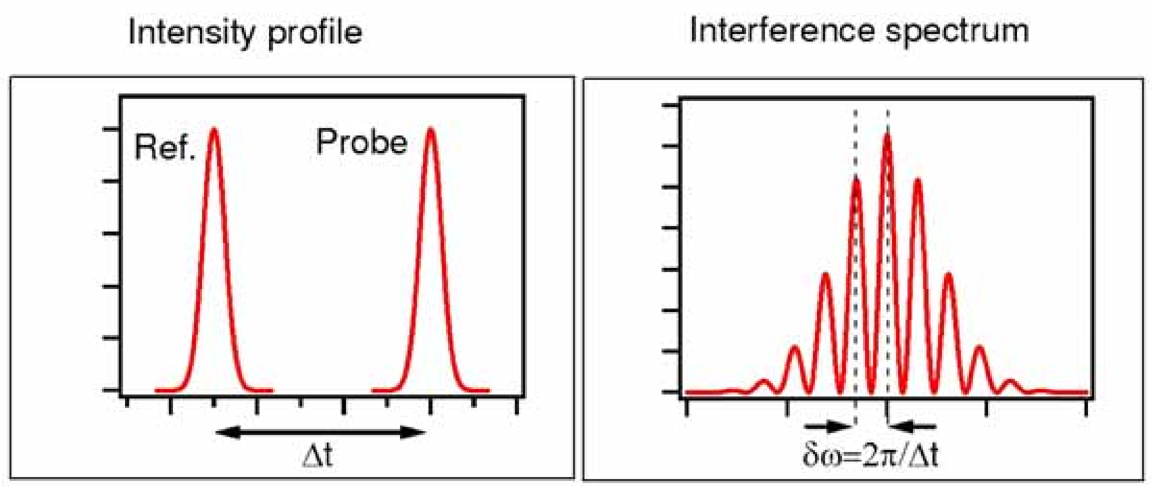

Figure 5.1 Intensity profile of two delayed Gaussian pulses and their interference spectrum.

The temporally delayed pulses interfere in the spectrometer due to the linear dispersion of the grating (Figure 5.2). As a consequence of the high spectral resolution in the spectrometer, the conjugate (temporal) information contained in the pulses becomes reduced to the point that previously separated pulses can overlap temporally.

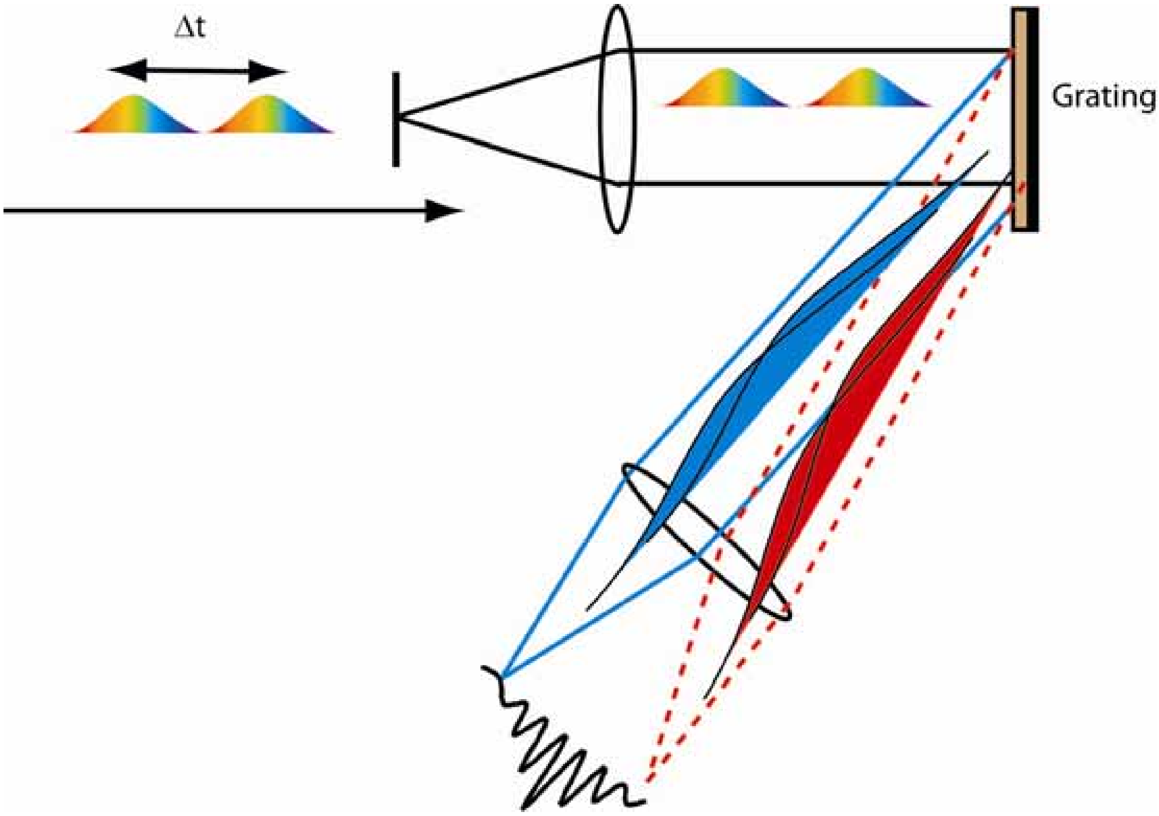

Figure 5.2 The schematics shows the reference and probe delayed by Δt. The high frequency resolution in the spectrometer forces the conjugate variable, the pulse duration, to increase. As a consequence, the resolved spectral components of the pulses interfere.

In the experiments, the first reference pulse and the time delayed probe pulse interact with the media before and after the pump pulse. Figure 5.3(a) shows the schematics of the pump-probe experiment where the FDI technique with the short pulses is implemented. Because the two pulses have a phase and intensity that depend on the optical properties of the reflected surface it is now possible to obtain changes in the optical properties of the reflecting surface from changes in the fringe contour [73]. Changing the time delay between the pump and probe pulses it is possible shot by shot to reconstruct the temporal reflectivity and phase shift changes of the reflected beam from the heated target.

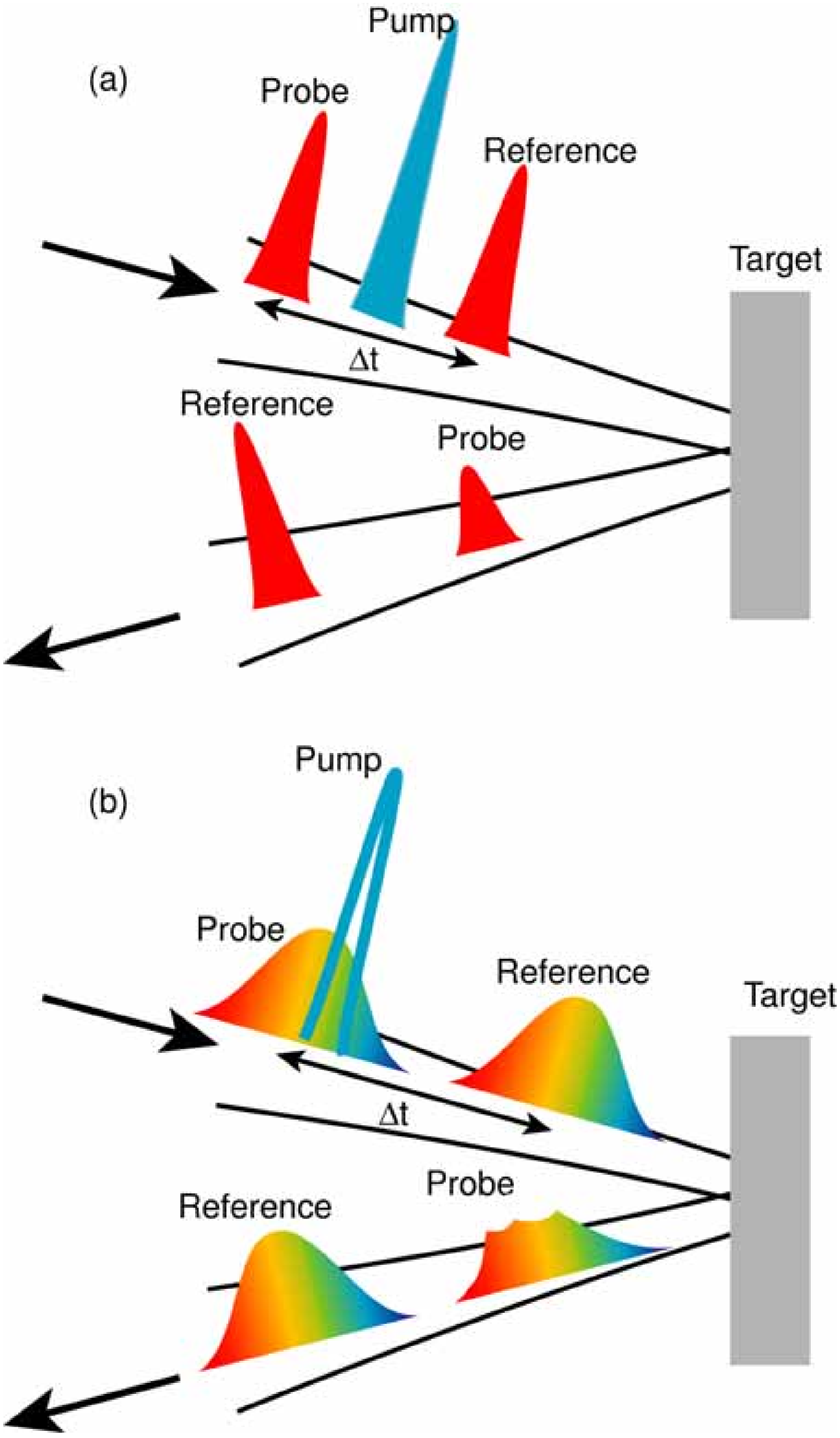

Figure 5.3 Pump-probe schematics using FDI technique as a diagnostic: (a) FDI with the short pulses, (b) FDI with the chirp pulses.

It is desirable to obtain measurement of the temporally changing optical parameters in a single shot in order to avoid shot to shot averaging and target surface variation. The FDI technique with the chirp pulses (Figure 5.3(b)) is designed to avoid this experimental uncertainty. In the FDI technique with the chirped pulses the probe and reference pulses are linearly chirped so that each time event in the plasma is projected onto a different frequency. The temporal variation of phase shift and reflectivity now can be obtained by direct mapping between the frequency and time[74]. The temporal observation window is determined from the probe pulse's duration and it is easily controlled by the distance between the compressor's gratings. It is important that the reference pulse will be reflected from the unperturbed target. However, too large of a separation Δt between the reference and probe causes the visibility of the fringes to become poor as the spectral modulation period change according to $\delta\omega = 2\pi / \Delta t$ or $\delta\lambda = -\lambda^2 /(c\Delta t)$.

From our spectrometer resolution of 0.2 nm, the maximum reference probe separation is 10 ps. In our measurements we use 28 ps probe pulses. To be able to reflect the reference from the unperturbed surface and have a good fringe visibility, the Michelson interferometer design was implemented (Figure 4.11). The reference and the probe pulses were split with the beam splitter at 45 degree. The reference pulse was reflected from the mirror outside of the interaction chamber and recombined with the probe pulse reflected from the back surface of the target. The reference beam was delayed from the probe beam by 3.3 ps.

5.2 UNWRAPPING PROCEDURE

In FDI, the reference pulse reflected from the unperturbed surface is $\widetilde{E}_0(t) = E_0(t)\exp(i\omega_0 t)$. The probe pulse is delayed by Δt. After reflecting from the plasma surface, the probe pulse undergoes a phase change $\Delta\Phi$ and its intensity is reduced by a factor $R(t)$. The field of the probe pulse can be written [63]:

$$E_1(t) = E_0(t-\Delta t)\sqrt{R}\exp(i[\omega_0(t-\Delta t)+\Delta\Phi(t-\Delta t)])\,. \qquad (5.3)$$

The Fourier transform of the two pulses together describes the spectral character of the signal:

$$F[E_1(t)+E_0(t)] = E(\omega-\omega_0)[1+\sqrt{r(\omega)}\exp\{-i[\omega\Delta t-\Delta\varphi(\omega)]\}\} \qquad (5.4)$$

In Eq.(5.4) the Fourier transform of the time-dependant reflectivity $R(t)$ is given by $r(\omega)=F[R(t)]$. Similarly, the Fourier transform of the time-dependant phase shift $\Delta\Phi$ is given as $\Delta\varphi = F[\Delta\Phi]$.

The power spectrum (or spectral intensity) of the signal is detected after the output of the spectrometer by the CCD camera. The spectral intensity of (5.4) is

$$\left|F[E_1(t)+E_0(t)]\right|^2 = \left|E(\omega-\omega_0)\right|^2[1+r(\omega)+2\sqrt{r(\omega)}\cos(\omega\Delta t+\Delta\varphi(\omega))]\,. \qquad (5.5)$$

The spectral phase difference between the probe and the reference is

$$\Delta\phi(\omega) = \phi_1(\omega)-\phi_0(\omega)\,. \qquad (5.6)$$

The temporal phase shift is determined by using the linear mapping between the frequency and time [74]:

$$\Delta\Phi(t(\omega)) = \Delta\phi(a(\omega-\omega_0))\,, \qquad (5.7),$$

where *a* is the linear chirp coefficient for a Gaussian pulse.

To extract the spectral phase shift and reflectivity changes from the experimentally obtained interferogram we used the Fourier transformed method developed by Takeda at *et al.* [73].

Following the notation of Takeda we rewrote Eq.(5.5) as

$$I(x) = a(x)+b(x)\cos(\omega_0 x+\phi(x))\,, \qquad (5.8)$$

where $a(x)$ represents the individual beam intensities combination and any non-uniform background illumination. The coefficint $b(x)$ was used to represent the envelope intensity. For the convenience of mathematical treatment we rewrote Eq.(5.8) as

$$I(x) = a(x) + c(x)\exp(i\omega_0 x) + c^*(x)\exp(-i\omega_0 x)\,, \tag{5.9}$$

where

$$c(x) = \frac{1}{2}b(x)\exp(i\phi(x))\,, \tag{5.10}$$

and $c^*(x)$ is a complex conjugate of $c(x)$.

The fringe pattern in Eq.(5.9) was then Fourier transformed with respect to x, giving

$$\tilde{I}(f) = \tilde{A}(f) + \tilde{C}(f - f_0) + \tilde{C}^*(f + f_0)\,, \tag{5.11}$$

where $\tilde{I}(f), \tilde{A}(f), \tilde{C}(f - f_0)$ and $\tilde{C}^*(f + f_0)$ are the Fourier spectra of $I(x), a(x)$ and $b(x)$ respectively, f is the spectral frequency in the x-direction. The spectra variation of $a(x), b(x)$ and $\phi(x)$ are slower compared with the spatial frequency f_0. With the use of a filter function only $\tilde{C}(f - f_0)$ spectrum was extracted from Eq.(5.11). Once extracted, it was translated by f_0 toward the origin to get $\tilde{C}(f)$. In this processes the unwanted background intensity profile $a(x)$ is filtered out. Using the inverse Fourier transform of $\tilde{C}(f)$, we obtained $c(x)$. To get $\phi(x)$ from the retrieved $c(x)$ we applied a complex logarithm to Eq.(5.10):

$$\ln[c(x)] = \ln[\frac{1}{2}b(x)] + i\phi(x)\,. \tag{5.12}$$

From the equation above the phase $\phi(x)$ and envelope intensity *b(x)* were obtained:

$$\phi(x) = \mathrm{Im}[\ln[c(x)]] = \tan^{-1}\frac{\mathrm{Im}[c(x)]}{\mathrm{Re}[c(x)]} \tag{5.13}$$

$$b(x) = 2|c(x)|\,, \tag{5.14}$$

where Re and Im represent the real and imaginary part of $c(x)$.

Figure 5.4 shows the result of this Fourier-transformed fringe analysis routine when applied to experimental data. Figure 5.4 (a) shows the interferometric fringes I(x) that were computed by averaging the 2D experimental interferogram. The Fourier transform of I(x) was computed with the FFT algorithm and the modulus of $\tilde{I}(f)$ was plotted in Figure 5.4 (b). $\tilde{I}(f)$ always has a central component $\tilde{A}(f)$ due to the pulse envelope and two spectra $\tilde{C}(f-f_0)$ and $\tilde{C}^*(f-f_0)$ at the carrier, or fringe, frequency. Only $\tilde{C}(f-f_0)$ was selected using a super-Gaussian filter and shifted by f_0 toward the origin to obtain $\tilde{C}(f)$. After applying the inverse Fourier transform to $\tilde{C}(f-f_0)$ we obtained $c(x)$. Figure 5.4 (c) shows the modulus of *b(x)* and the phase $\phi(x)$ computed from *c(x)* using Eq. and Eq.. In practice, the moduli *b(x)* and $\phi(x)$ are not absolute, and have systematic background signals superimposed on them. The extract the optical properties of the film, experimental values of *b(x)* and $\phi(x)$ were compared to a reference shot. Also, the extracted phase is determined only to within a factor of 2π. To correct for $|\Delta\phi(x)| \leq 2\pi$, a phase unwrapping subroutine was applied to avoid phase discontinuities.

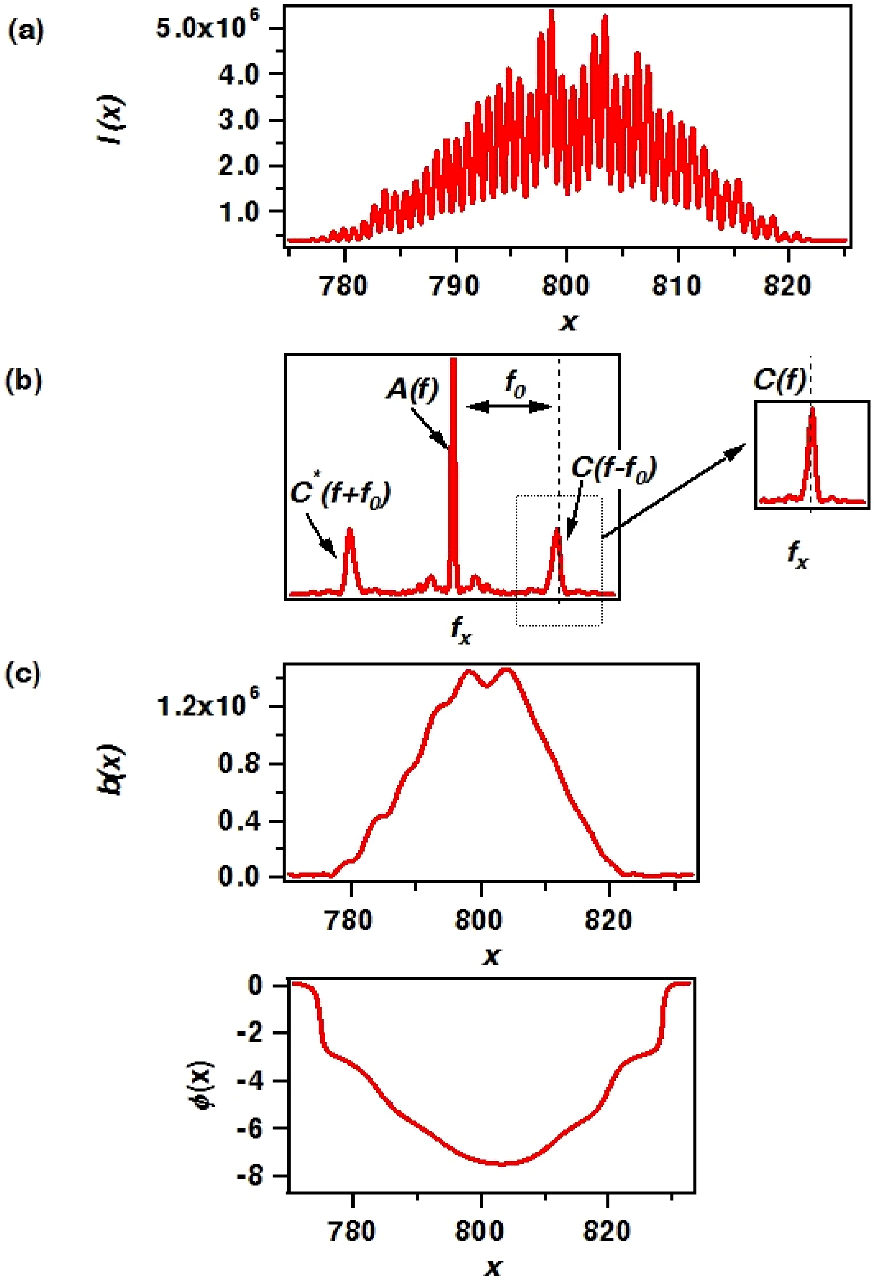

Figure 5.4 Fourier transform fringe analysis routine. (a) interferometric intensity profile. (b) Modulus of Fourier transform with a central component A(f) and two spectra C(f) and $C^*(f)$, separated by f_0 from the center component. (c) Modulus *b(x)* and phase *ϕ(x)* are obtain from the inverse Fourier transform *C(f)*.

5.3 CHIRP CHARACTERIZATION

To determine the temporal phase shift from the spectral phase shift, the linear chirp coefficient a from Eq.(5.7) must be measured. This was experimentally achieved by measuring the interference patterns of the reference pulse with the time-delayed 800 nm pump pulse. Figure 5.5 shows the schematics of the measurement, where the probe pulse was rejected in order to couple the pump beam to the interferometer. Figure 5.6 (a) shows the changes in interference patterns produced by interference of the pump and the reference pulse under the variation of pump-reference time delay τ. The wavelength shift of perturbed reference spectrum are plotted in Figure 5.6 (b) as a function of delay Δt. A linear least square fit of the data points that is co-plotted in Figure 5.6 (b) is used to extract the linear chirp coefficient a. The pulse length was estimated based on this measurement as well.

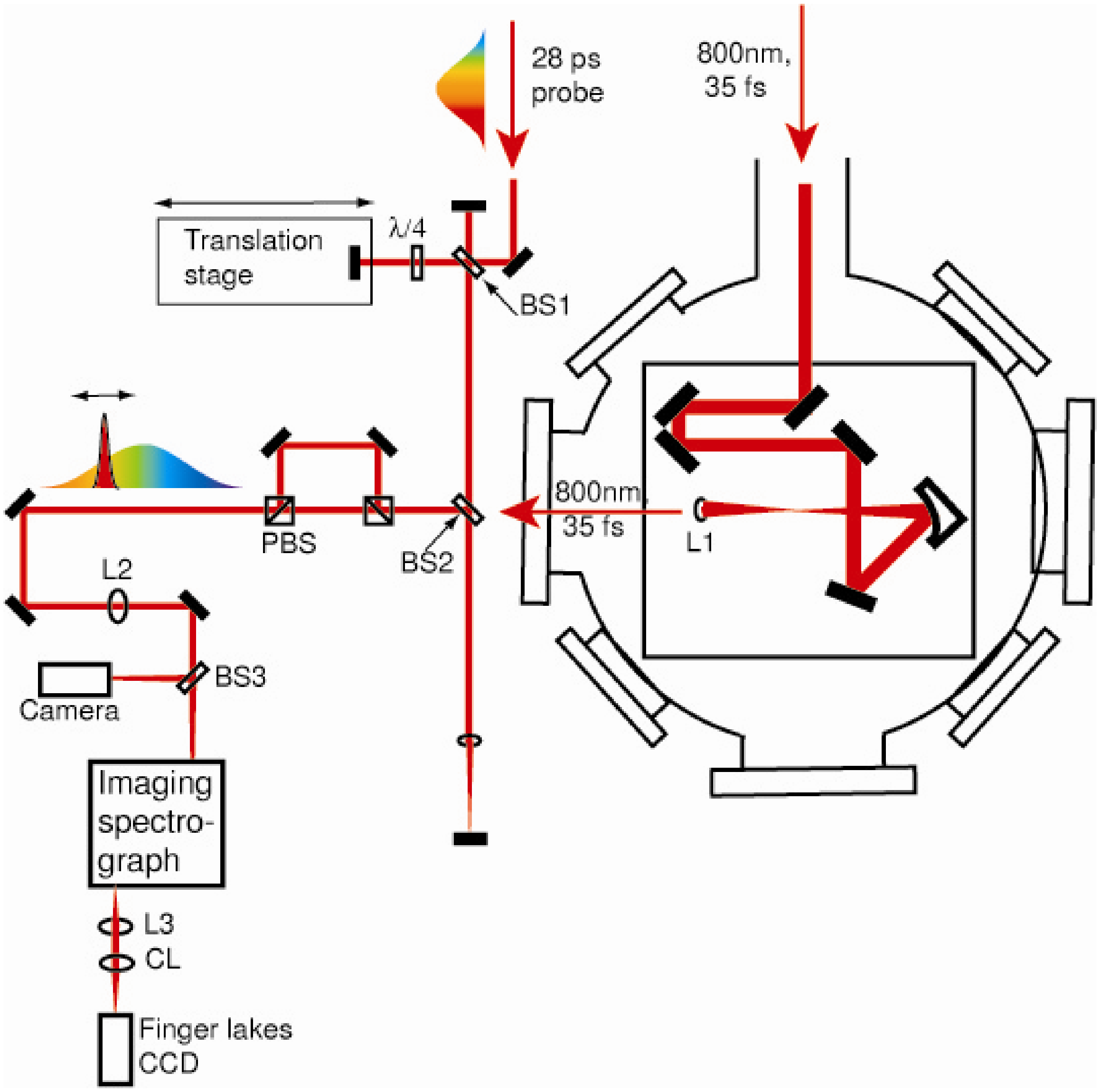

Figure 5.5 Schematics of the chirp pulse characterization, where 800 nm, compressed pump pulse was coupled to the interferometer. The time delay between pump and ps reference was adjusted with the translational stage

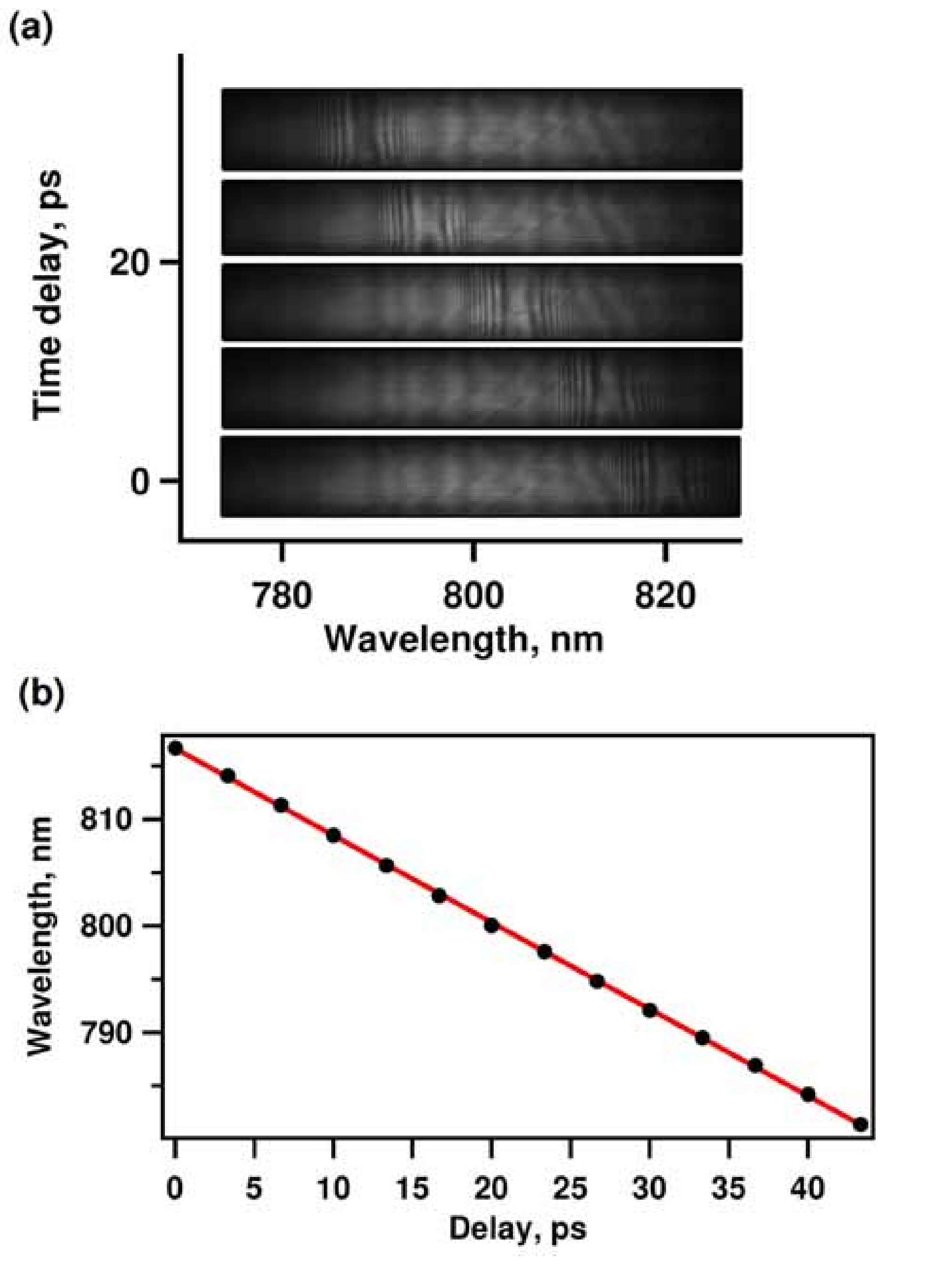

Figure 5.6 Determination of the chirp parameter of the 28 ps pulse. (a) Probe spectral intensity modulation as the pump-reference time delay changes.(b) Plot of the wavelength of the modulation peak (circles) vs. pump-reference delay with a liner least squares fit(line).

5.4 SIMULTANEOUS MEASUREMENT OF TWO PARAMETERS, RESOLUTION

In each shot there were two sets of probe and referenced pulses that were used to measure the back surface reflectivity and phase shift simultaneously. The interference signal from first set of probe and reference pulses delay by 120 ps from the second set was used as the background. The second interference signal modified by the presence of the laser produced plasma was taken as the background+signal. Ideally, the signal could be backed-out by comparing the two results. In practice, a second shot (calibration shot) was taken just before every data shot. In that case, all experimental parameters were the same except that the measurement was performed with the pump blocked. The additional shot was necessary in order to account for the phase accumulated through the different optical paths between two sets of probe-reference pulses. It was also necessary to repeat the additional shot for each target, because every target had a unique background response.

The changes in phase shift due to the laser heating of the target were calculated by taking the difference between the spectral phase of the probe ϕ_{pr} and the reference ϕ_{ref} signals and correcting it by extracted phase differences from the calibration shot $(\phi_{pr}^{C} - \phi_{ref}^{C})$.

$$\Delta\phi(\omega) = \phi_{pr}(\omega) - \phi_{ref}(\omega) - (\phi_{pr}^{C}(\omega) - \phi_{ref}^{C}(\omega)) \tag{5.15}$$

The change in the reflectivity due to the laser heating of the target was calculated by squaring the ratio between the envelope intensities of the probe $b_{pr}(\omega)$ and reference $b_{ref}(\omega)$ signals normalized to the probe-signal ratio from the calibration shot.

$$r(\omega) = \left(\frac{b_{pr}(\omega)/b_{ref}(\omega)}{b_{pr}^{C}(\omega)/b_{ref}^{C}(\omega)} \right)^{2} \tag{5.16}$$

Using the extracted linear chirp coefficient the spectral phase and reflectivity changes were converted to temporal phase $\Delta\Phi(t)$ and reflectivity *R(t).*

Signal-to-noise ratio of the camera defined the measurement sensitivity. The phase noise does not depend on the number of fringes [63]. At the same time the presence of any non-uniform background illumination had a negative impact on the measurement resolution. The measurement accuracy was also affected to the misalignment and clipping of the beams. From the calibration shot we determine the standard deviation $\sigma(\Phi(0))$ of the measured phase $\Phi(0)$ and reflectivity R(0) from the cold target. Taking into account that $\Delta\Phi$ and R are changing during the duration of the probe pulse, the measurement gave the temporal average of the parameters weighted by the amplitude of the reflected pulse from the plasma. The final phase and reflectivity fluctuations were

$$\sigma(\Phi(t)) = \frac{\sqrt{2}}{\sqrt{R(t)}}\sigma(\Phi(0)) \qquad (5.17)$$

$$\sigma(R(t)) = \frac{\sqrt{2}}{\sqrt{R(t)}}\sigma(R(0)) \qquad (5.18)$$

The $\sqrt{2}$ in the final formulas is due to the requirement of the calibration shot. In our measurement we were able to obtain $\sigma(\Phi(0)) = 0.007 rad$ and $\sigma(R(0)) = 0.03$. In practice, other sources of noise did exist. For instance, imperfect filtering of the frequency data was observed as small oscillations in the FFT output.

Temporal resolution of the measurement was affected by the chirp of the probe pulses, spectrometer resolution and the accuracy of the chirp characterization and zero time finding. The measured linear chirp coefficient $a = (4.2 \pm .3) * 10^5 fs^2$ indicated that the chirp was very small ($2a << \Delta\omega^{-2}$) and the time resolution was determined by the fundamental limit of transform limited pulse. With the laser bandwidth of 26 nm it gave a temporal resolution of 13 fs. In the measurement the time resolution that could be obtained was limited by the spectrometer's resolution. The spectrometer's resolution with the 13um/pix camera was 0.2 nm. As a consequence, the temporal resolution of the detector was only 220 fs. Taking into account the duration of the compressed pulse and the accuracy of finding the zero time delay, the final time resolution of the measurement was 350 fs.

6 Experimental results

6.1 PRIMARY RESULTS: REFLECTIVITY MEASUREMENT

In the first series of measurements, the back surface reflectivity of a 40 nm aluminum film supported by a formvar/carbon layer was measured using the pump-probe experimental setup with short (60 fs, 400 nm) probe pulses and short (50 fs, 800 nm) pump pulses with $5*10^{13}$W/cm^2 intensity. The experimental results are shown in Figure 6.1. The reflectivity was measured as a function of the time delay between the heating and the probe beams and in the experiments, and data were collected at time delays up to 30 ps. At every time step 5-10 shots were taken to improve statistics. The amount of shots that were available for each target set restricted the amount of time steps and shots per data point I was able to do. Every shot was normalized to the cold target reflectivity measurement that was taking before every shot by blocking the heating beam. Using this technique I was able to measure the reflectivity changes to within 6 %.

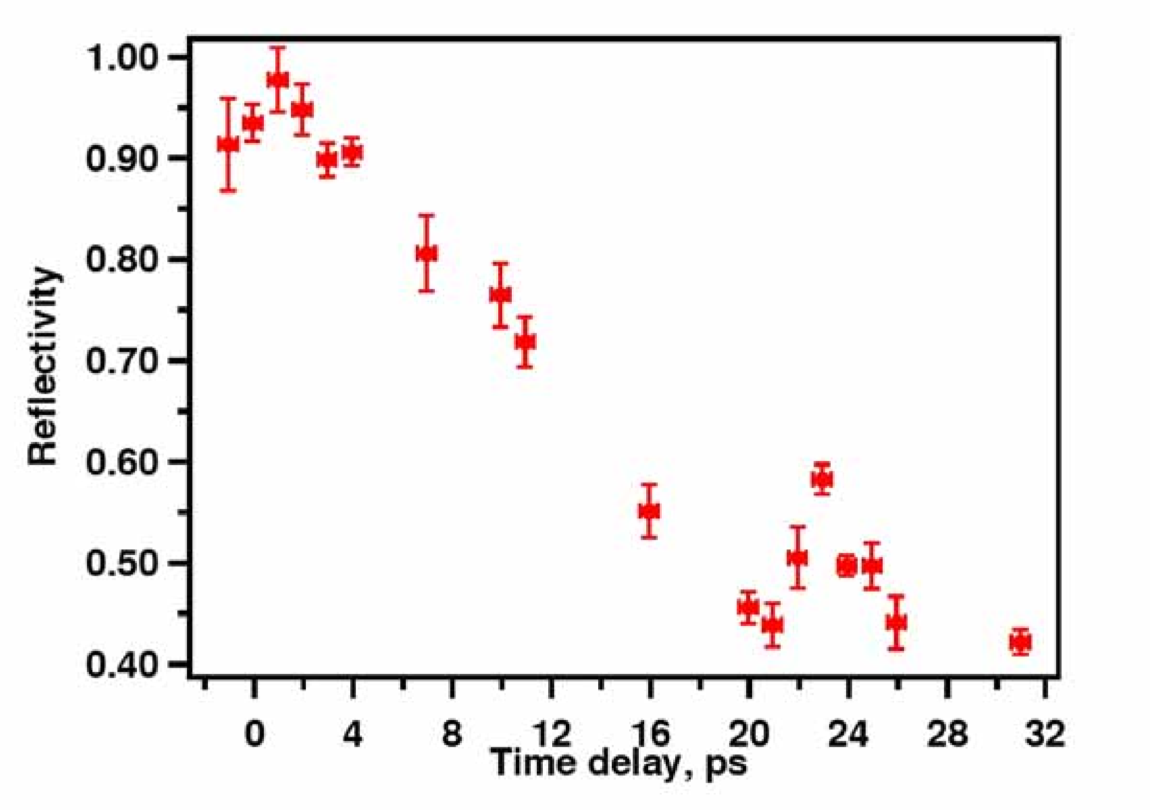

Figure 6.1 Time dependent reflectivity changes of the 400nm reflected probe from back surface of 40nm aluminum foil supported by a plastic layer. The target was heated with $5*10^{13}$W/cm^2.

The data show that as early as 3 ps after laser heating, reflectivity at the back surface of the target began to drop (Figure 6.1). It indicated that the heat wave had reached the back surface of the target, bringing an increase in electron temperature and a decrease in electrical conductivity. At the time of 15 ps, reflectivity changes were irreversible and had dropped by 50%, indicating that the target was expanding. An increase in reflectivity near 23 ps was also observed, however the feature is believed to have been caused by leakage of the 800 nm pump beam to the photodiode. The third order autocorrelation measurement resolved an intense post pulse with the pulse to post-pulse contrast ratio of 10^3 at 24 ps.

The presence of the supporting layer complicates the analysis of laser-matter interaction. At room temperature the formvar/carbon supporting layer is transparent. As the temperature in the layer increased the absorption increased and the film became highly conductive [75]. Assuming that the laser energy was mostly absorbed in the aluminum layer, the dielectric function was calculated using the Drude model. The temperature dependent conductivity and electron temperature were extracted from the hydrocode output. The details of the calculation are described in paragraph 6.6. The calculated time dependent reflectivity of heated aluminum film is shown in Figure 6.2. As it seen from the result of simulation the thermal wave reach the back surface of the film immediately after the laser irradiation and the film expands within 1 ps. The time scales obtained in the simulation are drastically different from the measurement. It suggests that the absorption in the support formvar/carbon layer should be considered. The presence of the absorbing supporting layer did not allow me to get any conclusive results about the dynamics of the thermal wave in aluminum.

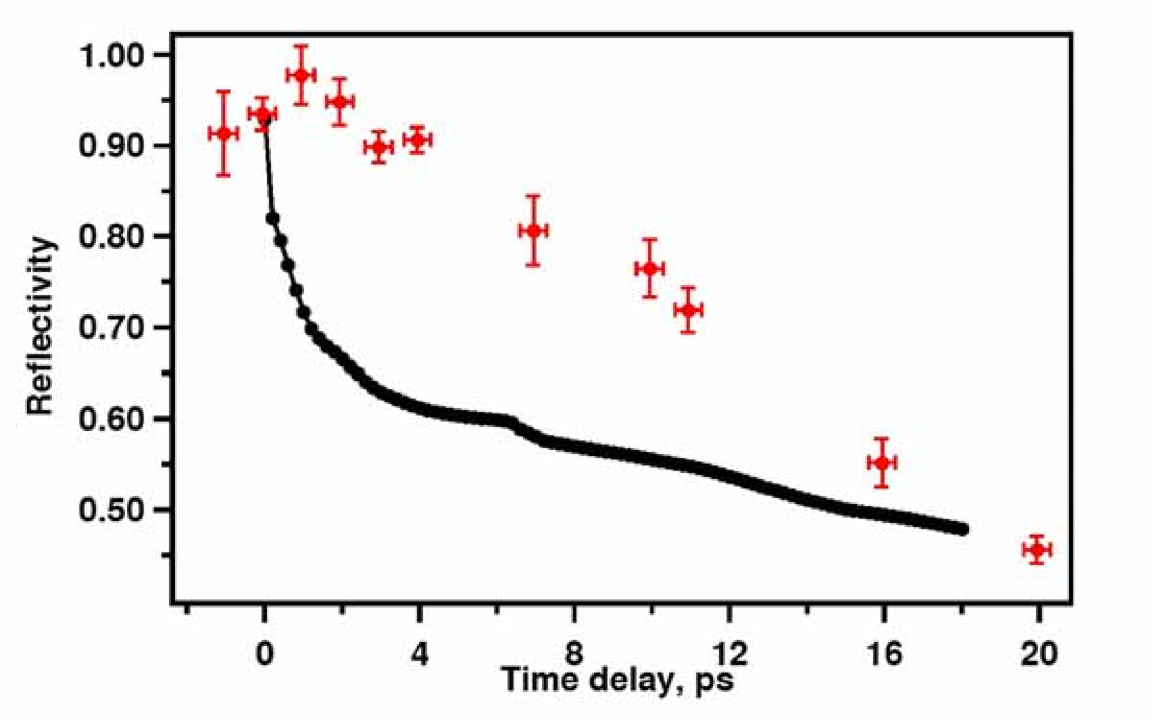

Figure 6.2 Calculated (line) time dependent reflectivity changes are compared to the experimental results (circles).

A number of improvements were needed following this initial reflectivity experiment. It was desirable to do the experiment in a single shot because differences in each target, including mechanical alignment error, introduced unwanted uncertainties. Furthermore, the number of targets available for each run restricted the amount of the time step taken during the run and the statistics improvement. We wanted to obtain continuous measurement restricted just by the time resolution of the experiment, rather than the resolution of a mechanical stepper in a delay line. It was also desirable to improve the target design. Having free standing metal film eliminates concerns about the absorption in the supporting layer and makes it possible to study the electron conduction mechanism in a purely laser-heated aluminum film. The intensity of the heating beam had to be kept below 10^{14} W/cm^2 in this experiment to avoid any target modification by the pre-pulses before the heating pulse arrival. Doubling the fundamental pulse improved the pulse to pre-pulse contrast ratio to 10^8 and also allowed for the intensity to be increased. Finally, the first experiment was designed to measure only one optical parameter, reflectivity of the back service. It has been suggested [24] that measurement of the phase shift of the reflected probe together with the reflectivity will be a more sensitive test of the electron thermal conduction in a plasma and it would allow us to asses the dielectric function, as well as the electrical conductivity of the plasma.

6.2 PUMP-PROBE OF FREE STANDING FOIL

Experimental studies of transient effects in laser irradiated aluminum thin film were carried out using the single-shot interferometry diagnostic. The experiments were done with 170, 230 and 375 nm free standing aluminum films. The targets were irradiated with a pump intensity of 1-5*10^{14} W/cm^2 in order to exclude radiation losses from laser heated plasma and radiation transport in the foil[40]. Consequently, the main transport mechanism in the heated targets was collisional-electron transport. This moderate intensity also minimized the vacuum heating effect [17, 58] (that is further neglected due to the normal incidence on the target of the heating beam) and eliminated the need to consider the anomalous skin effect [76], caused by laser energy absorption when the electron mean free path is shorter than the plasma scale length or density gradient.

Each analyzed data set of back surface reflectivity (Figure 6.3). and phase shift (Figure 6.4) change were chosen out of about 5 data sets taken at pump intensities similar to within 12% To eliminate noise not removed by filtering, the optical parameters were temporally averaged, leaving a final temporal resolution of 0.35 ps. (Figure 6.5)

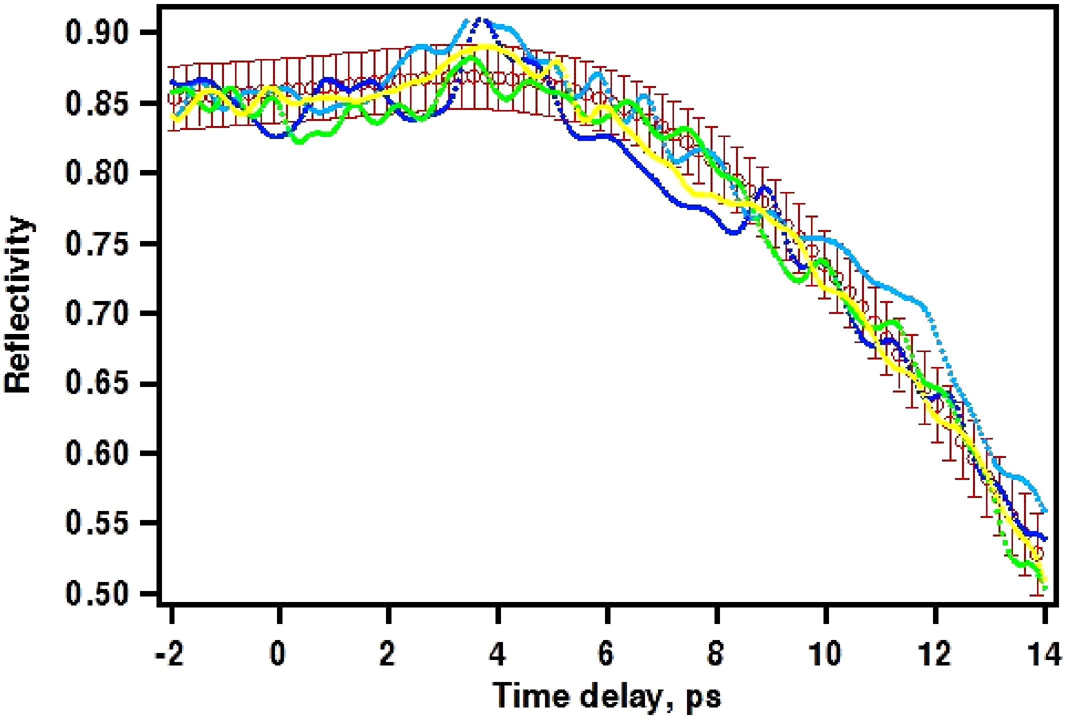

Figure 6.3 Time dependences of the back surface reflectivity changes from 170 nm thick laser-heated aluminum targets. The best shot (green curve) was chosen out of 4 shots (dots) taken at (2.4±0.2)*10^{14}W/cm^2 intensity and was temporally averaged (circles with the error bars).

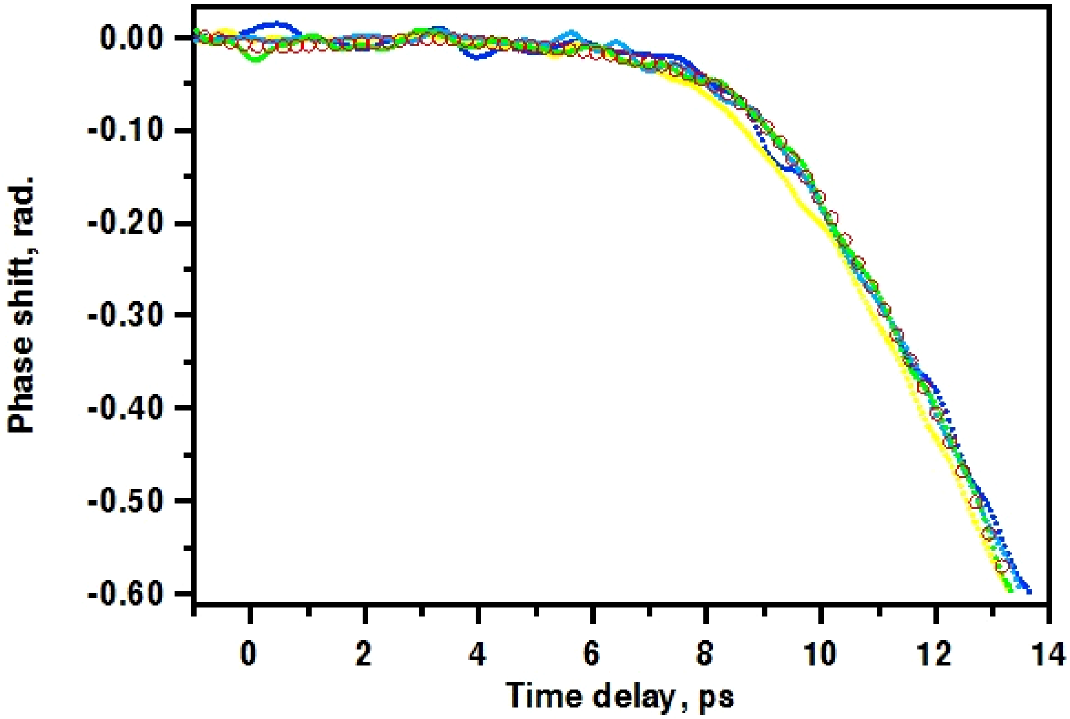

Figure 6.4 Time dependences of the back surface phase shift changes from 170 nm thick laser-heated aluminum targets. The best shot was chosen out of 4 shot (dots) taken at $(2.4 \pm 0.2)*10^{14}$W/cm^2 intensity and was temporally averaged (circles with the error bars).

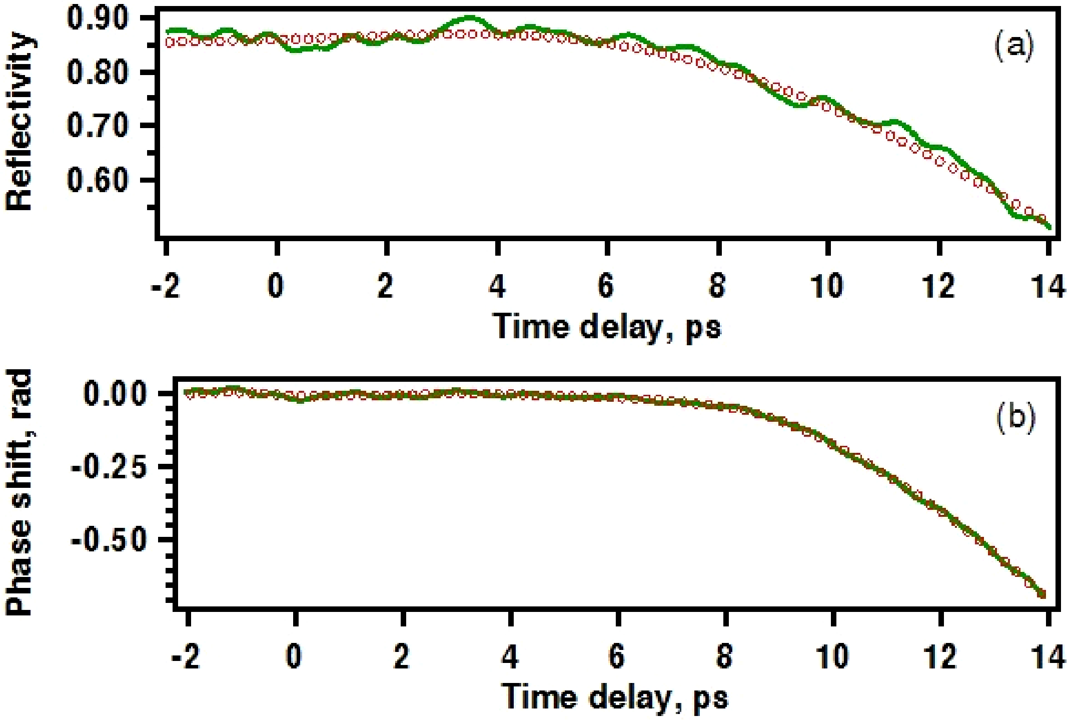

Figure 6.5 Time dependences of the back surface reflectivity (a) and phase shift (b) changes from 170 nm thick laser-heated aluminum targets. The best shot (see Figure 6.3, Figure 6.4) was temporally averaged leaving the final resolution of 350 fs.

6.3 DYNAMICS VS INITIAL ENERGY DEPOSITION

The summary of taken data for different film thickness heated within intensity range of 10^{14} W/cm^2 is shown in Figure 6.6, Figure 6.7, and Figure 6.8. Depending on the film thickness and laser irradiation intensity the time scales of plasma dynamical changes vary. Three stages of solid plasma development were observed. For the first few picoseconds after the laser irradiated the front surface of the target the signal of the probe at the back surface was unchanged. Later in time the heat front arrived at the back surface of the target due to electron conductive heating. The higher back surface electron temperature decreased the conductivity and created a greater skin depth for the probe. As a result of lower conductivity, the reflectivity dropped and changes in the optical path

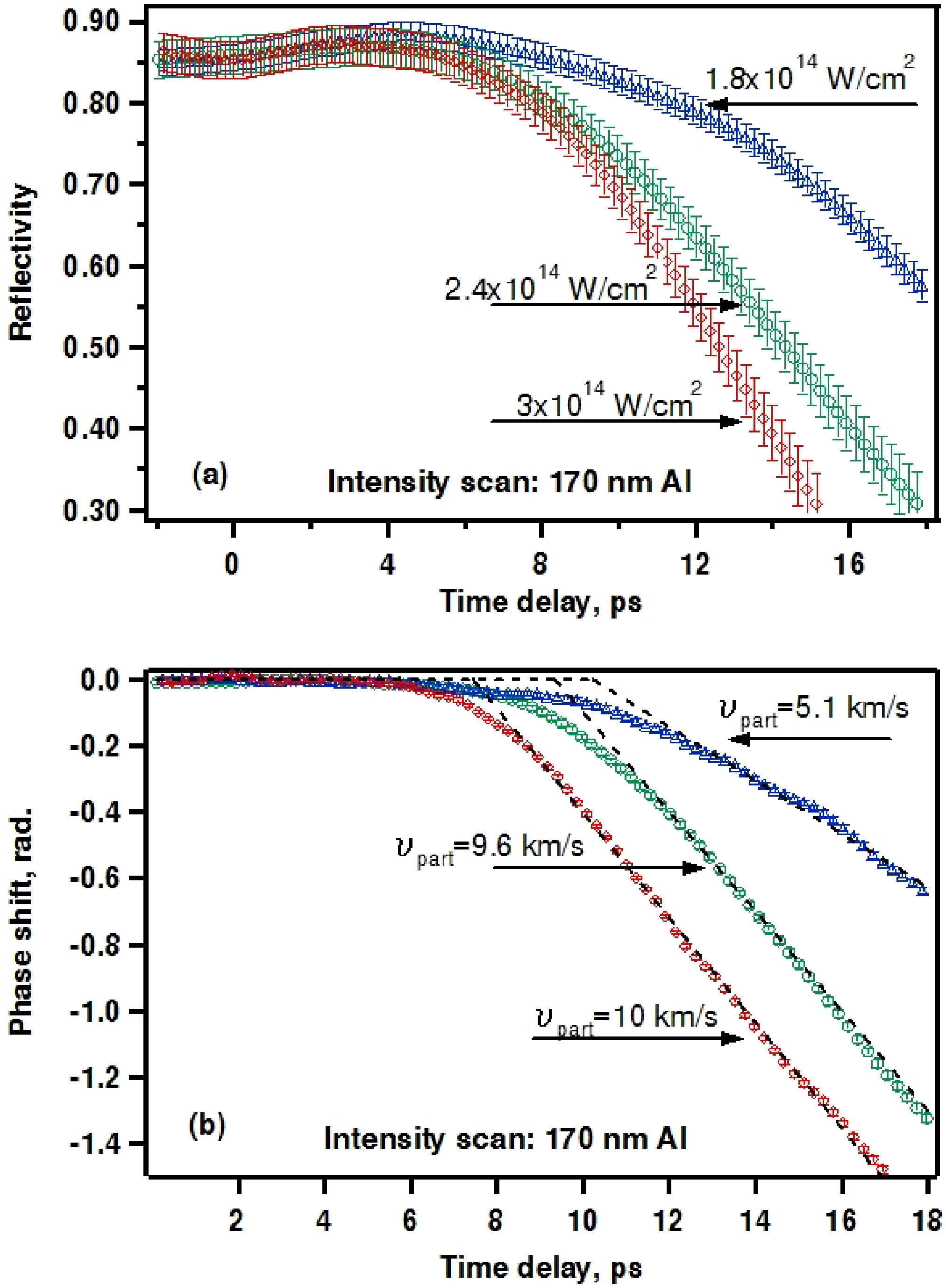

Figure 6.6 Time dependences of the back surface reflectivity(a) and phase shift (b) changes from 170 nm thick laser-heated aluminum targets at $3*10^{14}$W/cm^2(rhombs), $2.4*10^{14}$W/cm^2(circles) and $1.8*10^{14}$W/cm^2(triangles) intensities.

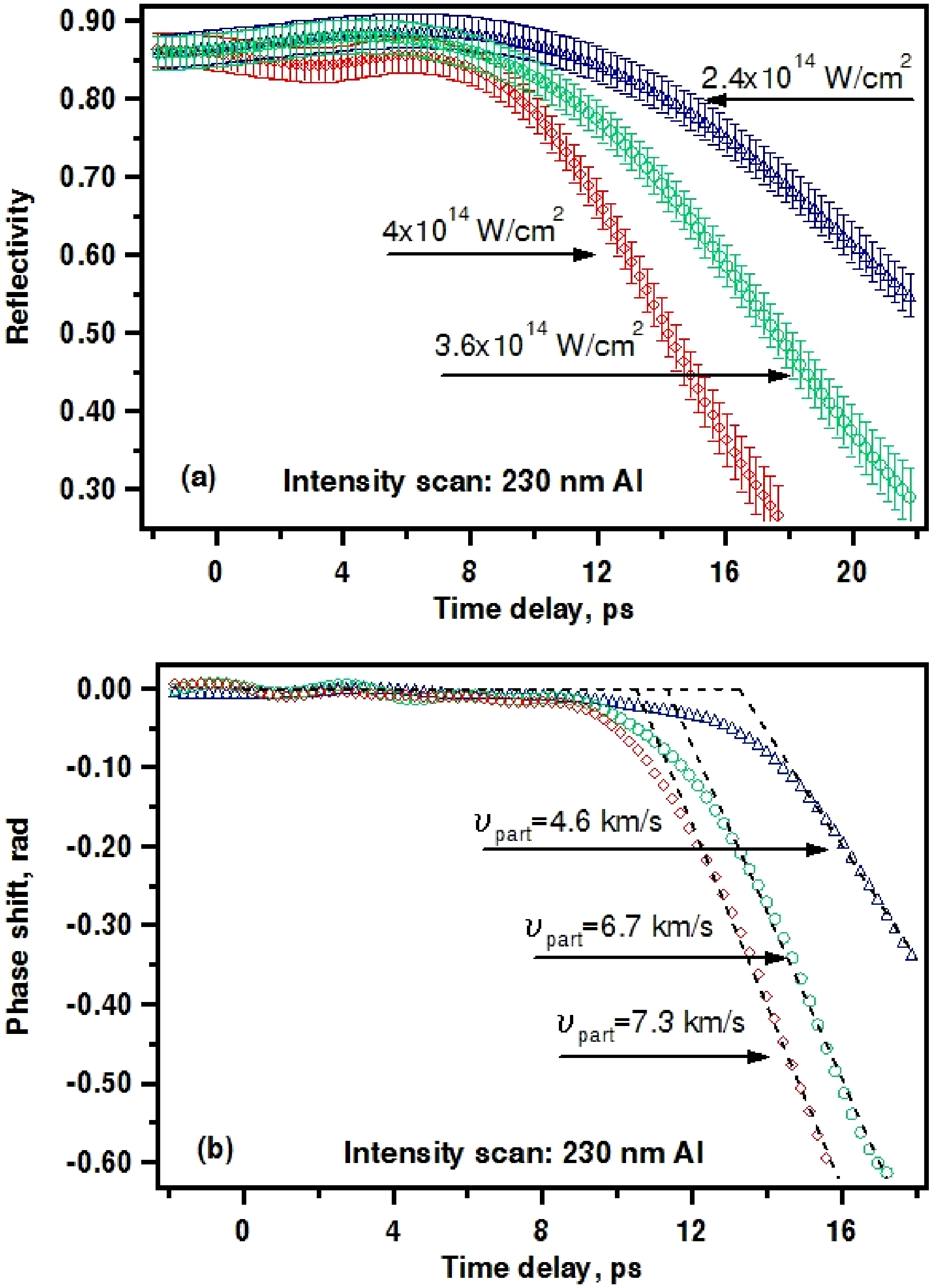

Figure 6.7 Time dependences of the back surface reflectivity(a) and phase shift (b) changes from 230 nm thick laser-heated aluminum targets at 4*10^{14}W/cm^2(rhombs), 3.6*10^{14}W/cm^2(circles) and 2.4*10^{14}W/cm^2(triangles) intensities.

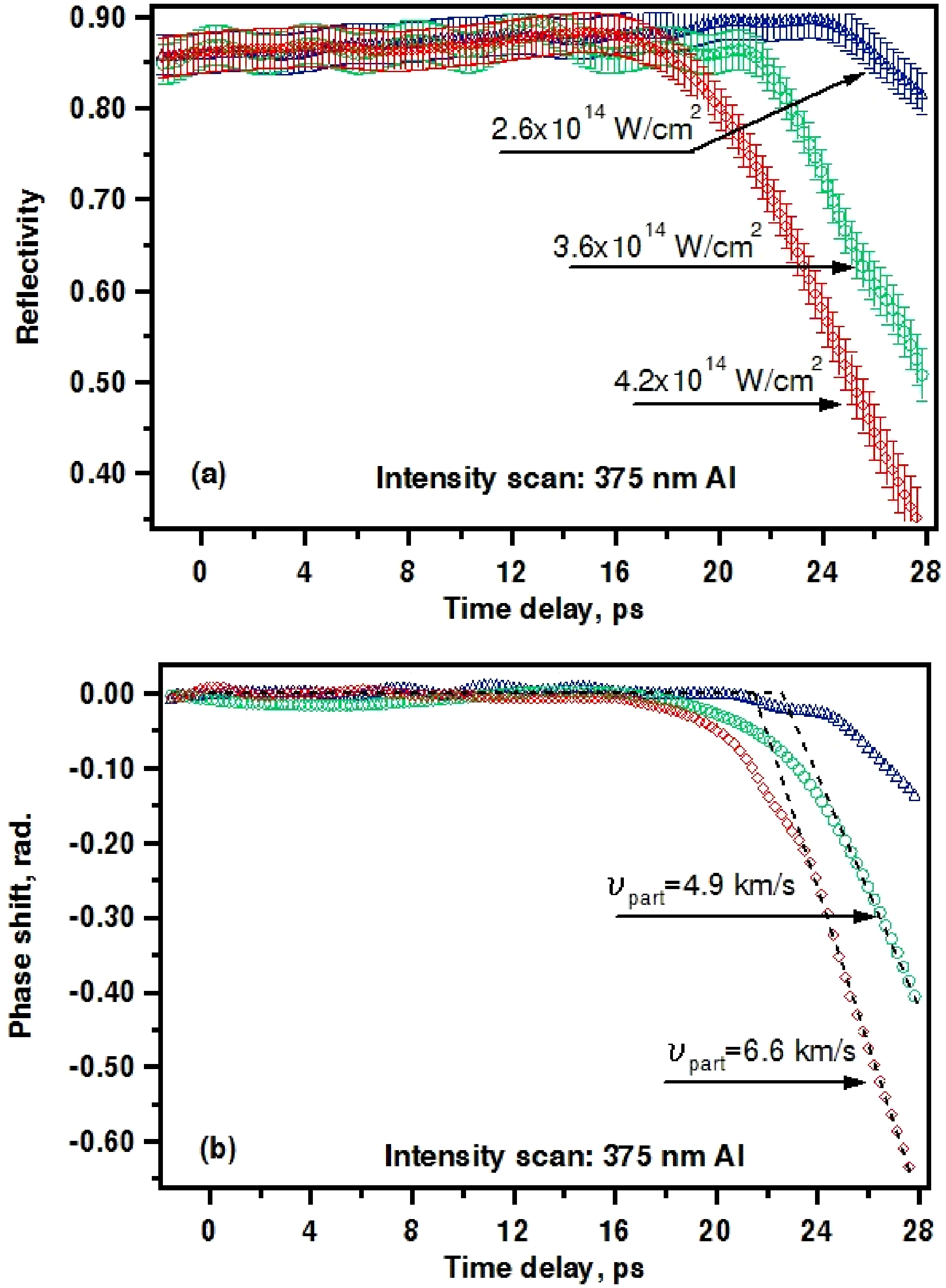

Figure 6.8 Time dependences of the back surface reflectivity(a) and phase shift (b) changes from 375 nm thick laser-heated aluminum targets at $4.2*10^{14}$W/cm^2(rhombs), $3.6*10^{14}$W/cm^2(circles) and $2.6*10^{14}$W/cm^2(triangles) intensities.

caused the measured phase to change. At the final stage the shock front reached the back surface. The shock wave produced the highest density compression of material that was then followed by a release wave. Following that the phase shift was dominated by the particle motion, and it decreased rapidly as material expanded.

To emphasize the final stage of the evolution of the heated foil, lines were fitted to the phase data for points following the arrival of the heat wave. The slope of the line was proportional to the free surface velocity, which was twice the particle velocity. The extracted particle velocity for the 170 nm film at $2.4*10^{14}$ W/cm^2 film was higher than the particle velocity extracted in earlier reports [49] of an aluminum film irradiated at the same intensity. The higher value obtained in our experiment is explained by the smaller thickness of the target and the fact that the shock decays as the pressure wave propagates. The fitted line shows a clear distinction between the stage when changes are dominated by the particle motion and the stage when the changes are defined by the temperature increase due to the electron thermal conduction. The shock precursor, or decrease in the phase shift prior to shock breakout, was different from the precursor observed in shocked aluminum films supported by thick cover glass [25]. The oppositely signed precursor, observed by Gahagan *at al* before the shock breakout in aluminum film supported by the thick cover glass, was attributed to the pressure dependent 1.5 eV interband transition in aluminum at 800 nm which is known to shift to higher frequency with pressure[77]. The absence of an oppositely signed precursor in our measurement was attributed to a difference between shocked metal film by laser driven pressure pulses and heated metal film by depositing the laser energy directly in the film, as been demonstrated in this thesis.

6.4 TIME DEPENDENCE OF HEAT FRONT PROPAGATION

Figure 6.9 shows the data for different film thicknesses heated with the same intensity. The thicker the target, the later the optical parameters start to change. The thickness of the target is plotted versus the heat front arrival time in Figure 6.10, assuming that the time when the optical parameters start to change corresponds to the time of the heat front arrival at the back surface. The time dependence of the heat front propagation in a target is nonlinear. The fitted power curve, $x_{front} = At^{B}$ to the plot results in a $t^{4/7}$ time dependence. This is much faster than the power laws obtained for electron thermal front propagation in an ideal plasma , where the formula for the heat front propagation derived in [40] was:

$$x_{front} = \xi_0 \left(\frac{8}{3m_e^{1/2}(Z+1)e^4 n_e^{7/2} \ln \Lambda} \right)^{2/9} F_{abs}^{5/9} t^{2/9} \qquad (6.1)$$

F_{abs} is absorbed laser energy fluence at the surface on the surface of the target. The Spitzer conductivity was assumed in the derivation. The fast heat transport obtain in this thesis is due to the fact that the Spitzer conductivity gives values that are factor of 100 smaller than expected for a lower temperature (<100eV) plasma.

It is possible to evaluate the temperature dependence of heat diffusivity using the heat front propagation power law. The one dimensional heat conduction equation is:

$$\frac{\partial T}{\partial x} = \frac{\partial}{\partial x} \chi \frac{\partial T}{\partial x} \qquad (6.2)$$

The spatial temperature distribution satisfies the condition of energy conservation:

$$\int_{-\infty}^{+\infty} T dx = Q \qquad (6.3)$$

The quantity Q is equal to $E/\rho c_p$, where E is the energy release at initial time per unit area, c_p is a specific heat of electrons defined at constant pressure, and ρ is a mass density. The parameter Q is in deg*cm.

The heat diffusivity can be generalized to following form:

$$\chi = aT^n \tag{6.4}$$

Where a is a numerical parameter in cm^2/s*deg^n. The parameters Q and a can be combined in a single dimensional combination containing only the units of length and time, aQ^n in cm^{n+2}/s. From dimensional consideration the law for the heat front propagation is:

$$x_{front} \sim (aQ^n t)^{1/n+2} = (aQ^n)^{1/n+2} t^{1/n+2} \tag{6.5}$$

The power law for the heat front propagation obtained in our measurement is $t^{4/7}$. From this power law, n equals to -¼. The temperature dependent electrical conductivity σ, can be obtained from thermal conductivity κ, using the Weidemann-Franz relation:

$$\sigma \sim \frac{\kappa}{T} \sim \frac{\chi}{T} = \frac{aT^{-1/4}}{T} = \frac{a}{T^{5/4}} \tag{6.6}$$

This power law shows that conductivity decreases as temperature increases. The front surface temperature immediately after the laser absorption was ~20 eV. Thermal diffusion transfers the heat into the surrounding material, resulting in temperature increase at the back surface of the target. The back surface sees temperature increase from room temperature to few hundreds of meV, depending on a target thickness. In this temperature range solid heating by electron thermal transport is governed by the solid state thermal conductivity of aluminum which is constant. The electrical conductivity in this temperature range can be approximated as *~1/T*. The obtained power law for the electrical conductivity in our experiment (Equation(6.6)) is different from the solid state one. However, the sample temperature dependence was consistence with that of a solid state material, both showed a decrease in electrical conductivity as the temperature increased.

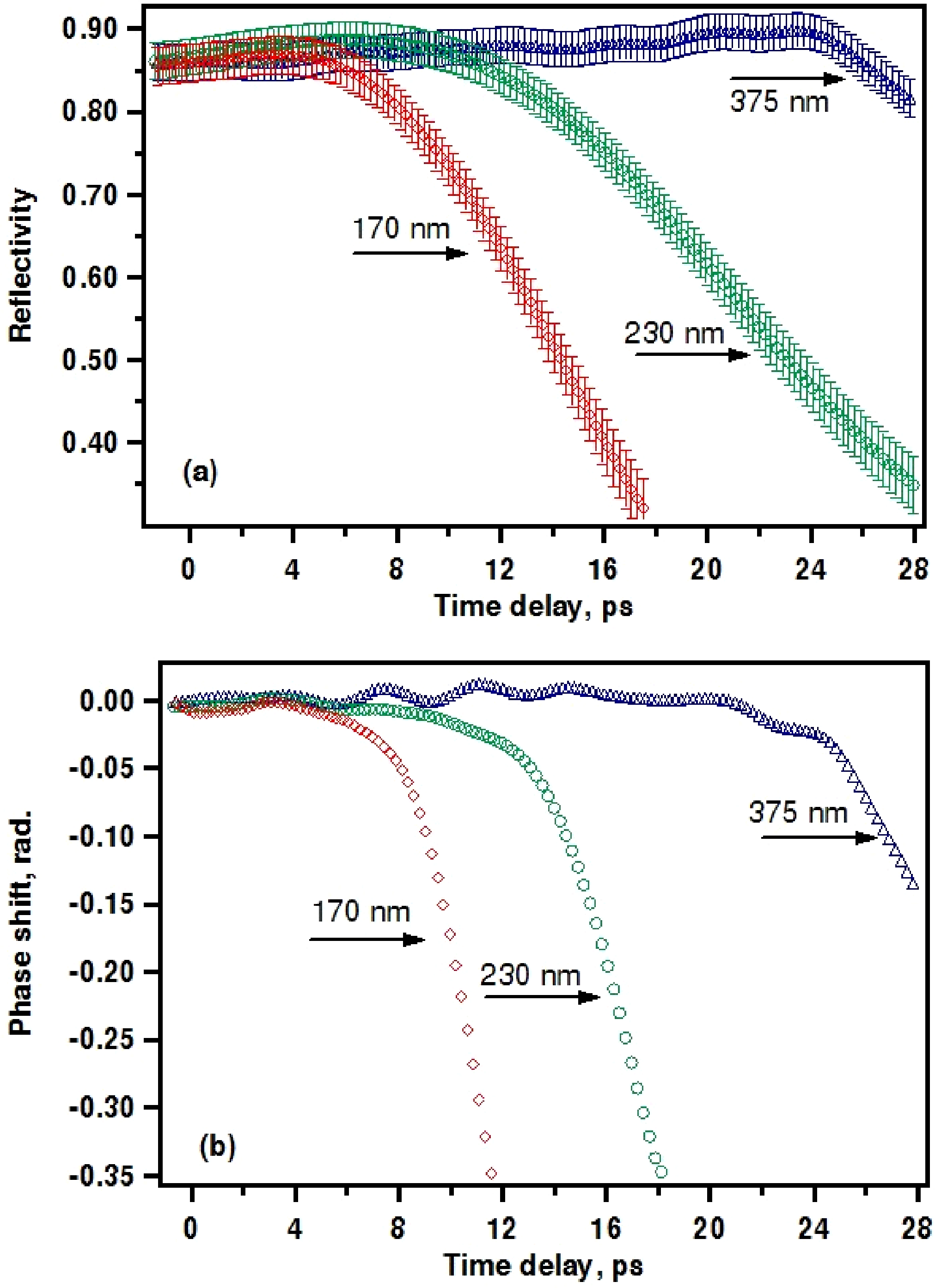

Figure 6.9 Time dependences of the back surface reflectivity(a) and phase shift (b) changes from 170nm (rhombs), 230nm (circles) and 375nm (triangles) thick laser-heated aluminum targets at (2.4±0.2)*10^{14}W/cm^2 intensity.

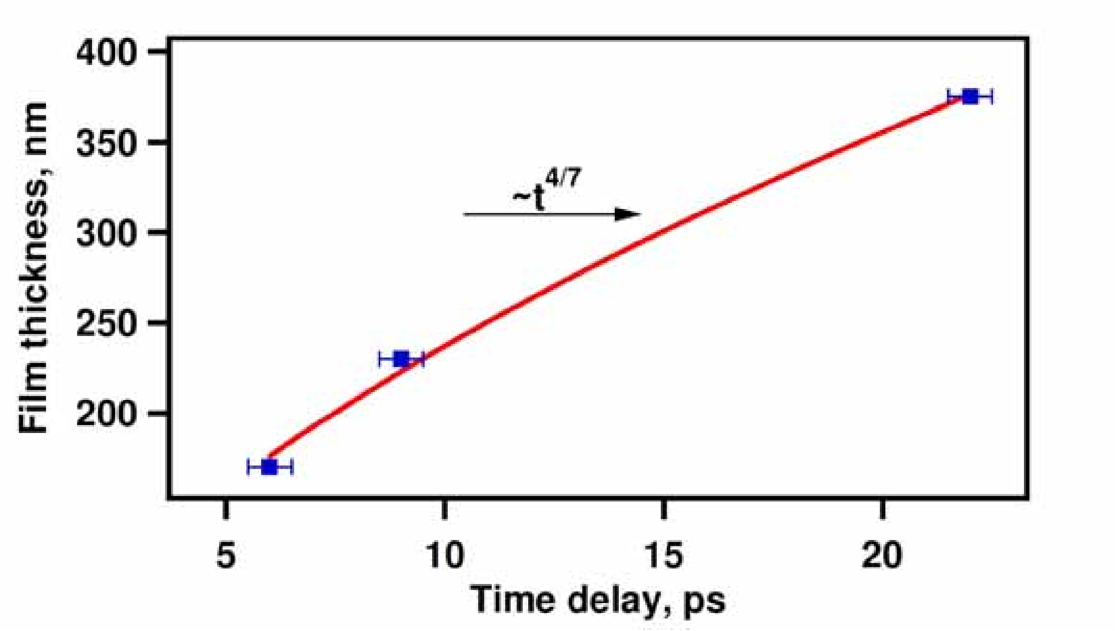

Figure 6.10 The time dependence of the heat front propagation in the target (squares) and the fitted power curve (line).

6.5 SHOCKED MATERIAL

Simultaneous measurements of shock velocity, U_{shock} and particle velocity, $U_{part.}$ are required in order to determine the equation of state of shocked material. Figure 6.9 shows the time dependent reflectivity and phase shift changes for different thickness targets irradiated at the same intensity. The particle velocity was extracted by fitting the line to the phase slope at times after the laser heating, and found to be 9.6 km/s and 4.6 km/s for the 170 nm and 230 nm targets respectively (Figure 6.6 (b), Figure 6.7 (b)). The shock velocity was obtained by substracting the shock breakout time measured for the same laser intensity and the two aluminum target thicknesses, and found to be ~20km/s for the 170 nm and 230 nn targets irradiated at $2.4*10^{14}$ W/cm^2 intensity. These velocities agree with the Equation of State (EOS) of shocked materials with a particle velocity above 6 km/s. The following empirical forms for the aluminum EOS were used [78] (particle and shock velocities are in km/s):

$$U_{shock}(U_{part.}) = 5.33 + 1.356 * U_{part.}, 0 \le U_{part.} \le 6.1$$
$$U_{shock}(U_{part.}) = 6.541 + 1.158 * U_{part.}, 6.1 \le U_{part.} \le 22 \tag{6.7}$$

The particle velocity obtained for 230 nm target was smaller (<6 km/s) resulting in smaller shock velocity compared to those derived from the EOS in Table 6.1. The shock velocity obtained from the measured shock breakout times for 230 nm and 375 nm targets irradiated at the intensity 3.6*10^{14} W/cm^2 (Figure 6.7 (b), Figure 6.8 (b)) is in agreement with the EOS in Table 6.1. Since the propagation distance of the pressure pulse in the target during the 60 fs laser pulse duration is much smaller the target thickness, a strongly decaying shock wave is expected. The decaying shock wave results in the smaller particle velocity obtained for the thicker target. Table 6.1and Table 6.2 shows that the shock velocities obtained using empirical EOS are in reasonable agreement with the shock velocities obtained by subtracting the shock breakout time for different target thicknesses.

Table 6.1 Particle, U_particle and shock, U_shock velocities obtained for the targets irradiated with 2.4*10^{14} W/cm^2 intensity.

	U_particle	EOS U_shock	Extracted U_shock
170nm	9.6km/s	17.7km/s	17km/s
230nm	4.6km/s	11.5km/s	17km/s

Table 6.2 Particle, U_particle and shock, U_shock velocities obtained for the targets irradiated with $3.6*10^{14}$ W/cm^2 intensity.

	U_particle	EOS U_shock	Extracted U_shock
230nm	6.7km/s	14.3km/s	14.5km/s
375nm	4.9km/s	12km/s	14.5km/s

Comparing our experimental results to the simulation of Ng [24] for a 400 nm target heated with a 400 nm pulse at $2.6*10^{14}$ W/cm^2 intensity, the shock breakout time of 24 ps obtained in the simulation is in agreement with our experimental result. The Ng simulation done for the 800 nm probe did not take into account the bound electron contribution. Since the bound electron contribution to the dielectric function is dominant for this wavelength, it does not make sense to compare other details of the time-dependent reflectivity and phase shift simulations to our experimental results. However, the heat front arrival time obtained in our experiment for 170 nm target suggests a higher value of 10^{18} W/m^{3}K for the coupling constant, due to the electron ion energy exchange.

6.6 OBTAINING TEMPERATURE DEPENDENT CONDUCTIVITY

The experimental data were analyzed by numerical hydrodynamic simulations which calculate space and time dependent temperature and density profile. To do the simulation the equation of state (EOS) model, providing pressure and energy as a function of density and temperature, has to be known. The success of experimental simulation depends on the availability and quality of this EOS data. One dimensional hydrodynamic code HYADES [79] was used to simulate the laser heating of the target.

The primary simulations were done using HAYDES 2001 version available in the lab. To simulate the laser coupling to target the wave source was used. The source utilizes the Helmholtz wave equation solution package, where the frequency dependent dialectric function, $\varepsilon(\omega)$, is used to calculate the penetration and absorption of the electromagnetic wave:

$$\varepsilon(\omega) = \varepsilon_{re}(\omega) + i\varepsilon_{im}(\omega) = (\eta(\omega) + i\gamma(\omega))^2, \qquad (6.8)$$

The index of refraction and absorption are noted by η and γ.

Since the target been heated from room temperature to few eV by the laser, it was important to address low temperature, solid state effects. In the hydrodynamic code the solid states behavior is described by the semi-empirical formulas and required some input data. For temperatures below 0.5eV the thermal conductivity was set to $2.33*10^{14}$ erg/s*cm*keV. The melting model has been used as well.

With the use of the wave source it was possible to simulate the fs laser heating of the aluminum film. The heated film dynamics was roughly reproduces by booth the HYADES 2001 and HYADES 2007 code versions. By implementing the Maxwell wave solver to calculate the film optical response, it was found that the two codes produce significantly different results. The two version of the code gave different initial values of the electron density and electrical conductivity. By order of magnitude lower values of initial parameters in the HYADES 2001 version result in low initial reflectivity and higher absorption at later times causing early reflectivity and phase shift drops compared to the calculation made with the new version output parameters.

The HYADES 2007 code version was chosen to simulate the experimental results. The currently available Livermore EOS (LEOS) for aluminum was used in the simulation. LEOS is a quotidian EOS (QEOS) [80] with the incorporated currently available data. Lee and More conductivity model [42] is used in the code to take into account dense plasma effects. The output of the hydrocode is a one dimensional array of the parameters as function of mesh number given at every time step. The target was divided into layers, the so called meshes. The example of electron temperature distribution inside the target at different times is shown in Figure 6.11.

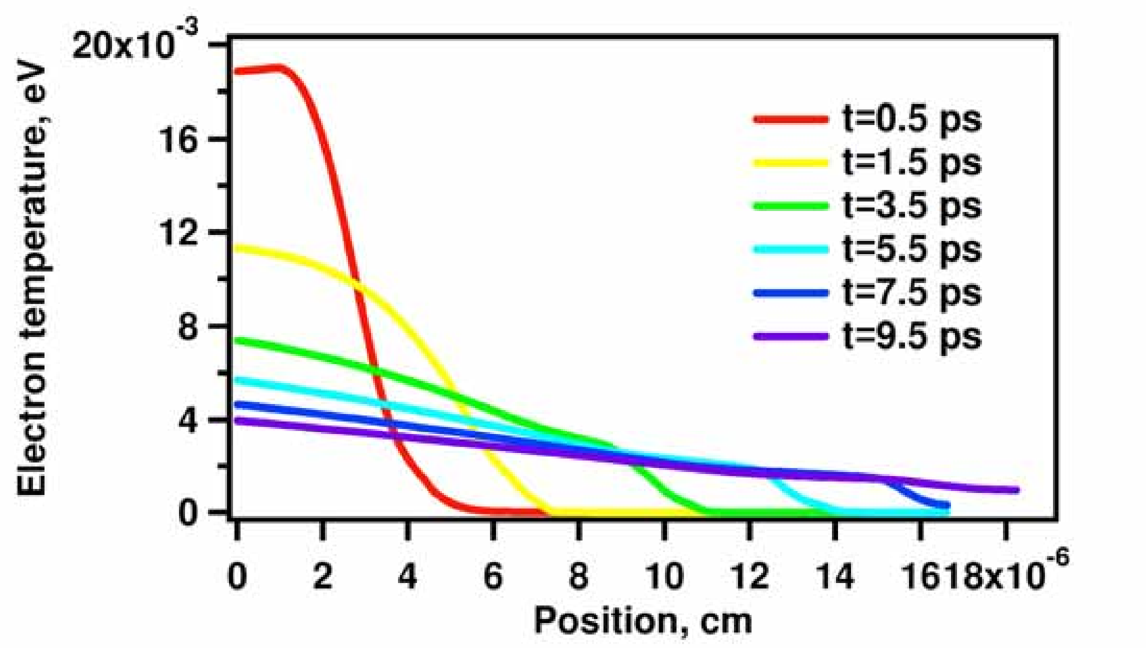

Figure 6.11 Electron temperature distribution inside 170 nm Al target heated with 2.4*10^{14}W/cm^2 obtained in HYADES.

To determine the film optical response, Maxwell's equations were solved via a matrix transfer method (described in Chapter 3) [52]. The aluminum film was divided into 190 layers, the so-called meshes in hydrocode. The dielectric function was given as $\varepsilon(x,\omega)=1+i4\pi\sigma(x,\omega)/\omega$, where x is a coordinate in a density gradient direction, $\sigma(x,\omega)$ is a total optical conductivity. The total optical conductivity at 800 nm contained the contribution from both bound and free electron $\sigma(x,\omega)=\sigma_{free}(x,\omega)+\sigma_{bound}(x,\omega)$. The free electron contribution was described by Drude $\sigma_{free}(x,\omega)=\sigma_{DC}(x)\nu(x)/(\nu(x)-i\omega)$, with dc conductivity $\sigma_{DC}(x)$, angular frequency ω, and collision frequency $\nu(x)$. Bond (covalent) electron contribution was important because of a strong interband transition in aluminum at 1.5 eV that is a result of parallel band structure in the planes parallel to the (200) faces of the Brillouin zone in the fcc aluminum [55].

While lattice properties do not change significantly before the shock wave's arrival at the back surface, the increase in ion and electron temperature causes the increase in collision frequency that affects the optical conductivity by shifting the interband absorption. The formulas for the real and imaginary parts of $\sigma_{bound}(x,\omega)$ were derived in [55]. The $\mathrm{Re}[\sigma_{bound}(x,\omega)]$ is significantly larger than $\mathrm{Re}[\sigma_{free}(x,\omega)]$ (Figure 3.8) indicating that the interband is the dominant light absorption mechanism at 800 nm for aluminum. Both free and bound electron contributions to the total optical conductivity are functions of collision frequency. The collision frequency in the studied temperature range was defined by the bulk properties of a film $\nu(x)=\omega_{pl}^2(x)/(4\pi\sigma_{DC}(x))$, where ω_{pl} is the plasma frequency.

Using the output of the HYADES simulation $\sigma(x,\omega)$ was computed and incorporated in a Maxwell wave solver for calculating the interaction of electric field at the film surface. Figure 6.12 shows the results of a comparison between the calculated time-dependent reflectivity and phase shift and experimental data obtain from 170 nm aluminum film irradiated at 2.4 10^{14} W/cm^2. The Lee and More model was in good agreement with our measurement. The shock breakout time obtained from the hydrodynamic simulation reproduced the experimental results. It is informative, then, to look at the dynamics of the foil in the first 8.5 ps, corresponding to the time before the shock wave's arrival at the back surface. The electron temperature changes at the back surface prior to the shock breakout, as shown in Figure 6.12(c). For 3 ps the back surface of the target sees a continuous transition from room temperature to few eV, while the heated back surface keeps a sharp interface to vacuum. The reflectivity dropped during this time, and the phase changed. As shown in [48] the reflectivity changes are correlated with the temperature increase but not with the increase of internal target pressure. The plasma is near solid density in the period when the shock wave did not yet reach the back surface of the target, with the small temperature gradient defined by the electron thermal conduction. The dielectric constant and optical conductivity were extracted from our simultaneously measured reflectivity and phase shifts over the 0.1 to 1.5 eV temperature range using Fresnel's equations. In Figure 6.13 the extracted real and imaginary parts of optical conductivity were compared to calculated values using the Lee and More conductivity model. The error bars for the real and imaginary parts of optical conductivity were evaluated by propagating the error for the measured reflectivity and phase changes using the Fresnel's equations. As the temperature increased, the imaginary part of the optical conductivity dropped, indicating the Ohmic-like conductivity of a metal. The real part showed more complicated temperature-dependence; it approached a stable value after the temperature was changed from the room temperature. The initial drop of both the real and imaginary parts of the conductivity indicates that the film was more absorptive at higher temperature. There is some discrepancy between the calculated imaginary part of conductivity and the experimentally obtained below 0.3 eV. At our probe frequency the dominant absorption mechanism was the interband absorption, indicating that the discrepancy was caused mostly by the bound electron contribution to the conductivity calculation, though temperature-dependent changes in the lattice that were not taken into account[57]. In the previous works it has been shown that the calculated Lee and More DC conductivity is at least an order of magnitude higher than measured values for warm (<.6 eV), moderately dense (1.6 g/cm^3) aluminum [10, 47]. Our data at solid density (2.7 g/cm^3) aluminum indicates that the Lee and More model predicts the real and imaginary parts of optical conductivity within 20%.

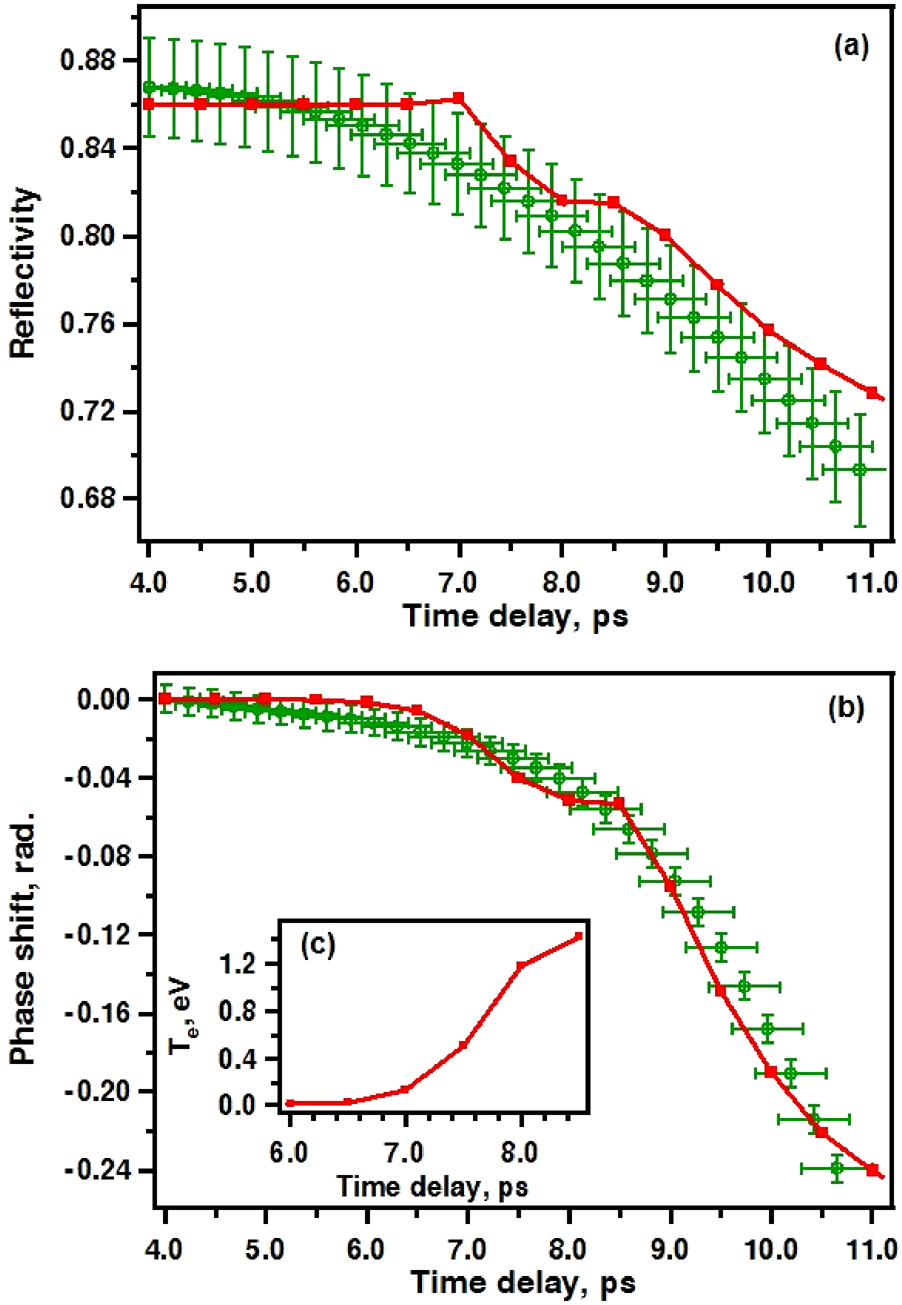

Figure 6.12 Time dependences of the (a) reflectivity and (b) phase shift changes from the laser-heated aluminum target at 2.4*1014W/cm2 (circles) compared to the calculated ones (squares) obtained using HYADES output. (c) Time dependence of the back surface average electron temperature obtained in HYADES.

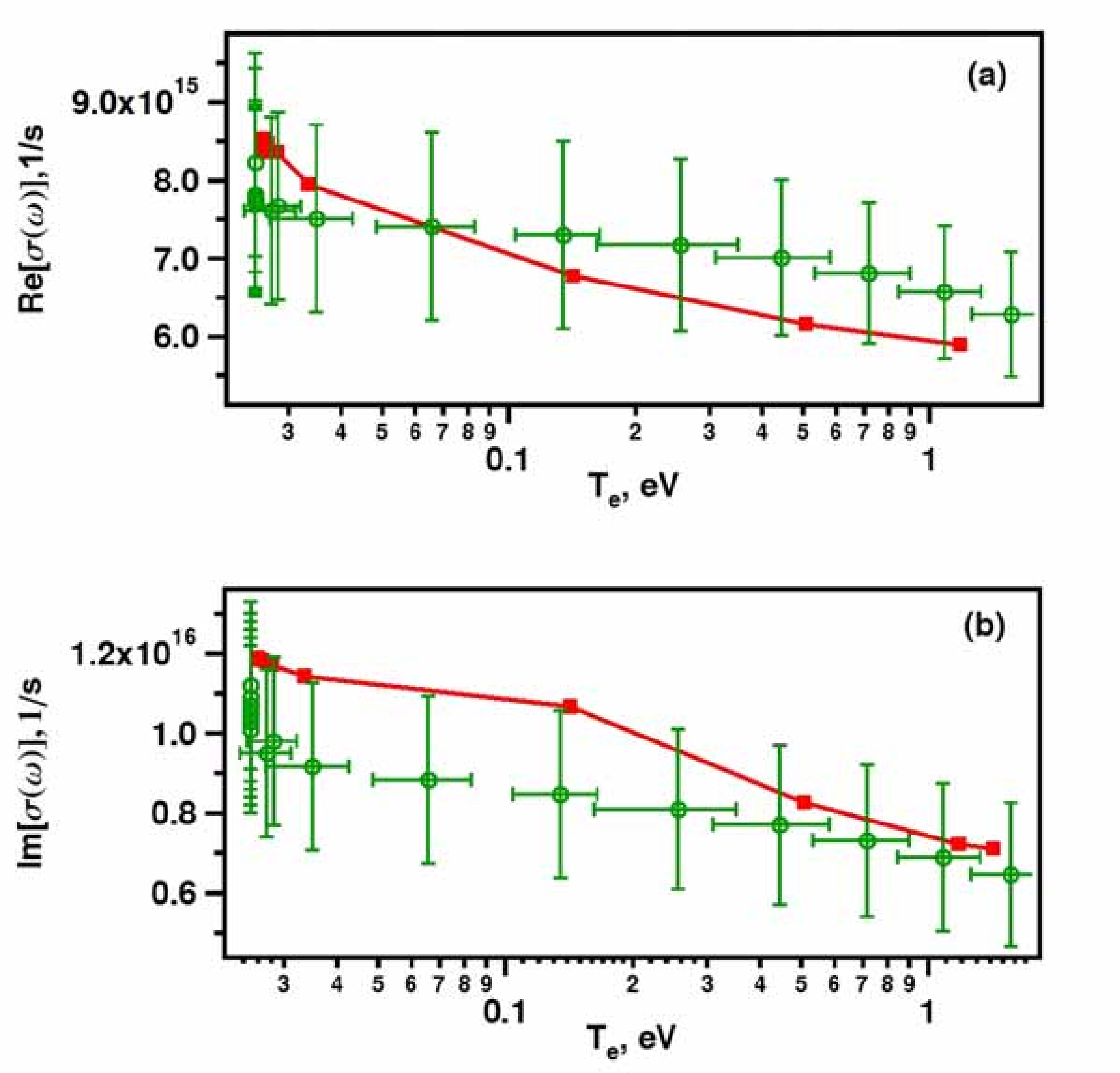

Figure 6.13 Temperature dependences of (a) real and (b) imaginary parts of optical conductivity extracted from the measured optical parameters (circles) compared to the calculated ones (squares) obtain using HYADES output.

Following the analysis outlined in the previous paragraph, simulations were done for the data obtained from our measurements for 170, 230, and 375 nm aluminum foils heated with the intensity of 1-5 x 10^{14} W/cm^2. The calculated optical response using the HYADES output was compared to the measured reflectivity and phase shift changes

(Figure 6.14, Figure 6.15, Figure 6.16, Figure 6.17). The electron temperature changes at the back surface prior to the shock breakout, extracted from the hydrocode, are shown in part c of Figure 6.14, Figure 6.15, Figure 6.16, and Figure 6.17 as well. The maximum temperature reached at the back surface due to the thermal conduction wave from the laser-heated front surface before the shock wave arrival is in the 0.5-1.5 eV range, depending on the target thickness and irradiated laser intensity. The calculated optical parameters using the HYADES output are in reasonable agreement for 170 nm and 230 nm targets heated with 2 - 4 x 10^{14} W/cm^2 intensities.

The optical conductivity values were extracted over the first 8-20 ps (depending on the target thickness and laser irradiated intensity) of the measurement corresponding to the time before the shock wave's arrival at the back surface. The real and imaginary optical conductivity values were obtained in the 0.1-1.5 eV range. It was found that the obtained values for the 170nm, 230 nm foils heated with the 2 - 4 x 10^{14} W/cm^2 laser intensity were consistent with (and correspond to) the values presented in Figure 6.13. The extracted conductivity values for different data sets are shown in Figure 6.18. As it was seen from Figure 6.18, the values were consistent within the error of the measurement. Using the approach of optically probing the back surface of the foil heated by the thermal conduction wave from the laser-heated front surface we were able to gain information about the dielectric constant of dense aluminum in 0.1-1.5eV range.

The extracted conductivity values for the 170 nm target irradiated with 1.8x10^{14} W/cm^2 intensity and for 375 nm irradiated under 1.8x 10^{14} W/cm^2 are within ~30% of the values presented in Figure 6.18. The values obtained for the real part of the conductivity showed a discrepancy only within 0.1-0.6eV range. This can be attributed to the accuracy of the experimentally taken data and the calculation based on the HYADES output. The calculated optical parameters for a 400nm heated target using HYADES output are in poor agreement with the measured parameters (Figure 6.17), and that affected the accuracy of determining the temperature at the back surface of the heated foil. The maximum electron temperature reached at the back surface of this target was in 0.5-0.7 eV range according to the HYADES simulation. At the same time, the dominant absorption mechanism in aluminum at the probe wavelength of 800 nm is interband absorption. In this case the discrepancy is caused mostly by the bound electron contribution to the conductivity calculation, though temperature-dependent changes in the lattice that were not taken into account[57].

Overall, my calculation showed that the optical conductivity values obtain using the Lee and More conductivity model, coupled with the published model of bound electron contribution to the optical conductivity, are in reasonable agreement with the extracted values (within 20%). It was found that in the cases of 170 and 230 nm aluminum target irradiated with 2 - 4 x 10^{14} W/cm^2, we derived the same conductivity, though the arrival of the heat wave and subsequent shock waves varied with the choice of intensity and target thickness. This consistency in our data gives us good confidence in the validity of our technique for deriving conductivity as a function of temperature.

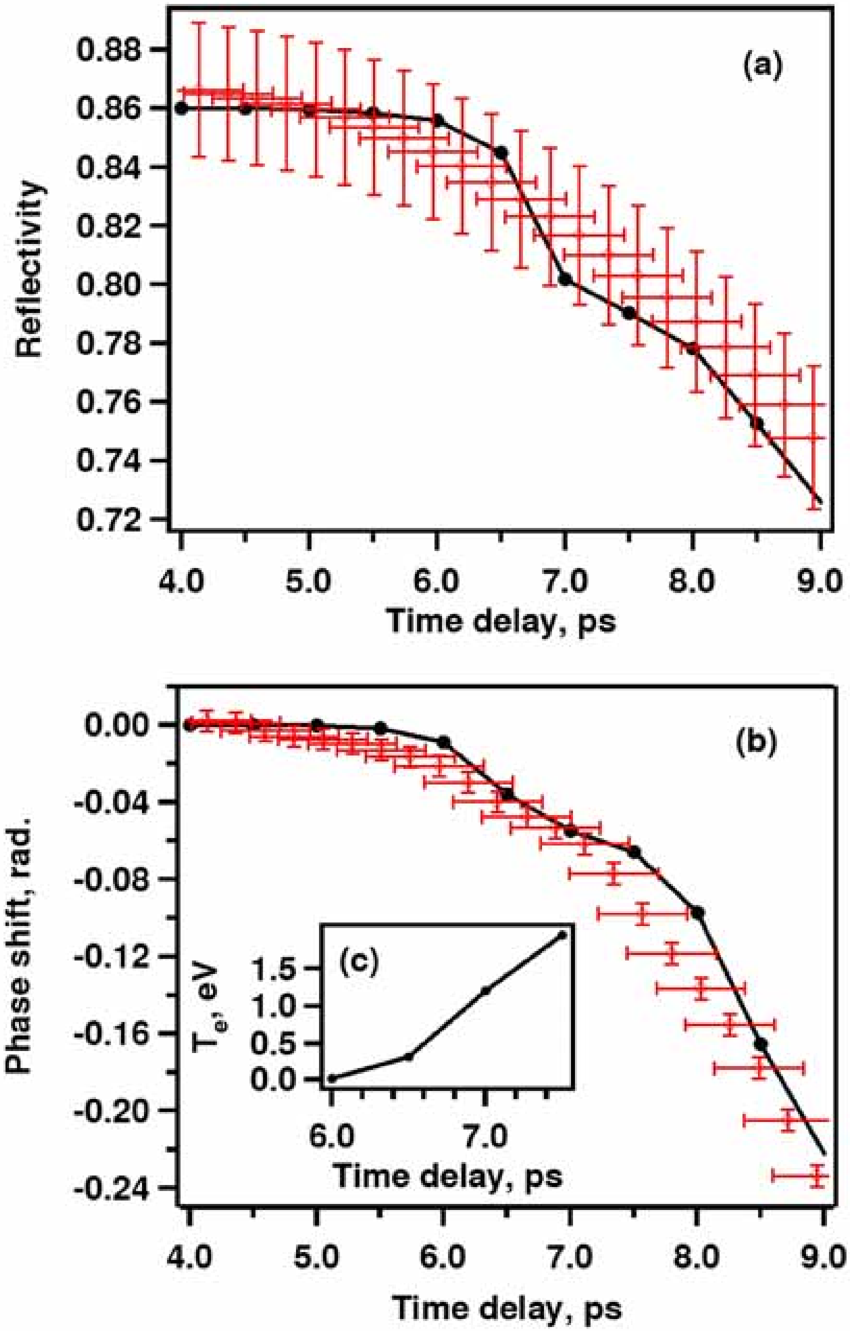

Figure 6.14 Time dependences of the (a) reflectivity and (b) phase shift changes from the laser-heated 170nm aluminum target at 3*10^{14}W/cm^2 (open circles) compared to the calculated ones (line) obtained using HYADES output. (c) Time dependence of the back surface average electron temperature obtained in HYADES.

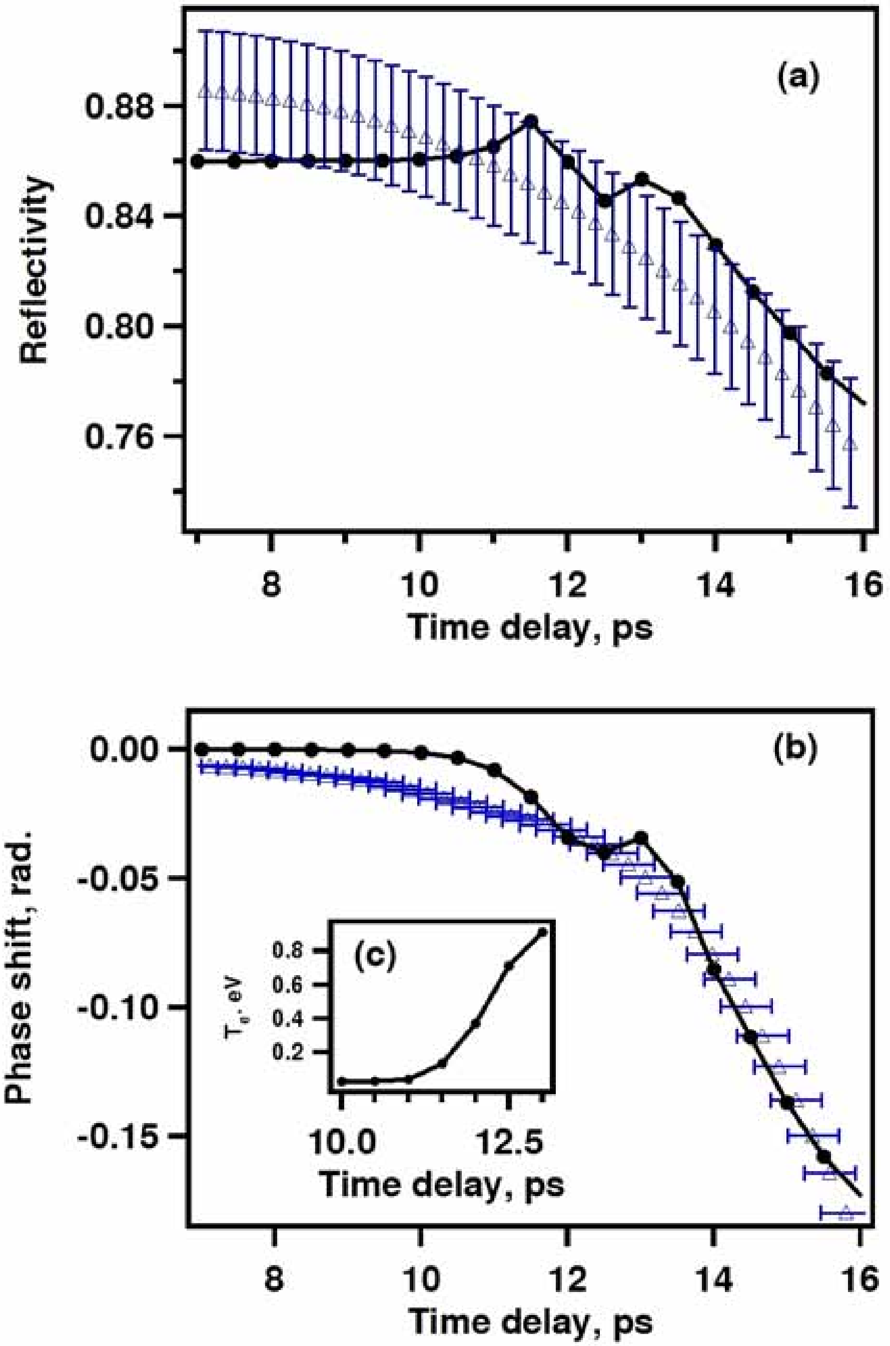

Figure 6.15 Time dependences of the (a) reflectivity and (b) phase shift changes from the laser-heated 230nm aluminum target at $2.4*10^{14}$W/cm^{2} (triangles) compared to the calculated ones (line) obtained using HYADES output. (c) Time dependence of the back surface average electron temperature obtained in HYADES.

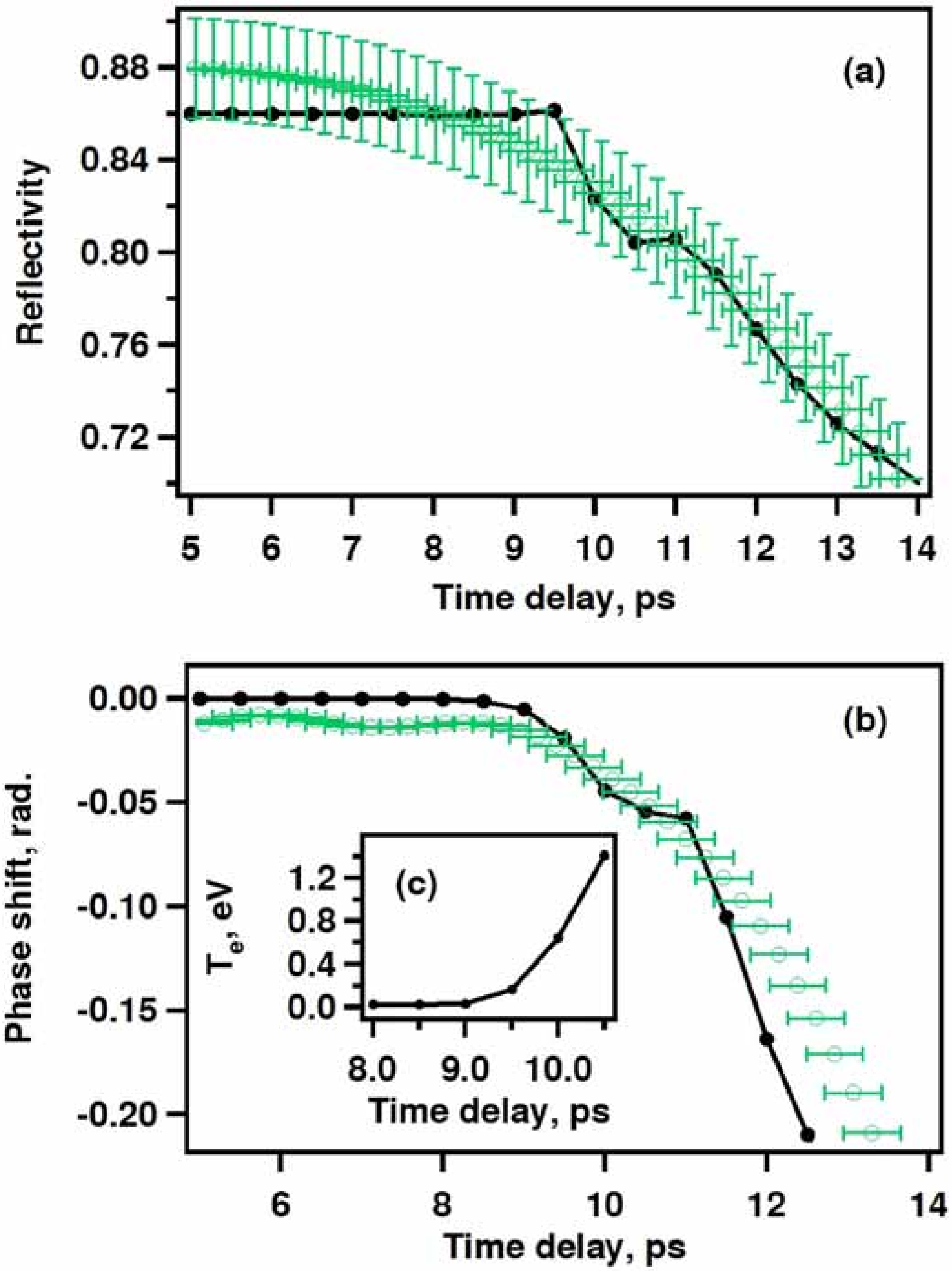

Figure 6.16 Time dependences of the (a) reflectivity and (b) phase shift changes from the laser-heated 230nm aluminum target at $3.6*10^{14}$W/cm^2 (open circles) compared to the calculated ones (line) obtained using HYADES output. (c) Time dependence of the back surface average electron temperature obtained in HYADES.

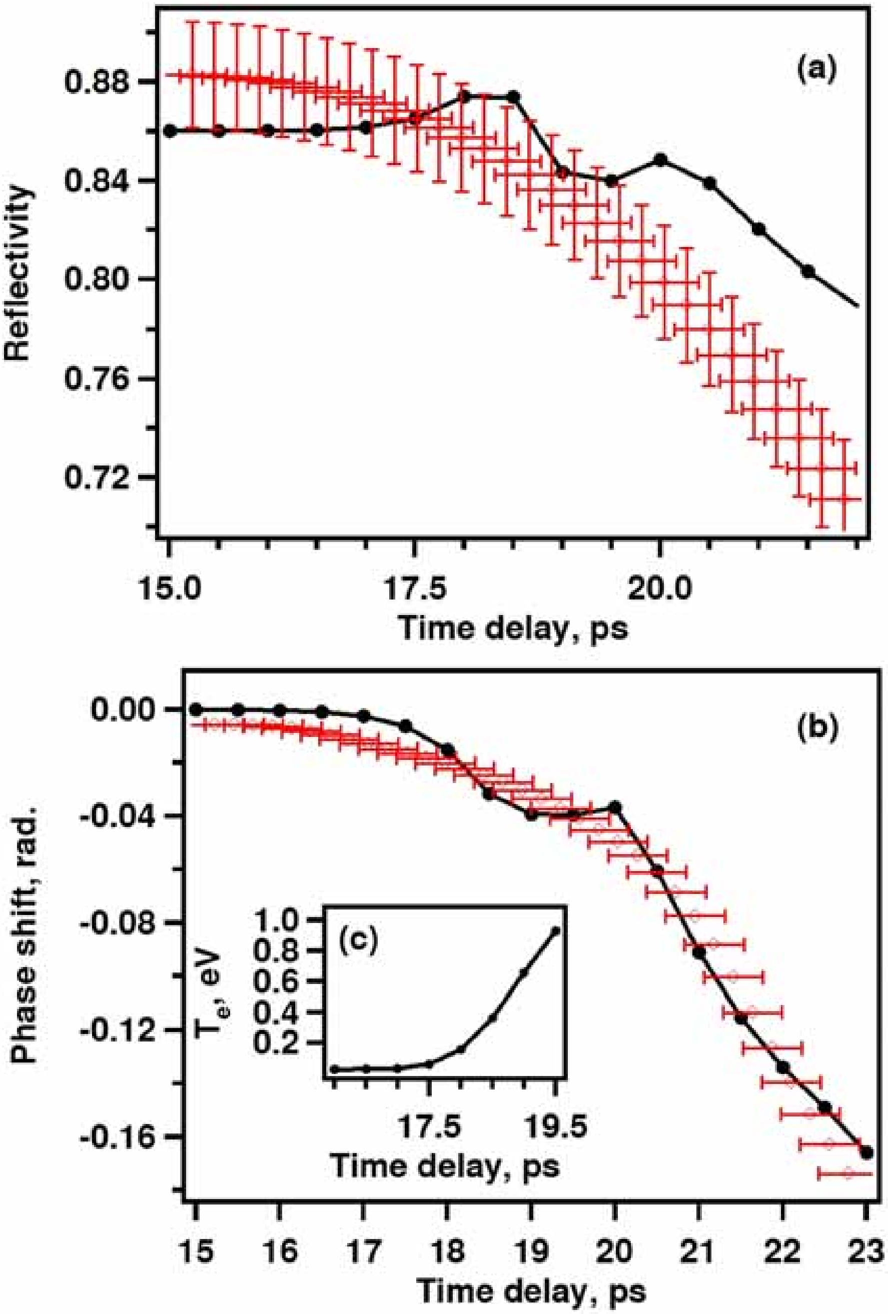

Figure 6.17 Time dependences of the (a) reflectivity and (b) phase shift changes from the laser-heated 375nm aluminum target at $4.2*10^{14}$W/cm^2 (open circles) compared to the calculated ones (line) obtained using HYADES output. (c) Time dependence of the back surface average electron temperature obtained in HYADES.

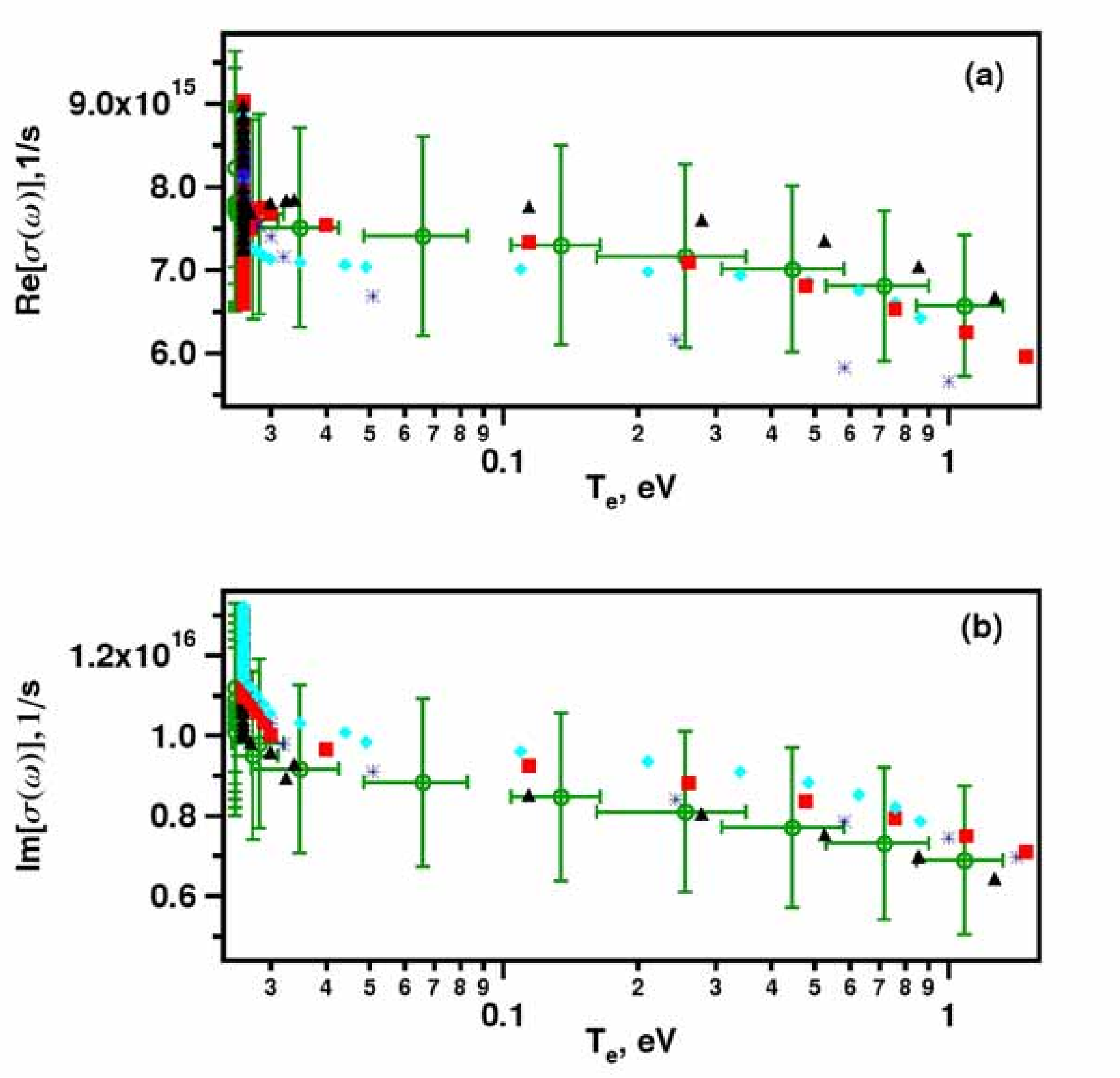

Figure 6.18 Temperature dependences of (a) real and (b) imaginary parts of optical conductivity extracted from the measured optical parameters of 170nm aluminum target heated with intensity of 2.4*10^{14} W/cm^2 (open circles), 3*10^{14} W/cm^2(snow flakes). The conductivity was also extracted for 230 nm target heated with intensity of 2.4*10^{14}W/cm^2 (rhombs), 3.6*10^{14}W/cm^2(squares) and 4*10^{14} W/cm^2 (triangles).

7 Conclusions

7.1 SUMMARY

The goal of this work was to study electron thermal transport properties, such as thermal and electrical conductivity in the laser-heated solids. Solid aluminum was chosen as a target since it is well studied material and the current equation of state (EOS) is available. To gain information about the electron thermal transport two experiments were conducted on the THOR laser. The new approach of probing the back surface of the heated target was implemented in both experiments.

The goal of the first experiment was to study the dynamics of the heated thin (40nm) aluminum film by measuring the back surface reflectivity of the target. Such a thin foil with thickness of only a few skin depths was chosen since it can be nearly uniformly heated by the femtosecond pulse. By measuring the back surface reflectivity changes of the reflected probe I was able to capture the dynamics of expanded material heated with an intensity of $5*10^{13}$ W/cm^2. Since the aluminum foil was supported by the formvar-carbon layer for the stability, the absorption in the supporting layer had to be taken into account in the analysis. To be able to study electron conduction mechanism in a purely laser-heated aluminum film the free-standing metal foil was used. Using the fundamental frequency of the THOR laser required keeping the intensity of the heating beam below 10^{14} W/cm^2 in this experiment to avoid any target modification by the pre-pulses before the heating pulse arrival. Finally, measuring only one optical parameter was not enough for gaining information about the dielectric function of the heated solid. The unclear result of the first experiment and the need for future improvements led me to design a second experiment.

The goal of the second experiment was to gain more information about the dielectric constant of warm dense aluminum. The approach taken in this experiment was to probe the back surface of a thicker (170-375nm) metallic foil heated by a thermal conduction wave from the laser-heated front surface[24]. Such an approach requires measurement of both reflectivity and reflected probe phase shift to derive information on real and imaginary parts of the dielectric function. The frequency domain interferometry diagnostic with chirped pulses was designed and built in order to allow me to simultaneously measure the reflectivity and phase changes of the reflected probe from the heated matter in a single shot. The diagnostic was successfully implemented for probing the back surface of the aluminum free standing foils heated with the 1-5*10^{14} W/cm^2 intensity. Using thin foils I was able to observe the thermal wave created by the heating laser as it propagated ahead of the shock wave in the sample. For several ps prior to the shock breakout, the temperature on the back surface ramped up from the arriving thermal wave, while the heated back surface kept a sharp interface to vacuum. During this time window, the reflectivity and phase changes allowed us to gain information about the heated solid. Using these dynamics I was able to extract, on a single shot, the dielectric constant and optical conductivity simultaneously over the 0.1 to 1.5 eV temperature range using Fresnel's equations. It was found that the imaginary part of the optical conductivity exhibits Ohmic-like conductivity in the studied temperature range. The obtained results were compared with the dense plasma conductivity model using the hydrodynamic simulation code HYADES. Using the HYADES outputs coupled with published models of bound electron contributions to the conductivity the optical parameters were calculated and were shown to be in reasonable agreement with the measurement. Using the simulation results the temperature dependent optical conductivity of solid aluminum was obtained in the 0.1 to 1.5 eV and compared to the

Lee and More (LM) conductivity model. LM model predicts the real and imaginary part of the optical conductivity within 20%. The temperature dependence of the conductivity was examined using 170 and 230 nm aluminum foils heated with the intensities of 2 - 4 x 10^{14} W/cm^2, as well as for 375 nm aluminum foil heated with the intensities of 4 x 10^{14} W/cm^2. It was found that in all cases, the same conductivity was obtained, though the arrival of the heat wave and subsequent shock waves varies with the choice of intensity and target thickness. This consistency in the data gave us good confidence in the validity of this technique for deriving conductivity as a function of temperature.

7.2 FUTURE WORK

It will be important to probe the aluminum foil heated by a thermal conduction wave from the laser-heated front surface at 400nm, because at that wavelength there will be no bound electron contribution to the optical response. The dielectric constant at this wavelength is defined solely by the free electron contribution, and using the Drude model it will be possible to evaluate the collision times for warm dense aluminum, $\tau = \mathrm{Im}[\sigma(\omega)]/(\mathrm{Re}[\sigma(\omega)]*\omega)$. In designing this experiment the attention should be paid to the heating beam. It should be prevented from leaking to the imaging system of the probe beam. It was straightforward to do it with 800 nm probe and 400 nm pump beams, by using the filter at the entrance slit of the spectrometer. Using the off normal angle of incidence for the heating beam can help in rejection of the heating beam leakage to the imaging system.

It will be also interesting to implement this technique for different materials such as gold. The faster relaxation time in gold may lead to different dynamics between the thermal and the shock waves in the material. It will be also possible to check the dense plasma conductivity model validity for high Z materials.

The next step in studying the thermal transport properties is to go to higher irradiated intensities. In the intensity range of 10^{16}-10^{19} W/cm^2 it will be important to consider the anomalous skin effect[76], when laser energy is absorbed into the target. At high temperature the radiative thermal transport will dominate over the collisional electron transport. In this intensity range it will be possible to heat solids to temperature exceeding the Fermi temperature. At such high temperature it will be informative to learn about electronic properties of dense plasma by using VUV and XUV pulses. Techniques similar to those employed in this thesis should be used to avoid probing the density gradient in hot expanding matter that is created immediately after the laser heating.

Appendix A X-ray generation from modified surfaces

When a high-power laser pulse irradiates a cold solid, a dense, high-temperature plasma is produced. Laser energy gets absorbed either by inverse Bremsstrahlung [44] during electron collisions with ions or by collisionless absorption mechanisms, such as resonance absorption [37] or vacuum heating [58]. A dense plasma with temperature in the range of 0.1-10 keV can be created immediately after the laser pulse absorption. Most of the absorbed energy is released through ionization processes in the atoms contained in the target material, in which electrons in low electronic states are released followed by strong radiation of X-rays by the highly charged ions. The intensity contrast at the leading edge of the short excitation pulses is increased in order to prevent the formation of a long, low-density plasma pedestal, and allows the laser energy deposition to take place in a high-density plasma. At high plasma density the electron thermal conduction as well as the expansion and cooling happens on a shorter time scale that causes a decrease in the duration of the x-ray pulses that are produced. However at such high density the plasma surface acts as a good mirror, preventing plasma from absorbing additional laser energy. Additional ways to increase absorption through collisionless laser absorption mechanism, like vacuum heating or resonance absorption, can only be implemented at off-normal angle of incidence. It was suggested that the use of modified surfaces to improve the absorption and to reduce the reflection may be used to avoid lowering of the effective intensity on the target associated with using off-normal angles of incidence.

Several experiment in the past studied the effect of nanometer structuring surfaces on increase of laser absorption as well as on yield in X-ray production. In one of the earlier experiments[81] is been shown that replacing the plane target with the grating or covering the surface with the gold nanoclusters it is possible to increase the absorption by 10%. By using the nanostructured "velvet", consisting of 10-200nm diameter metallic long fibers, Kulcsar [82] *et al*. enhanced the soft (125 eV) x-ray production by a factor of 50 over a flat target using 1 ps pulses at 10^{17} W/cm^2 intensity. Gavrilov [6] *et al.* achieved both an increase in efficiency of hard x-ray (1-20 keV) generation, and in hot electron temperature of plasma by using electromechanically modified surface layers, such as craters, pyramidal cavities, porous silicon and gratings.

While most of the previous studies focused on the effect of nanostructured surfaces on x-ray production, it is well known that if the particle size is comparable to the light wavelength (sub micron size), then very large enhancement of the laser field through Mie resonances can be achieved. Previously, Donnelly *et al.* [5] demonstrated the increase in x-ray temperature by irradiating wavelength scale droplets in contrast to the slab targets. Because a large distribution in the size of the droplets were used in that experiment, the effect of Mie resonances for particular particle size could not be studied.

The goal of our work was to study the structure and size effects on field enhancement and hot electron generation from an array of polysterene spheres with a well-defined size deposited on planar target. Precise control of the size and scale of the surface modification, allowed us to determine how specifically the Mie enhancement affects the x-ray and hot electron production by measuring the x-ray yield as a function of the sphere size.

To succeed in our studies several experimental approaches were taken that involved efforts from several graduate students, post docs, as well as a visiting professor. The results of our work were published in several articles [7, 83], as well as in PhD and Master theses.

The experiment was performed on the THOR laser at the University of Texas at Austin. The layout of the experimental set up is shown in Figure A 1. The THOR laser delivers 800 nm, 35 fs pulses with the energy up to 0.7 J. The fundamental wavelength was used in the experiments. Later the 800 nm output was frequency-doubled with a 2 mm thick KDP crystal in air and 12 mJ of 400 nm light was delivered to the vacuum chamber through the glass window, resulting in a ~100 fs pulse. To separate the 400 nm light from the co-propagating fundamental 800 nm light, two dichroic mirrors and the BG 39 glass filter were inserted into the beam line prior to entering the chamber. Inside the chamber 400 nm light was focused with f/2.8 parabolic mirror to a $2*10^{17}$ W/cm^2 peak intensity with a 6 μm diameter focus. The 400 nm light was used to avoid any surface modification due to the pre-pulses before the main pulse arrival. To measure the X-ray signal six NaI detectors shielded in lead housing were used. All detectors were arranged next to each other to provide a similar observation angle through the same thickness of the chamber material (Plexiglas window). Each detector was filtered with slabs of different thickness of copper and aluminum. Table A.1 shows the resulting cutoff energies for each detector.

Table A.1 Filter cut off energy.

Filter	Cut off energy
37 mm of $(C_5O_2H_8)_n$	22.7 keV
3.2 mm of Al	32 keV
6.4 mm of Al	39 keV
0.6 mm of Cu	52 keV
1.2 mm of Cu	65 keV
1.8 mm of Cu	75 keV

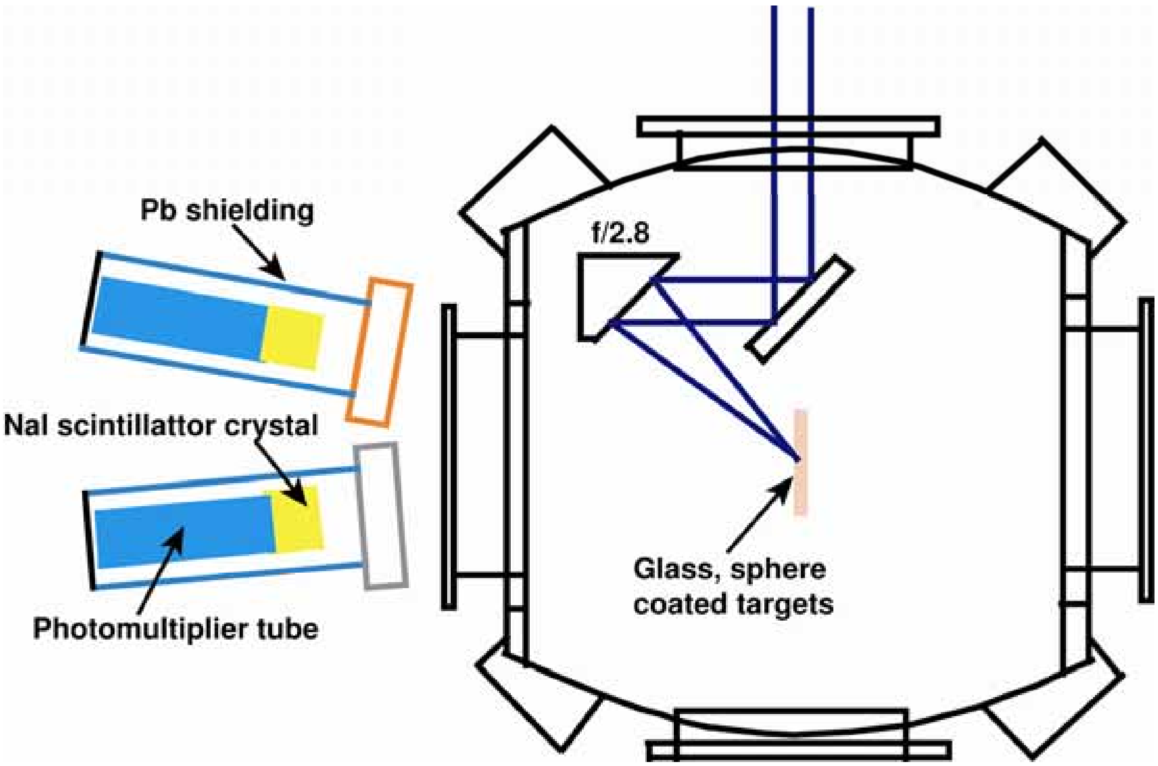

Figure A 1 Layout of the experimental set-up for hard x-ray detection from irradiated sphere coated glass targets.

The targets were prepared by evaporating a sphere suspension on a substrate. After several attempts to produce a monolayer of polystyrene spheres, the best result was achieved by depositing sphere suspension onto a smooth, clean surface. Polished fused silica substrates were found to be the most effective and easily obtainable substrate. Before evaporating the sphere solution the substrates were treated with the Hellmanex soap and rinsed in Millipore water (bi-distilled water). After repeating this procedure for 3 times and drying the substrates in the oven we prepared the substrate surface for the evaporation of the sphere suspension. The suspension of polystyrene spheres was purchased from Duke Scientific and had only 2-3% in particle diameter distribution. The particle suspension was diluted with ethanol and 20 μL droplet of the diluted suspension was deposited on clean fused silica substrate position on the inclined surface at 9^0. Using ethanol as a diluting agent provided faster evaporation time and produced a reasonable coverage. The Duke Scientific sphere suspension with a negligible particle size distribution allowed us to obtain regions of monolayer coverage of spheres on a fused silica substrate (Figure A 2, Figure A 3). As seen from the SEM images the coverage was not 100 %, but with proper imaging of the target surface we were able to select the sphere coated patches for every shot (Figure A 4). The sphere coated targets with sphere's diameter of 0.1, 0.26, 0.5, 1, and 2.9 μm were prepared for the experiment.

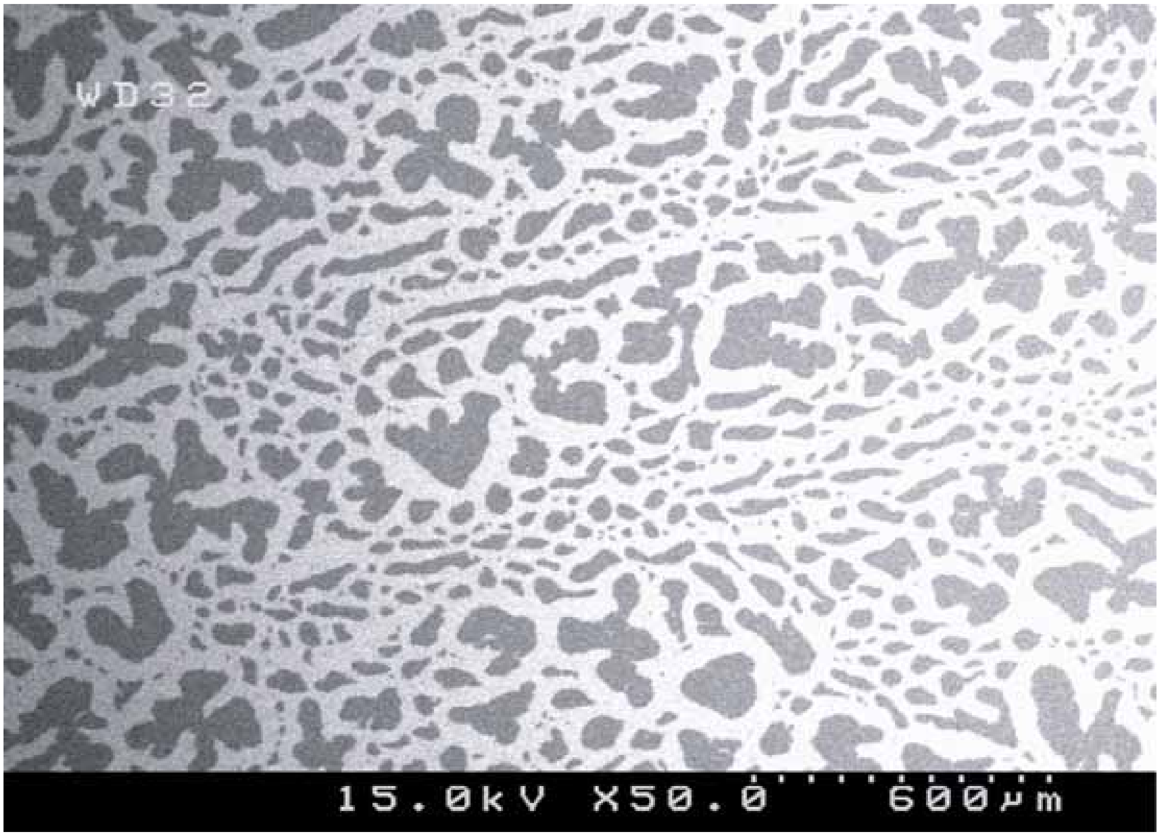

Figure A 2 SEM image of the glass target coated with $0.5 \mu m$ polystyrene spheres.

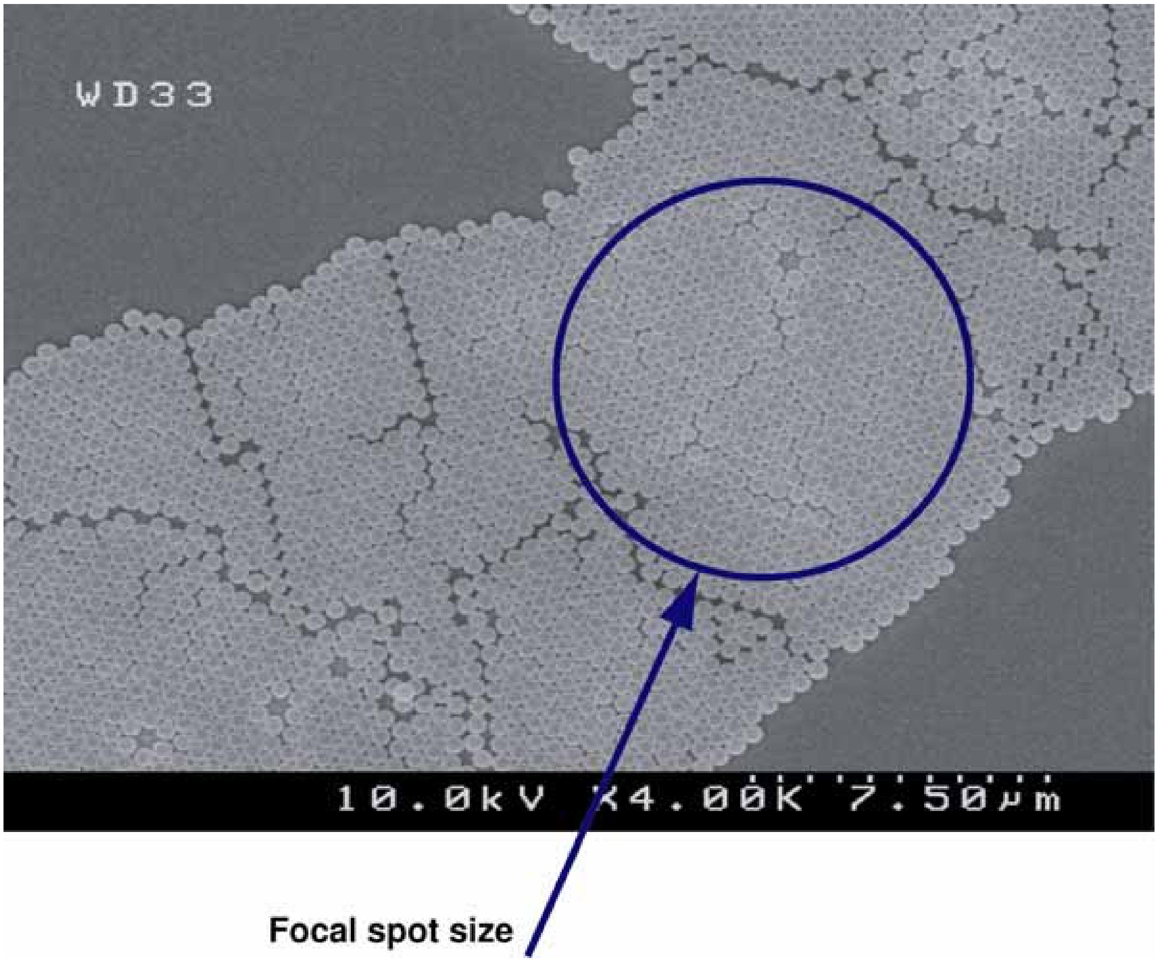

Figure A 3 SEM image of glass target coated with the monolayer of $0.5\mu m$ polystyrene spheres.

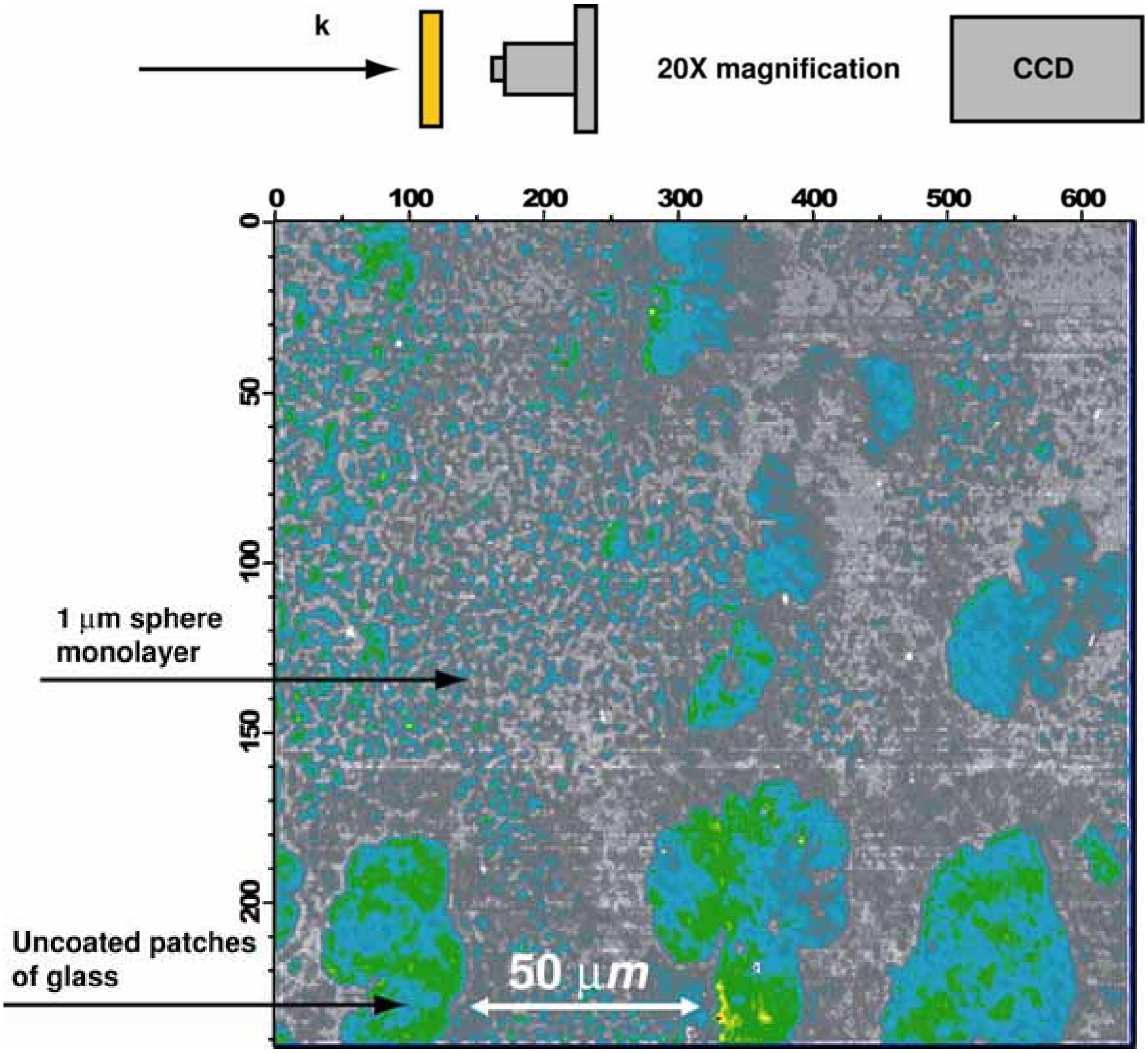

Figure A 4 Schematics of the imaging of the glass substrate with the 20X magnification objective on a camera.

The primary experiments were done with the 800 nm fundamental wavelength of the THOR laser. The 15 mJ 800 nm pulse was focused to an intensity of $1*10^{18}$ W/cm^2. At such high intensity it is important to evaluate the contribution of the pre-pulses in the laser-matter interaction. The pre-pulses were identified earlier using third-order autocorrelation and the autocorrelation scan reviled an intense 24 ps pre-pulse at the 10^{-4} level (Figure 2.4). An angle scan was conducted in order to study the effect of the pre-pulses. The angle scan allowed us to plot the x-ray signal from a single NaI detector versus angle of incidence of p-polarized 800 nm light incident on the unmodified copper target (Figure A 5). The plot shows the peak at 15 degrees, indicating the resonance absorption dominated in hot electron generation. To evaluate this impact, the plasma scale length can be estimated as $L = (c/\omega)*(0.8/\sin\theta)^3$ for angular frequency ω at the max angle of absorption θ. For $\theta = 15$ degrees the plasma scale length was 3.5 μm, suggesting that the sphere monolayer would be destroyed by the time the main pulse arrived.

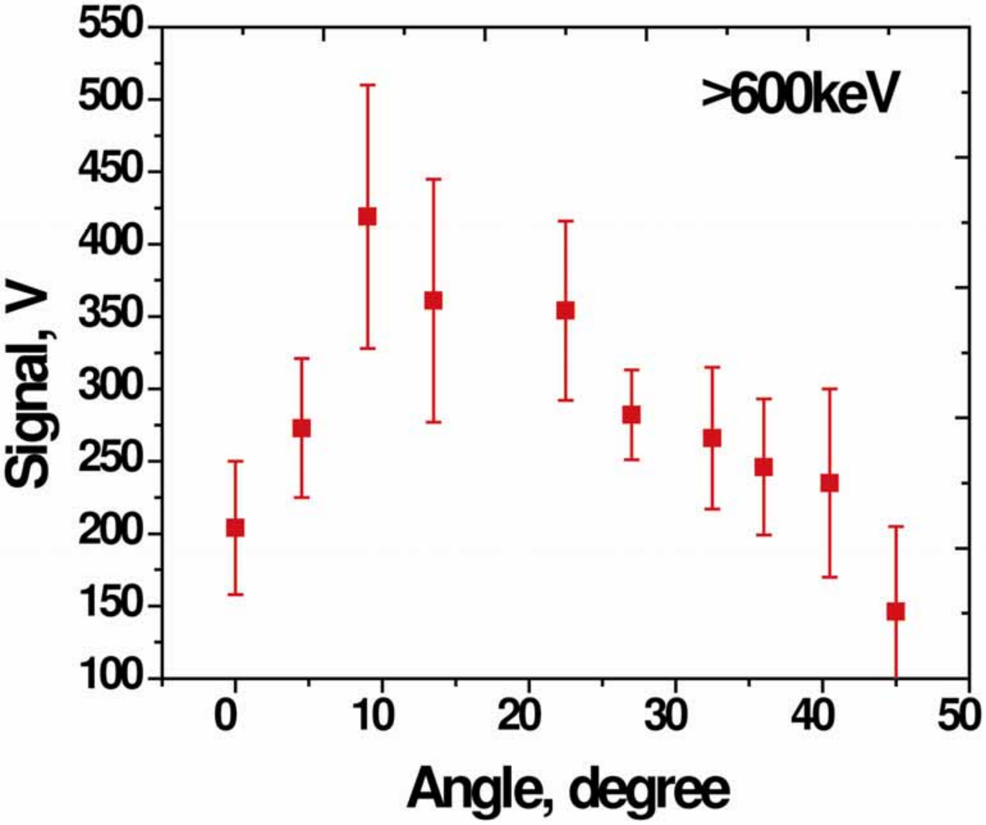

Figure A 5 Angular dependence of >600 keV x-ray yield for polished copper irradiated with 800 nm laser beam.

To avoid modification of the target surface by the pre-pulses before the main pulse arrival, the 800 nm pump pulse was frequency-doubled and filtered to remove the fundamental wavelength. The angle scan was repeated with unmodified fused silica substrate irradiated with p-polarized 400 nm light. The plot of the angle scan is shown in Figure A 6. The peak at 55 degrees indicates the main absorption mechanism is the vacuum heating, which confirmed by the presence of the steep density gradient when the p-polarized pulse was incident on a target. Vacuum heating corresponds to the mechanism when hot electrons are pulled from the plasma by the laser field, accelerated and returned to the plasma surface. In this configuration the angle of maximum absorption of55 degrees is defined by the magnitude of the perpendicular component of the laser electri field at the target surface $E_{\perp} = E_0 \sin\theta\sqrt{\cos\theta}$. For $\theta = 55$ degrees the plasma scale length is under 15 nm, suggesting that the laser pulse will be interacting with the sphere monolayer without any pre-pulse modification.

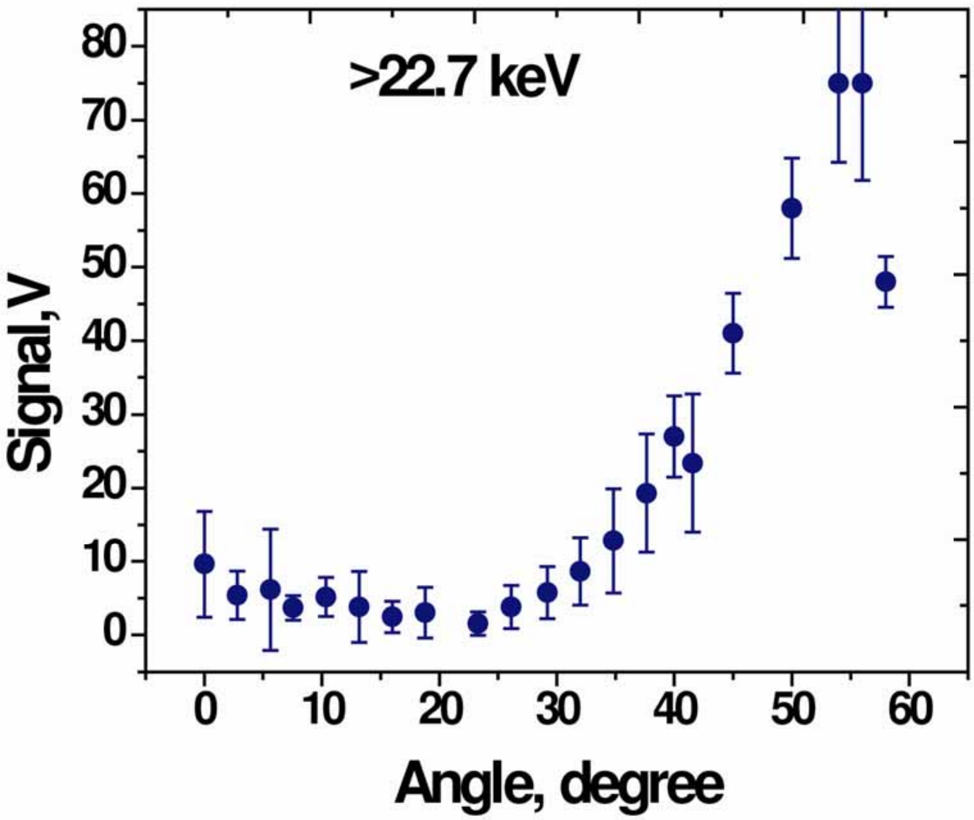

Figure A 6 Angular dependence of >22.7 keV x-ray yield for fused silica irradiated with 400 nm laser beam.

We performed a measurement x-ray emission from the uncoated fused silica slide and the silica slide coated with 0.26 μm spheres when the laser pulse was incident at 55 degrees, the resonance angle for the maximum absorption. The results of the measurement are plotted in Figure A 7. The hot x-ray yield for the sphere coated slide was 4 times higher the uncoated slide's yield at the resonance angle. The temperature fit indicated a higher average electron temperature for the sphere coated slide (25 keV) compared to the uncoated slide's electron temperature (15 keV). The Maxwellian electron distribution was used to determine the average electron temperature. The detector response to the radiation spectrum of temperature kT was determined with the following formula: $G(kT) = \int_0^\infty \frac{Exp(\frac{E_x}{kT})}{kT} FilterAttenuation(E_x) E_x dE_x$, where E_x is the photon energy.

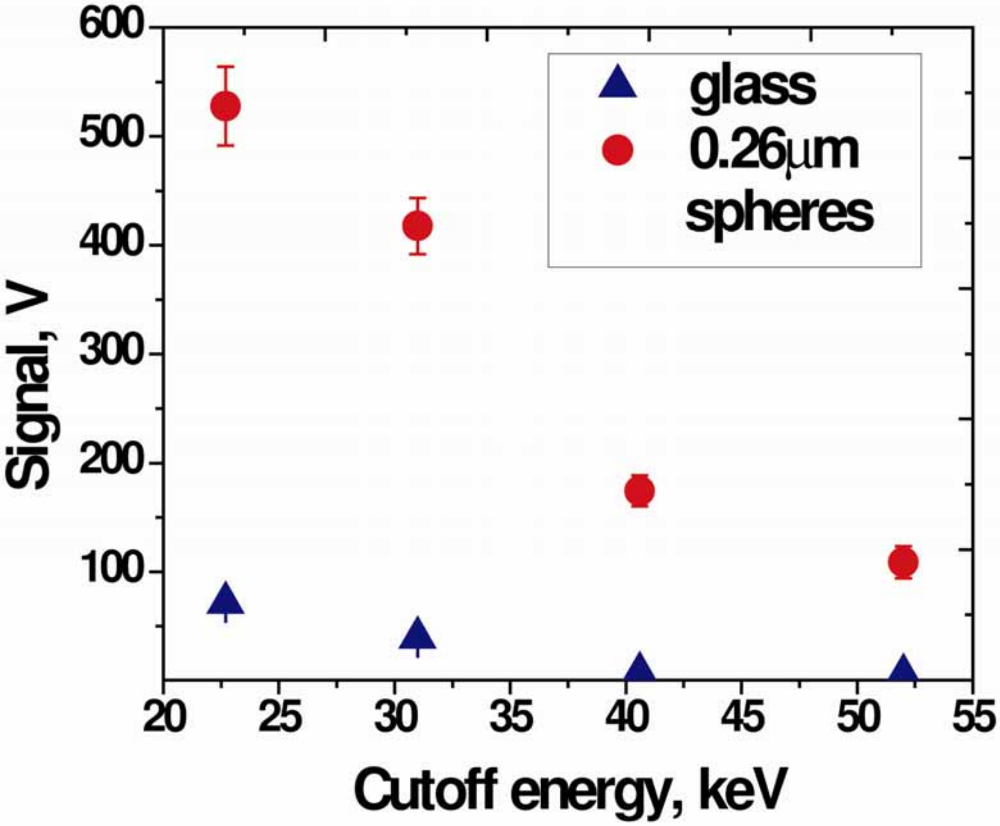

Figure A 7 Hard x-ray yield of glass and sphere coated glass targets irradiated with 400 nm laser pump at 56 degrees.

The x-ray yield was measured from several targets coated with $0.1-2.9$ μm diameter spheres. The results of the measurements are shown in Figure A 8. Every data point was obtained by averaging 25-30 laser shots at each sphere size. The laser was normally incident on the target. At this angle of incidence we observed a very weak x-ray signal from the uncoated fused silica substrate. As it seen from the graph there is a strong dependence of the hard x-ray production on the sphere size. The peak in the x-ray production corresponds to the measurement done on the 0.26 μm sphere coated target. As it has been shown before, the x-ray yield from the same target was 4-8 times higher compared to the x-ray yield from unmodified target when the laser light was incident at 55 degrees (Figure A 7). Furthermore, at normal incidence the irradiated 0.26 μm sphere coated target produced an enhancement of the x-ray yield of >1000 compared to the unmodified target x-ray yield. The fitted hot electron temperatures from the 0.1-2.9 μm sphere coated targets was consistent with the average value of 20 keV and a weak peak in temperature for 0.26 μm sphere target. Compared to the x-ray yield obtained for the 0.1, 0.5, and 2.9 μm sphere coated targets, the x-ray yield obtained from the 0.26 μm sphere coated target was 3 times larger.

The data shows strong dependence of the x-ray yield on the target modification size. We believe that this is a result of Mie enhancements of the laser field, which resulted in increase of x-ray yield and temperature. By doing the angle scan of the unmodified target we showed that the main absorption mechanism is the vacuum heating. In this regime, the average electron temperature is of the ponderomotive energy that is 3 keV in our case. As been discussed above, the average electron temperature observed in our measurements of the irradiated modified targets was 20 keV. To be able to reach such high electron temperature it would require the enhancement of the local electric field.

Another possible mechanism for increase electron temperature is the multiple vacuum heating, or so called stochastic heating [84, 85]. In this regime, electron first accelerated out of the overdense plasma region of the sphere and then driven back into it by the combined effects of the laser field and the electrostatic field produced by the laser-driven charge separation. Under the right circumstances, some electrons can undergo many such vacuum heating passes on each side of the plasma sphere. To explorer the interplay of the effect of the field enhancement generated by Mie resonances and the effect of the multiple vacuum heating, Pukhov at al [83] conducted particle in cell simulation of electron heating. This simulations assumed a ~10fs pulse, 400nm pulse incident on a plasma sphere with an intensity of $2*10^{17}$ W/cm^2. The simulation showed that the maximum in the average energy of the hot electrons occurs for the plasma spheres of 250nm diameter that is in agreement with our measurement.

In conclusion, we observed that by controlling the size of the surface modification of the target allows for control of the strong electric field coupling to hot electron and enhancement of hard x-ray production. The resonance-like behavior for the x-ray production was observed for $0.26\mu m$ sphere coated target. We think that the observed strong increase in hot electron temperature is the result of the combination of the effect of the field enhancement generated by Mie resonances and the effect of the multiple vacuum heating. Our measurement demonstrated a way to enhance x-ray yield for laser based x-ray sources with a simple modification of the target surface.

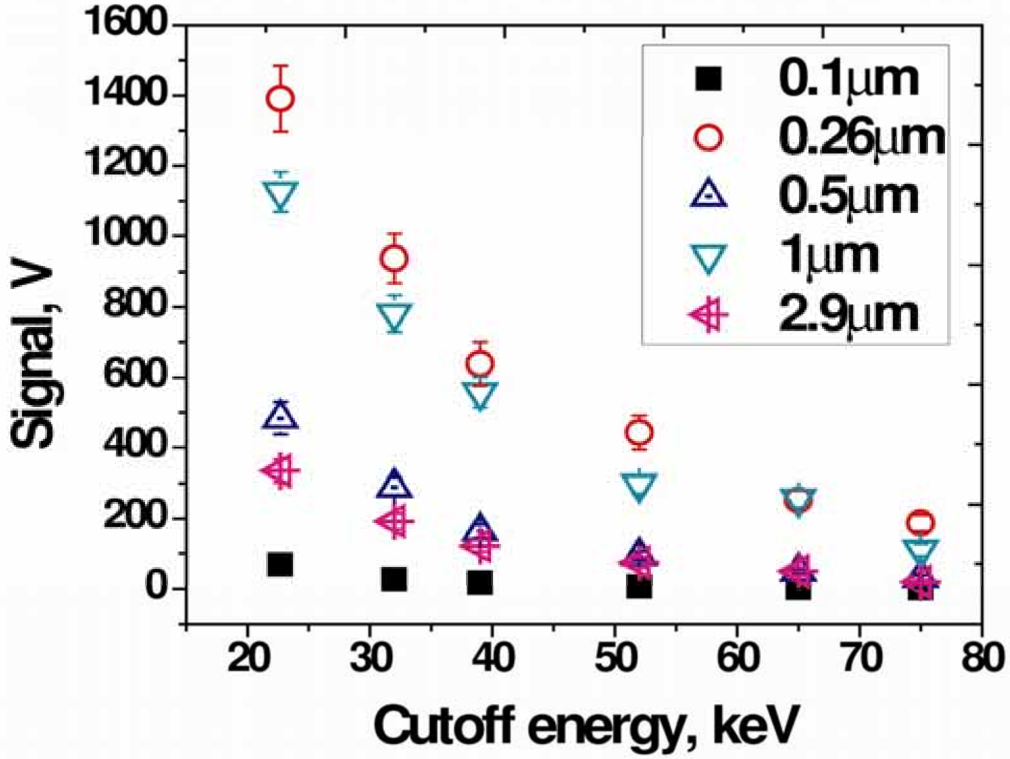

Figure A 8 Hard x-ray yield of glass targets coated with 0.1, 0.26, 0.5, 1 and 2.9 μm polystyrene spheres irradiated with 400 nm laser beam at normal incidents.

Appendix B HYADES input file for free standing Al foil

The following file was used as an input file for 2007 HYADES code available on Livermore computer. The files with the currently available EOS and the consistent with it ionization tables are recalled in the code.

```
c Al foil heated by the laser wave source
c
mesh 1 141 0.0e-6 .835e-5 1.02
mesh 141 189 .835e-5 1.67e-5
region 1 188 1 2.7 2.6e-5 2.6e-5
material 1 13.  26.98 1.
c
eos /g/g17/larsen/EOS/LEOS/leos_713.dat 1 $Al
c
ioniz 1 3 0.0005
data ioniz 1 /g/g17/larsen/EOS/LEOS/zeff_4713.dat
c
data thrmcond 1 0.0005 2.33e+14
c
c 2.5e14 watts/cm^2, wavelength = .4 micron
source wave .4 +1 1 0
gauss 1.5e-13 2.5e21 5.1e-14
c
c room temperature dielectric function
```

```
data refindx 1 0.00015 0.49
data absindx 1 0.00015 4.86
c
data tmelt 1 1.05e-4 1.5 1.97
data metal 1 1 9.1e+13 0.65 1 1 3.48e+25 1 2.67e+14
c
pparray r rcm te ti rho dene deni taue tauei zbar elecon0 pres deplas conde condi
c
parm alvism .3
parm qstimx 5.e-5
parm flxlem 0.05
parm xlabth 1.e+10
parm temin 2.6e-5
parm timin 2.6e-5
parm trmin 2.6e-5
parm dtmax 1.e-15
parm editdt 2.e-13
parm postdt 2.e-13
parm tstop 1.8e-11
parm itmcyc 1000
parm nstop 100000
```

References

1. Kadau, K., et al., *Shock waves in Polycrystalline Iron.* Physical Review Letters, 2007. **98**: p. 135701.
2. Perry, M.D., et al., *Ultrashort-pulse laser machining of dielectric material.* J. Appl. Phys., 1999. **85**: p. 6803.
3. Hubbard, W.B., et al., *Liquid metallic hydrogen and the structure of brown dwarfs and giant planets.* Phys. Plasmas, 1997. **4**(5): p. 2011-2015.
4. Yaakobi, B., et al., *Symmetric Laser Compression of Argon-Filled Glass Shells to Densities of 4-6 g/cm^3.* Physical Review Letters, 1980. **44**(66): p. 1072-1075.
5. Donnelly, T.D., et al., *Hard x-ray and hot electron production from intense laser irradiation of wavelength-scale particles.* Journal of Physics B: Atomic, Molecular and Optical Physics, 2001. **34**: p. L313-L320.
6. Gavrilov, S.A., et al., *Efficient hard X-ray source using femrosecond plasma at solid targets with a modified surface.* Laser and Particle Beams, 2004. **22**(301-306).
7. Sumeruk, H.A., et al., *Control of Strong-Laser-Field Coupling to Electrons in Solid Targets with Wavelength-Scale Spheres.* Physical Review Letters, 2007. **98**: p. 045001.
8. Nguyen, J.H. and N.C. Holmes, *Melting of iron at the physical conditions of the Earth's core.* Nature, 2004. **427**(6972): p. 339-341.
9. Knudson, M.D., et al., *Principal Hugoniot, reverberating wave, and mechanical reshock measurements of liquid deuterium to 400 GPa using plate impact techniques.* Physical Review B, 2004. **69**.
10. Benage, J.F., W.R. Shanahan, and M.S. Murillo, *Electrical Resistivity Measurements of Hot Dense Aluminum.* Physical Review Letters, 1999. **83**(15): p. 2953-2956.
11. Davis, J.-P., et al., *Magnetically driven isentropic compression to multimegabar pressures using shaped current pulses on the Z accelerator.* Physics of Plasmas, 2005. **12**.
12. Patel, P.K., et al., *Isochoric Heating of Solid-Density Matter with an Ultrafast Proton Beam.* Physical Review Letters, 2003. **91**(12).
13. Dyer, G.M., et al., *Equation-of-State Measurement of Dense Plasmas Heated With Fast Protons.* Physical Review Letters, 2008. **101**.
14. Milchberg, H.M. and R.R. Freeman, *Light absorption in ultrashort scale length plasmas.* J. Opt. Soc. Am.B, 1989. **6**(7): p. 1351-1355.
15. Fedosejevs, R., et al., *Absorption of Femtosecond Laser Pulses in High-Density Plasma.* Physical Review Letters, 1990. **64**(1250-1253).
16. Price, D.F., et al., *Absorption of Ultrashort Laser Pulses by Solid Targets Heated Rapidly to Temperatures 1-1000 eV* Physical Review Letters, 1995. **75**(252-255).

17. Grimes, M.K., et al., *Experimental Indentification of "Vacuum Heating" at Femtosecond-Laser-Irradiated Metal Surfaces.* Physical Review Letters, 1999. **82**(20): p. 4010-4013.
18. Wang, X.Y. and M.C. Downer, *Femtosecond time -resolved reflectivity of hydrodynamically expanding metal surfaces* Optics Letters, 1992. **17**(20): p. 1450-1452.
19. Widmann, K., et al., *Interferometric Investigation of Femtosecond Laser-Heated Expanded States.* Physics of Plasmas, 2001. **8**(9): p. 3869-3872.
20. Milchberg, H.M., et al., *Resistivity of a Simple Metal from Room Temperature to* 10^6 *K.* Physical Review Letters, 1988. **61**(20): p. 2364-2367.
21. Ng, A., et al., *A.Reflectivity of Intense Femtosecond Laser Pulses from a Simple Metal* Physical Review Letters, 1994. **72**(21): p. 3351.
22. Widmann, K., et al., *Single-State Measurement of Electrical Conductivity of Warm Dense Gold* Physical Review Letters, 2004. **92**(12): p. 125002-1-125002-4.
23. Ping, Y., et al., *Broadband Dielectric Function of Nonequilibrium Warm Dense Gold.* Physical Review Letters, 2006. **96**: p. 255003.
24. Ng, A., A. Forsman, and G. Chiu, *Electron Thermal Conduction Waves in a Two-Temperature, Dense Plasma.* Physical Review Letters, 1998. **81**(14): p. 2914-2917.
25. Gahagan, K.T., et al., *Measurement of Shock Wave Rise Times in Metal Thin Films* Physical Review Letters, 2000. **85**(15): p. 3205-3208.
26. Funk, D.J., et al., *Ultrafast Measurement of the Optical Properties of Aluminum during Shock-Wave Breakout.* Physical Review B, 2001. **64**: p. 115114-115114-5.
27. Gahagan, K.T., et al., *Ultrafast interferometric microscopy for laser-driven shock wave characterization.* Journal of Applied Physics, 2002. **92**(7): p. 3679-3682.
28. Tokunaga, E., A. Terasaki, and S. Kobayashi, *Frequency-domain interferometer for femtosecond time-resolved phase spectroscopy.* Optics Letters, 1992. **17**(16): p. 1131-1133.
29. Martinez, O.E., *Design of High-Power Ultrashort Pulse-Amplifiers by Expansion and Recompression.* IEEE Journal of Quantum Electronics, 1987. **23**(8): p. 1385-1387.
30. Strickland, D.J. and G. Mourou, *Compression of Amplified Chirped Optical Pulses.* Optics Communication, 1985. **55**(6): p. 447-449.
31. Treacy, E.B., *Optical Pulse Compression with Diffraction Gratings.* IEEE Journal of Quantum Electronics, 1969. **5**(9): p. 454-458.
32. Dyer, G.M., *Experimental Study of the Equation of State of Isochorically Heated Warm Dense Matter*. 2007, The University of Texas at Austin Austin, TX.
33. Hays, G.R., *Development of Broad Spectrum Technologies for High Energy Chirped Pulse Amplification*. 2007, The University of Texas at Austin: Austin, TX.
34. Grigsby, W.R., *Experimental Studies of High Energy Density Silicon Using Ultra-Fast Lasers*. 2007, The University of Texas at Austin: Austin, TX.
35. Banks, P.S., et al., *Novel all-reflective strecher for chirped-pulse amplification of ultrashort pulses.* IEEE Journal of Quantum Electronics, 2000. **36**(3): p. 268-274.

36. Ao, T., et al., *Optical Properties of Nonequilibrium Phase Transitions.* Physical Review Letters, 2006. **96**: p. 055001-055001-4.
37. Kruer, W.L., *The Physics of Laser Plasma Interaction.* 1988: Addison-Wesley Publishing Company, Inc.
38. Eidmann, K., et al., *Hydrodynamic simulation of subpicosecond laser interaction with solid-density matter.* Physical Review E, 2000. **62**(1202-1214).
39. Zeldovich, Y.B. and Y.P. Raizer, *Physics of Shock Waves and High-Temperature Hydrodynamic Phenomena.* 2002, Mineola, NY: Dover Publication, INC.
40. Ditmire, T., et al., *Supersonic Ionization Wave Driven by Radiation Transport in a Short-Pulse Laser-Produced Plasma.* Physical Review Letters, 1996. **77**(3): p. 499-501.
41. Hazeltine, R.D. and F.L. Waelbroeck, *The Framework of Plasma Physics.* 1998, Reading, MA: Perseus books.
42. Lee, Y.T. and R.M. More, *An Electron Conductivity Model for Dense Plasmas.* Phys. Fluids, 1984. **27**(5): p. 1273-1285.
43. Ashcroft, N.W. and N.D. Mermin, *Solid State Physics*: Harcourt College Publishers.
44. Spitzer, L. and R. Harm, *Transport Phenomena in a Completely Ionized Gas.* Physical Review, 1953. **89**(5): p. 977-981.
45. Rinker, G.A., *Electrical conductivity of a strongly coupled plasma.* Physical Review B, 1985. **31**(7): p. 4207-4219.
46. Desjarlais, M.P., J.D. Kress, and L.A. Collins, *Electrical conductivity for warm, dense aluminum plasmas and liquids.* Physical Review E, 2002. **66**(R): p. 025401-1-4.
47. Kim, K.Y., et al., *Measurement of Terahertz Electrical Conductivity of Intense Laser-Heated Dense Aluminum Plasmas.* Physical Review Letters, 2008. **100**: p. 135002-135004.
48. Mostovych, A.N. and Y. Chan, *Reflective Probing of Elecrtical Conductivity of Hot Aluminum in the Solid, Liquid, and Plasma Phases.* Physical Review Letters, 1997. **79**(25): p. 5094-5097.
49. Evans, R., et al., *Time- and Space-Resoved Optical Probing of Femtosecond-Laser-Driven Shock Waves in Aluminum.* Physical Review Letters, 1996. **77**(16).
50. Vu, B.-T.V., O.L. Landen, and A. Szoke, *Time-resolved Probing of Femtosecond-laser-produced plasmas in Transparent Solids by Electron Thermal Transport.* Phys. Plasmas, 1995. **2**(2): p. 476-485.
51. Kittel, C., *Introduction to Solid State Physics.* 1986, NY: John Wiley &Sons, Inc.
52. Born, M. and E. Wolf, *Principles of Optics, 6th ed.* 1980: Pergamon Press, Oxford.
53. Jackson, J.D., *Classical Electrodynamics.* 1999, NY John Wiley&Sons, Inc.
54. Bethune, D.S., *Optical harmonic generation and mixing in multilayer media: analysis using opitcal transfer matrix techniques.* J. Opt. Soc. Am. B, 1989. **6**(5): p. 910-916.
55. Ashcroft, N.W. and K. Sturm, *Interband Absorption and the Optical Properties of Polyvalent Metals.* Physical Review B, 1971. **3**(6): p. 1898-1910.

56. Tups, H. and K. Syassen, *Effect of pressure on the optical absorption in aluminum.* J. Phys. F: Met.Phys, 1984. **14**: p. 2753-2767.
57. Mathewson, A.G. and H.P. Myers, *Optical absorption in aluminum and the effect of temperature* J. Phys. F: Met.Phys, 1972. **2**: p. 403-415.
58. Brunel, F., *Not-So-Resonant, Resonant Absorption.* Physical Review Letters, 1987. **59**(1): p. 52-55.
59. Benuzzi-Mounaix, A., et al., *Chirped Pulse Reflectivity and Frequency Domain Interferometry in Laser Driven Shock Experiments.* Physical Review E, 1999. **60**(3): p. R2488-R2491.
60. Cho, B.I., et al., *Hot Electron Generation From Intense Laser Irradiation of Micro-Tiped Cone and Wedge Targets* Physics of Plasmas, 2008.
61. Pandy, A., et al., *Experimental investigation of high Si/Al selectivity during anisotropic etching in tetra-methyl ammonium hydroxide.* J. Vac. Sci. Technol. A, 1998. **16**(2): p. 868-872.
62. Vu, B.-T.V., A. Szoke, and O.L. Landen, *Time-Resolved Probing of Electron Thermal Transport in Plasma Prduced by Femtosecond Laser Pulses* Physical Review Letters, 1994. **72**(24): p. 3823-3826.
63. Geindre, J.P., et al., *Frequency-domain Interferometry for Measuring the Phase and Amplitude of a Femtosecond Pulse Probing a Laser-produced Plasma.* Optics Letters, 1994. **19**(23): p. 1997-1999.
64. Forsman, A., et al., *Interaction of femtosecond pulses with ultrathin foils.* Physical Review E Rapid Communication, 1998. **58**(2): p. R1248-R1251.
65. Wang, X.Y., et al., *Time-resolved electron-temperature measurement na highly excited gold target using femtosecond thermionic emission.* Physical Review B, 1994. **50**(11): p. 8016-8019.
66. me, *lkjhlkjh.* ghhengis flan, 2008. **5**(1): p. 15.
67. Tokunaga, E., A. Terasaki, and S. Kobayashi, *Femtosecond continuum interferometer for transient phase and transmission spectroscopy.* J.Opt. Soc. Am. B, 1996. **13**: p. 496-513.
68. Chien, C.Y., et al., *Single-shot chirped-pulse spectral interferometry used to measure the femtosecond ionization dynamics of air.* Optics Letters, 2000. **25**(8): p. 578-580.
69. Le Blanc, S.P., et al., *Sine-shot measurement of temporal phase shift by frequency-domain holography.* Optics Letters, 2000. **25**(10): p. 764-766.
70. Geindre, J.P., et al., *Single-shot Spectral Interferometry with Chirped Pulses* Optics Letters, 2001. **26**(20): p. 1612-1614.
71. Rebibo, S., et al., *Single-shot spectral interferometry of femtosecond laser-produced plasma.* Laser and Particle Beams, 2001. **19**: p. 67-73.
72. Siders, C.W., et al., *Laser Wakefield Excitation and Measurement by Femtosecond Longitudinal Interferometry.* Physical Review Letters, 1996. **76**(19): p. 3570-3573.
73. Takeda, M. and S. Kobayashi, *Fourier-transform Method of Fringe-pattern Analysis for Computer-based Topography and Interferometry.* J. Opt. Soc. Am., 1982. **72**(1): p. 156-160.

74. Kim, K.Y., I. Alexeev, and H.M. Milchberg, *Single-shot supercontinuum spectral interferometry.* Applied Physics Letters, 2002. **81**(22): p. 4124-4126.
75. Smith, F.W., *Optical constants of a hydrogenated amorphous carbon film.* Journal of Applied Physics, 1984. **55**(3): p. 764-771.
76. Rozmus, W. and V.T. Tikhonchuk, *Skin Effect and Interaction of Short Laser Pulses with Dense Plasmas.* Physical Review A, 1990. **42**(12): p. 7401-7412.
77. Dandrea, R.G. and N.W. Ashcroft, *High pressure as a probe of electron structure: Aluminum.* Physical Review B, 1985. **32**(10): p. 6936-6938.
78. Trunin, R.F., *Experimental Data on Shock Compression and Adiabatic Expansion of Condense Matter*, in *SAROV, RFNC-VNIIEF*. 2001.
79. Larsen, J.T. and S.M. Lane, *HYADES- A Plasma Hydrodynamics Code For Dense Plasma Studies.* J. Quant. Spectrosc. Radiat. Transfer, 1994. **51**(1): p. 179-186.
80. More, R.M., et al., *A new quotidian equation of state (QEOS) for hot dense matter.* Phys. Fluids, 1988. **31**(10): p. 3059-3058.
81. Murnane, M.M., et al., *Efficient coupling of high-intensity subpicosecond laser pulses into solids.* Applied Physics Letters, 1993. **62**(1068).
82. Kulcsar, G., et al., *Intense Picosecond X-Ray Pulses from Laser Plasmas by Use of Nanostructured "Velvet" Targets.* Physical Review Letters, 2000. **84**(5149).
83. Sumeruk, H.A., et al., *Hot electron and x-ray production from intense laser irradiation of wavelength-scale polystyrene spheres.* . Physics of Plasmas, 2007. **14**(062704).
84. Antonsen, T.M., et al., *Resonant heating of a cluster plasma by intense laser light.* Physics of Plasmas, 2005. **12**: p. 056703.
85. Breizman, B.N., A.V. Arefiev, and M.V. Fomyts'kyi, *Nonlinear physics of laser-irradiated microclusters.* Physics of Plasmas, 2005. **12**(056706).

Vita

Irina V. Churina was born on May 24, 1978 in Kirovo-Chepetsk, Russia to Vera E. Churina and Vladimir V. Churin. After completing her work at High School in Protvino, Russia in 1995, she attended Lomonosov Moscow State University in Moscow, Russia, where she earned a M.S. in physics in January 2001. In August 2001, she enrolled in the University of Texas at Austin to pursue a doctoral degree in physics.

Permanent address: 1901 Garden drive, Burlingame, CA 94010

This dissertation was typed by the author.